

Few-Cycle Laser Pulse Generation and Characterization for Coulomb Explosion Imaging of Molecules

by

Michael Singh

A thesis
presented to the University of Waterloo
in fulfillment of the
thesis requirement for the degree of
Master of Science
in
Physics

Waterloo, Ontario, Canada, 2019

© Michael Singh 2019

Author's Declaration

I hereby declare that I am the sole author of this thesis. This is a true copy of the thesis, including any required final revisions, as accepted by my examiners.

I understand that my thesis may be made electronically available to the public.

Abstract

Ultrashort pulses can induce coulomb explosions of molecules through which ionic fragments receive substantial momentum. These momenta, measured in coincidence, carry information about the molecule's initial geometry. Momenta measurements can be done using a modified time-of-flight spectrometer. The spectrometer is improved upon by modifying the housing of its focusing mirror. The ion extraction field exhibited greater uniformity due to a more robust mirror mounting design and a correction of structural asymmetries. Ultrashort pulses are measurement tools, exploited for their brevity in duration and are sought to be made even shorter to improve their time resolution. Hollowfibre pulse compression studies are done to investigate the impacts of pressure on spectral broadening results. The pulses that exit the pulse stretching and compression components in the hollowfibre system can become riddled with distortions. The pulses need to be characterized to identify and correct distortions before they can be used to interrogate molecules. Frequency-resolved optical gating (FROG) techniques have demonstrated powerful characterization capabilities. A qualitative and quantitative methodology is presented in order to analyze the validity of FROG measurements of simple Gaussian pulses and then more complex, frequency modulated pulses.

Acknowledgements

Firstly, I would like to thank my supervisor Dr. Joseph Sanderson for trusting me to watch over the lab and giving me the freedom to explore all of my creativity without looking over my shoulders. He exposed me to experiments of all kinds and introduced me to so many researchers. The countless opportunities that he provided will not be forgotten.

Perhaps my most exciting time in graduate school was when Dr. Donna Strickland won the Nobel Prize in Physics for her work on Chirped Pulse Amplification. Since she is on my committee and we shared a part of the lab with her, I had the opportunity of touring and meeting many of her visitors and guests. Not too mention the TV cameras! I would like to thank her for making graduate school unforgettable and that much more enjoyable.

Dr. Kevin Resch was a great help when I was struggling in his Quantum Optics course. He dedicated more time and effort to me than should be expected of a professor. I ended up doing quite well in the course thanks to his help. If that wasn't enough, he loaned the GRENOUILLE to our lab which I based a large part of my thesis on.

I would like to thank Dr. Marcel Nooijen for being a great committee member with his interesting questions and comments. Dr. Benjamin Wales gave me a great number of tips when he left the lab in my hands. Abdullah Rahnama, Reza Reihani, and Dr. Reza Karimi were great companions in the lab and will continue to be good friends of mine. Thanks are also in order for the rest of the lab researchers, undergraduate volunteers, and the machine shop.

Lastly, of course, my biggest thank you is to my parents for keeping me in school and out of jail. I remember in high school I told my mom that I wanted to go to college instead of university. It's safe to say she convinced me to go to university. The rest is history.

Dedication

In dedication to my parents and my loved ones, including Akimbo and Adonis, the two goofy rottweilers.

Table of Contents

List of Tables	ix
List of Figures	x
1 Introduction	1
2 Coulomb Explosion Imaging Using Ultrashort Laser Pulses	4
2.1 Introduction	4
2.2 Ultrashort Pulses	6
2.3 Ti:Sapphire Oscillator - Ultrashort Pulse Generation	7
2.3.1 Oscillator Design	8
2.4 Chirped Pulse Amplification System	8
2.4.1 CPA System Design	12
2.5 Coulomb Explosion Imaging Principles	12
2.6 Experimental Design and Techniques	16
2.7 Experimental Data Acquisition and Analysis	22
2.7.1 Time-of-flight Histogram	22
2.8 TOF Spectrometer Modification	24
2.8.1 Results	28

3	Hollowfibre Pulse Compression: Few-Cycle Generation	34
3.1	Introduction	34
3.2	Experimental Design and Techniques	36
3.3	Results	38
4	Pulse Characterization	43
4.1	Introduction	43
4.2	Single-Shot Autocorrelator	45
4.2.1	Experimental Design and Techniques	48
4.2.2	Results	48
4.3	GRENOUILLE: FROG Trace	49
4.3.1	Experimental Design and Techniques	53
4.3.2	Results	55
5	Conclusion and Future Work	71
	References	74
	APPENDICES	80
A	Laser Induced Breakdown Spectroscopy (LIBS): An Industrial Application	81
A.1	Introduction	81
A.2	Laser System	81
A.3	Apparatus	82
A.4	Ablation Characteristics	83
A.5	Spectra Collection	83
A.6	LIBS Test Results	84
A.6.1	Coating analysis: demonstration of LIBS for a prime hand-held application	84

A.6.2	Mixed metals analysis: sorting common metal alloys and super-alloys with very complex spectra	86
A.6.3	Ni-Cr-Mo alloys: quantitative analysis and the selection of key elements for calibration	87
A.6.4	Diagnostics: an example of a measurement that is critical for quantitative LIBS	88
A.7	Conclusion and Future Work	90
B	Oscillator Optimization Technique	92
C	Spitfire Ace CPA System Techniques	93
C.1	Electronic Components	93
C.1.1	Start-up from Standby Mode	93
C.1.2	Cable Connections	95
C.1.3	Optimization techniques	96
C.2	Optimization Results	97
C.2.1	December 12, 2017	97
C.2.2	January 11, 2018	98
C.2.3	March 29, 2018	98
C.2.4	June 21, 2018	99
D	Hollowfibre Alignment Technique	100
E	GRENOUILLE Techniques	101
F	Time-Of-Flight Spectrometer Techniques	115
F.1	Coulomb Explosion Imaging Chamber Alignment Technique	115
F.2	Electronic Connections	117
F.2.1	Starting the TOF Spectrometer	120
F.3	Plot Identification Algorithm Code	120

List of Tables

2.1	Oscillator specifications	8
2.2	Regenerative amplifier Spitfire Ace-35F specifications	12
A.1	Composition of samples.	87

List of Figures

2.1	Visualization of beam-foil ionization. Reprinted with permission from [50].	6
2.2	Oscillator with the roof removed to reveal the internal optics	9
2.3	The measured spectrum of the oscillator.	10
2.4	Diffraction grating stretcher using positive GVD (from [42, p. 3-5])	11
2.5	Schematic layout of Spitfire Ace-35F from Spectra-Physics (from [42, p. 8-1])	13
2.6	Measured spectrum of the Spitfire Ace with a central frequency of 798.8 nm and full-width at half maximum (FWHM) of 32.8 nm.	13
2.7	MCP with 4 signal. Reprinted from [29] with permission from Elsevier. . .	19
2.8	Visualization of the ion time-of-flight process after a Coulomb explosion in the TOF spectrometer.	20
2.9	The TOF spectrometer oriented upside down as compared to normal operation. Each metallic plate (electrode) is separated by equally thick Teflon spacers. The stack is suspended from the flange by four threaded rods. There is a cutout to make the parabolic focusing mirror accessible to the laser beam. The resistor chain acts as a voltage divider circuit for the electrodes.	21
2.10	Sig waveform showing 4 detection signals (bottom) and their sum (blue signal, top).	23
2.11	Mirror mount prior to modification	26
2.12	Overly thick mirror mount causing the metallic plates to bend outward. . .	26
2.13	Autocad design for the new mirror mount.	28
2.14	TOF histogram obtained using the mirror mount prior to modification. . .	29

2.15	TOF histogram obtained using the newly modified mirror mount. The peaks are much more distinguishable than the TOF histogram in Fig. 2.14. . . .	30
2.16	The calibration lines for the TOF histograms from prior to and after TOF the spectrometer modification. The most probable times for ionic species are plotted on the line.	32
3.1	Linearly chirped pulse with positive GVD	37
3.2	Experimental setup of the hollowfibre compressor system.	38
3.3	Ideal spectral broadening result from [11]	39
3.4	Series of spectra with varying pressure and by varying the compressor position of the Spitfire Ace.	40
3.5	Table (left) and plot (right) of bandwidth vs. pressure.	41
3.6	Table (left) and plot (right) of the number of modulations vs. pressure.	41
3.7	(a) and (b) show the two closest matching spectra to the reference spectrum. (c) and (d) show the spectra from (a) and (b), respectively, overlaid on the reference spectrum for comparison. The spectrum in (a) spans from approximately 600 nm to 900 nm and exhibits 6 modulations. The spectrum in (b) spans from approximately 540 nm to 900 nm and exhibits 7 modulations.	42
4.1	Autocorrelator diagram	47
4.2	Visualization of a single-shot autocorrelation (from [49]).	47
4.3	Autocorrelation result with the spatial image on the left and the retrieved intensity function $I(t)$ on the right. The temporal FWHM was measured as 38 fs.	48
4.4	A visualization of how a FROG trace is generated. A gate function is scanned across the pulse waveform where the spectrum is computed for each gated portion (the depiction on the left is from [49, p. 102]).	50
4.5	Schematic of a non-collinear SHG FROG (from [49, p. 126])	51
4.6	Optical layout of GRENOUILLE apparatus (from [49, p. 231])	52
4.7	Visualization of angle dithering the SHG crystal. Reprinted with permission from [32].	53
4.8	The side-view and top-view of the GRENOUILLE beam geometry (from [49, p. 231])	54

4.9	Comparison of the independently measured beam profile (left) and the beam profile measured by the GRENOUILLE (right).	56
4.10	Independent beam profiler setup.	56
4.11	Retrieved FROG measurement of pulses from the Spitfire Ace with a notable asymmetry on the right-hand side.	58
4.12	Retrieved FROG measurement of pulses from the Spitfire Ace. Both axes exhibit Gaussian forms.	59
4.13	Retrieved spectrum and phase from the FROG measurement of Fig. 4.12	60
4.14	Autoconvolution test: Comparison of the autoconvolution (red line) of the independently measured Spitfire Ace spectrum (blue line) from Fig. 2.6 with the frequency marginal of the FROG trace of Fig. 4.12. The autoconvolution is observed to have a considerably larger full range causing the autoconvolution test to fail.	61
4.15	Retrieved intensity and phase from the FROG measurement of Fig. 4.12.	62
4.16	Independently measured spectrum of hollowfibre compressed pulses.	63
4.17	Retrieved FROG measurement of the same hollowfibre compressed pulses which correspond with Fig. 4.16	64
4.18	Returned spectrum and phase from the FROG measurement of Fig. 4.17.	65
4.19	Comparison of the hollowfibre spectra measured by the USB4000 (red) and returned from the GRENOUILLE (blue). The arrows indicate spectral peaks which are similar for both spectra.	66
4.20	Autoconvolution test: Comparison of the autoconvolution (red line) of the independently measured hollowfibre spectrum (blue line) from Fig. 4.16 with the frequency marginal of the FROG trace of Fig. 4.17. The autoconvolution is observed to have a considerably larger full range causing the autoconvolution test to fail. However, both curves exhibit similar spectral features. Both are double-peaked with a small shoulder on the left peaks.	67
4.21	Retrieved spectrum and phase from a FROG measurement of hollowfibre compressed pulses. The phase exhibits a complex form as opposed to the phase function in Fig. 4.18.	68
4.22	Returned intensity and phase from the FROG measurement of hollowfibre compressed pulses of Fig. 4.17.	69

A.1	Empower 30 Q-Switched Green Laser.	82
A.2	Sample chamber.	82
A.3	Ablation spot.	83
A.4	Spectra collection setup	84
A.5	Schematic	84
A.6	Spectra of the super-alloys compared to the Fe reference in spectral range of the HR4000	85
A.7	The coating signal (top plot) is obtained by a rapid exposure to the laser, only ablating the surface coating of the galvanized steel. The coating signal is compared to reference spectra with accurate peak matching of Zn (328 nm, 330 nm, 334 nm), Ca (393 nm), and Al (394 nm and 396 nm). The substrate signal (bottom plot) is acquired by using a delayed exposure to ablate through the surface to the Fe reference.	86
A.8	Spectral segment from 375 to 425 nm to show wavelength accuracy and relative intensities for the Fe reference spectrum and the Empower LIBS spectrum.	87
A.9	INCONEL and INCOLOY spectra with Fe and Mo reference spectra for peak-matching.	88
A.10	INCONEL and INCOLOY narrow spectral segment 340 nm - 355 nm with Ni reference spectra for peak-matching.	89
A.11	SS316 with Fe interference and identification lines for Ni, Mo, and Cr.	89
A.12	The discrepancy between peak ratios of LIBS AL6160 spectrum and Al reference spectrum is good indication of self-absorption. The ratio of left peak to right peak in the reference spectrum is 1:2 as compared to the approx. 1:1 ratio in LIBS spectrum.	90
A.13	Self-absorption example from [57].	91
C.1	The Spitfire Ace GUI control software. Reprinted from [42].	94
C.2	Photo of the electronic components for the Spitfire Ace	95
C.3	Build-up signal showing the amplification of pulses after each pass through the Ti:Sapphire crystal.	97
E.1	Screenshot of QuickFrog software in Time Mode during operation.	102

E.2	Photo of the AGC driver and its phase and amplitude tuning knobs.	103
F.1	Laser beamline into CEI chamber	116
F.2	Visualization of a perfectly aligned CEI beamline, where the incident beam is centred exactly on the outgoing back reflection.	117
F.3	A card can be used to block the incident beam to see how it compares to the vertical half, the horizontal half, and a quarter of the back reflection.	117
F.4	The proper connection orientation for the ion detector box. Notice there is a small black line on the white part of the ion detector box which must align with the slot cutout shown on the CEI chamber.	118
F.5	Perspective on orientation of the CEI chamber to assist in the proper connection of the ion detector box.	119
F.6	There are 4 position detection boxes that need to be connected to 4 coaxial inputs on the CEI chamber. Only 3 position detection boxes are shown, the 4th box is not visible.	120

Chapter 1

Introduction

The invention of the camera enabled us to capture a moment frozen in time. Cameras are the paintbrushes of old, the pinnacle of modern entertainment. These devices are the most common image captors. What is an *image*? An image is a rendition of reality at a particular moment in time. Types of images include sculptures, paintings, magnetic resonance images (MRI), the all-too-common photograph, and even Coulomb explosion images of molecules. Every imaging modality renders an image in a different way. Each require a sensory instrument to receive physical information of which to interpret into an image. Physical information can come in many forms, such as photons, electrons, sound waves, and in the case of Coulomb explosion imaging, ions. The common camera receives photons on a photo-sensitive medium to create a photographic image. MRI uses oscillating magnetic fields to induce a sample's hydrogen atoms to emit radio waves which are detected and interpreted into an image. Human eyes image reality by detecting photons of visible light with photoreceptors that send signals to our brain to render an image. This image of reality may differ from say, a snake's image of reality since its eyes detect infrared photons. If our eyes can't image certain objects, we must employ external devices to do our bidding. So how does one image a molecule; invisible to the naked eye? This has been a long-lasting endeavour since the rise of atomic theory.

A technique known as Coulomb Explosion Imaging (CEI) was introduced by Kanter et al. in [24] which offered a new way to study molecules. Not only can the static structure of a molecule be studied but also its dynamical structure as it evolves over time. Structural dynamics include bond lengthening and shortening, structural bending, and even its dynamical properties such as the migration of a proton[52, 20]. A *molecular movie* can be created if a sequence of images of molecular dynamics is captured over time [36].

A molecule consists of two or more atoms each of which are bonded electrostatically. If the bonds are broken, what remains are positively charged ions. The ions will undergo repulsion due to the Coulombic force. The trajectory of the ions will carry with it inherent information about its position at time zero. The molecular structure can then be inferred if there is trajectory information for all its ionic fragments. Any molecule with a temperature above absolute zero Kelvin will be in thermal motion. The motion occurs on very fast timescales, tens of femtoseconds. If the bonds are broken on longer timescales than the characteristic time of a molecule's atomic motion, the resulting image will be *blurred*. The requirement for CEI is that the bonds must be removed on femtosecond timescales to match that of the molecular motion. Enter ultrashort laser pulses - intense bursts of laser light which are extremely thin in space allowing them to traverse a point on *ultrafast* timescales (10^{-15} s). Light is an oscillating electric field and magnetic field, both of which can interact with matter. The electric field is of interest in this application since it is responsible for the rapid ionization of the molecule which leads to a Coulomb explosion. Given sufficient energy, the pulses can be focused down to produce enormous electric fields exceeding the strength of electron potentials. The electric fields can then strip a molecule of many electrons on femtosecond timescales giving rise to a Coulomb explosion. Thus, the ultrashort pulses can be used to Coulomb explode a molecule through which ionic fragments receive substantial momentum. The initial momenta imparted to the ions can be measured and used to infer the molecule's initial geometry.

CEI relies on the brevity of ultrashort pulses; as they become shorter, the time resolution improves. As a result, pulse compression has received a great deal of interest. Hollowfibre compression systems have become standard tools in pulse compression and, as any pulse compression system, they are comprised of a considerable number of optics. Pulses have proven to be extremely fragile and have a knack for distorting as they travel through almost any medium. Since they are the main measuring tool for CEI applications, it is best if the researcher has at least some knowledge of the pulses before they begin an experiment. Without prior knowledge, it would be analogous to measuring the length of a desk with a blank measuring tape! Various devices have been put to the task of measuring pulses. A technique commonly used to characterize pulses is the famous FROG (**F**requency-**R**esolved **O**ptical **G**ating) and its variants. Not only is the length of a pulse important, but also its phase, that is, the relationship of a pulse's frequency with time. Both characteristics can affect CEI results. The FROG has proven to be able to measure both of those characteristics which is quite unique.

Ultrashort pulses are highly malleable which is advantageous since their characteristics provide a broad set of parameters for molecular interaction. For our current setup, the pulses go through the following steps in a CEI experiment:

1. Generation - Ti:Sapphire Oscillator (Chapter 2.3)
2. Amplification - Chirped Pulse Amplification System (Chapter 2.4)
3. Compression - Self-Phase Modulation - Hollowfibre System (Chapter 3)
4. (a) Characterization - GRENOUILLE: FROG traces (Chapter 4)
(b) Coulomb Explosion - CEI (Chapter 2)

The work described in the subsequent chapters improves upon different facets of a CEI experimental setup. The CEI apparatus saw an improvement by redesigning the mount for its focusing mirror. The CEI data, before and after, reveal strong improvements to the uniformity of the ion extraction field. The hollowfibre compression system is studied and the pulse spectra results are presented in comparison to a previously published ideal spectrum. Spectra are produced that closely approach the spectral shape of the published result. Finally, the FROG technique was employed to characterize the hollowfibre compressed pulses. However, the device consistently produced erroneous measurements. Thus, a qualitative and quantitative methodology for assessing FROG measurements was developed. Each of the three main chapters contain an introductory background along with the experimental designs and techniques, finally followed by a discussion of results.

Chapter 2

Coulomb Explosion Imaging Using Ultrashort Laser Pulses

2.1 Introduction

When the atoms of a molecule are multiply ionized, the interatomic bonds are removed which leaves positively charged ions to repel and accelerate away from each other. The repulsive Coulombic force between ions become negligible after a certain separation distance and acceleration ceases. At this point, the ions can be modelled to have initial momenta imparted by the Coulomb repulsion force. The momentum vectors can be used to infer the molecule's initial structure.

For a Coulomb explosion to take place, there must be a rapid ionization mechanism. Furthermore, the imaging requirements put a timing constraint on the ionization mechanism. If the ionization occurs on a timescale larger than that of molecular dynamics, the resulting image will be blurred. This is analogous to the the image of a fast moving object photographed with a slow exposure camera. In order to photograph a moving object and avoid blur, the shutter speed of the camera (or exposure time) must be less than what is known as the object's *characteristic time*. The characteristic time is related to the object's length and speed,

$$\Delta t = \frac{l}{v} \tag{2.1}$$

Thus to photograph a bullet of length 1 cm and speed 1000 m/s, a shutter speed less than or equal to

$$\begin{aligned}
\Delta t &= \frac{l}{v} \\
&= \frac{1\text{cm}}{1000\text{ m/s}} \\
&= 10\ \mu\text{s}
\end{aligned}$$

is required to resolve the bullet.

An ultrafast spectroscopy researcher’s favourite historical reference of fast photography is Eadweard Muybridge’s work with horse hooves in 1872. It was an amazing accomplishment for its time, considered to be a pioneering step in motion photography. Interestingly, this work did not arise from a question in science but a debate between the then Governor of California, Leland Stanford, and a race-horse owner. Muybridge was tasked to determine if all four hooves of a horse are ever simultaneously off of the ground during its gallop [26]. He was a professional photographer and would use photography to answer the question. The difficulty was that the horse was moving at quite a high speed and the hooves are relatively small. The characteristic length of the hooves was 0.1 m and the characteristic speed of the horse was 16.67 m/s [43]. Amazingly, Muybridge had to have a mechanical shutter speed equal to or less than $\Delta t = \frac{0.1\text{m}}{16.67\text{m/s}} = 6\text{ ms}$! An extraordinary feat in 1872. He accomplished his task and the answer to the question was an astounding ‘yes’.

To produce an image of a molecule, for example diatomic Hydrogen, the required pulse duration must be equal to or less than its vibrational period, which is 14 fs [12]. Hence the need for few-cycle pulses.

Early CEI experiments relied on beam-foil ionization. Molecular beams of MeV energy were directed through an atomically thin aluminum foil. Electrons of the passing molecules will encounter a wall of electrons in the foil which will cause scattering of the molecule’s electrons at large angles, shown in Fig. 2.1. This process will rapidly (10^{-16} s) strip the molecule of its electronic bonds and induce a Coulomb explosion [27]. The constituent ionic fragments then fly off to a detector. The geometric information of the molecule is encapsulated in the momenta of the ions to be uncovered via classical mechanics.

Following beam-foil ionization, newer rapid ionization techniques were developed such as highly charged ion collisions. The advent of high-intensity femtosecond laser pulses allowed optics to enter the field of ultrafast spectroscopy. The controllability and stability of ultrashort laser pulses made them excellent candidates for CEI applications. Time-resolved studies were available using ultrashort pulses that were not available for many previous

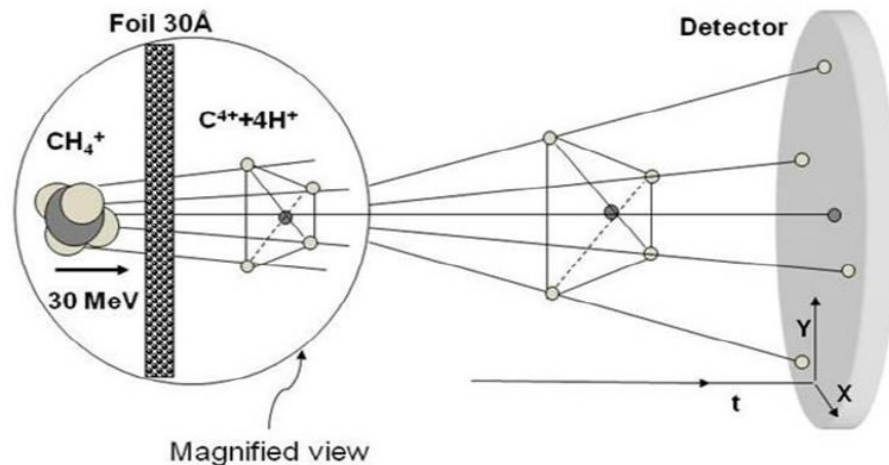


Figure 2.1: Visualization of beam-foil ionization. Reprinted with permission from [50].

ionization methods. One can do pump-probe experiments where the target molecule is *pumped* by a laser pulse to initiate some photodynamics then probed (i.e., Coulomb exploded) by another pulse. The pump and probe pulse can be separated by delays on the femtosecond timescale. A molecular movie can be produced by varying the delay to take snapshots of the molecule as it evolves over time. Time evolved molecular studies can eventually improve our understanding of many ultrafast processes such as protein-folding, photosynthesis, DNA mutation, and liquid-phase collisions.

2.2 Ultrashort Pulses

Ultrashort pulses are extremely short bursts of coherent electromagnetic radiation. Electromagnetic radiation (i.e., light) is the propagation of mutually perpendicular oscillating electric and magnetic fields. For continuous electromagnetic radiation, the electric field is perpetually sinusoidal in time. Electromagnetic pulses are packets of electromagnetic radiation that consists of a finite number of sine waves or E-field cycles. If you were able to see an ultrashort light pulse, it would be an exceedingly thin wall or disc of light travelling through space at light speed. The thickness of this disc of light can be described in metres or time; the latter being the norm. The two measurements can be interchanged using the speed of light (i.e., $c = \frac{\Delta d}{\Delta t}$, so the thickness of a 10 fs pulse is: $\Delta d = c \times \Delta t = c \times 10^{-15}$

s = 3 μm).

Atoms and molecules are made up of protons and electrons. Molecules consist of atoms which are bonded by their electrons. Chemical bonds have electric field strengths that exceed the electric field strengths of most forms of everyday light in the human world (i.e., light emitted from a lamp). Ultrashort laser pulses possess extraordinarily strong electric fields which can be attributed to their brevity in duration. Some basic physics equations can help illustrate this.

The intensity of an ultrashort pulse is the square of the magnitude of its electric field:

$$I(t) = |E(t)|^2 \quad (2.2)$$

Intensity is defined as power per unit area:

$$I(t) = \frac{P}{A} \quad (2.3)$$

Power is defined as energy per unit time:

$$P = \frac{E}{t} \quad (2.4)$$

The power of a pulse is then calculated by dividing its total energy by its duration. The duration of an ultrashort pulse is on the femtosecond timescale (1 fs = 10^{-15} s). The brevity of pulse duration enables pulses to have extremely high peak powers if they have sufficient energy (which they do through the amplification process - see Chapter 2.4). It gets better. Use a focusing mirror to concentrate that power onto a tiny area and the result is an exceedingly high intensity. The electric field then is the square root of that intensity which is still a significantly large number. Amplified ultrashort pulses possess electric field strengths comparable and in excess of those which bind electrons to atoms. This gives them the ability to interact with molecules in useful ways.

2.3 Ti:Sapphire Oscillator - Ultrashort Pulse Generation

Ti:Sapphire oscillators have become the most common generators of ultrashort pulses due to their large gain bandwidth. Ti:Sapphire is short-form for titanium-doped aluminum

Pulse duration	<12 fs
Spectral width	>75 nm
Output power (avg.)	>300 mW
Repetition rate	75 MHz
Pulse energy	>4 nJ

Table 2.1: Oscillator specifications

oxide crystal, $\text{Ti}^{3+}:\text{Al}_2\text{O}_3$. Ti:Sapphire oscillators generate ultrashort pulses through a technique known as mode-locking where almost all the modes of the laser cavity oscillate with the same initial phase and have constant phase differences. In this mode-locking regime, the phases periodically interfere constructively to produce high-amplitude pulses with short durations. The pulse duration τ_p is related to the number of cavity modes m and spectral bandwidth $\Delta\omega$ by [37, p. 59]:

$$\tau_p = \frac{4\pi}{m\Delta\omega} \quad (2.5)$$

Ti:Sapphire is special in that it has the broadest emission bandwidth of any gain laser gain medium and the highest number of modes on the order of 10^4 . The result is a cavity which can produce extremely short pulses on the femtosecond timescale. What is more is that Ti:Sapphire crystals exhibit strong absorption within 400 nm to 600 nm, falling very nicely in the range of the robust and reliable frequency doubled Nd:YLF or Nd:YAG lasers. Ti:Sapphires are currently the most commonly used gain media for ultrashort infrared pulses.

2.3.1 Oscillator Design

The specifications of our Ti:Sapphire oscillator can be found in Table 2.1. The internal optics can be found in Fig. 2.2. The spectrum can be seen in Fig. 2.3.

2.4 Chirped Pulse Amplification System

The Chirped Pulse Amplification (CPA) system employs the Nobel prize winning CPA technique [44] to add energy to the seed pulses while maintaining femtosecond timescale duration.

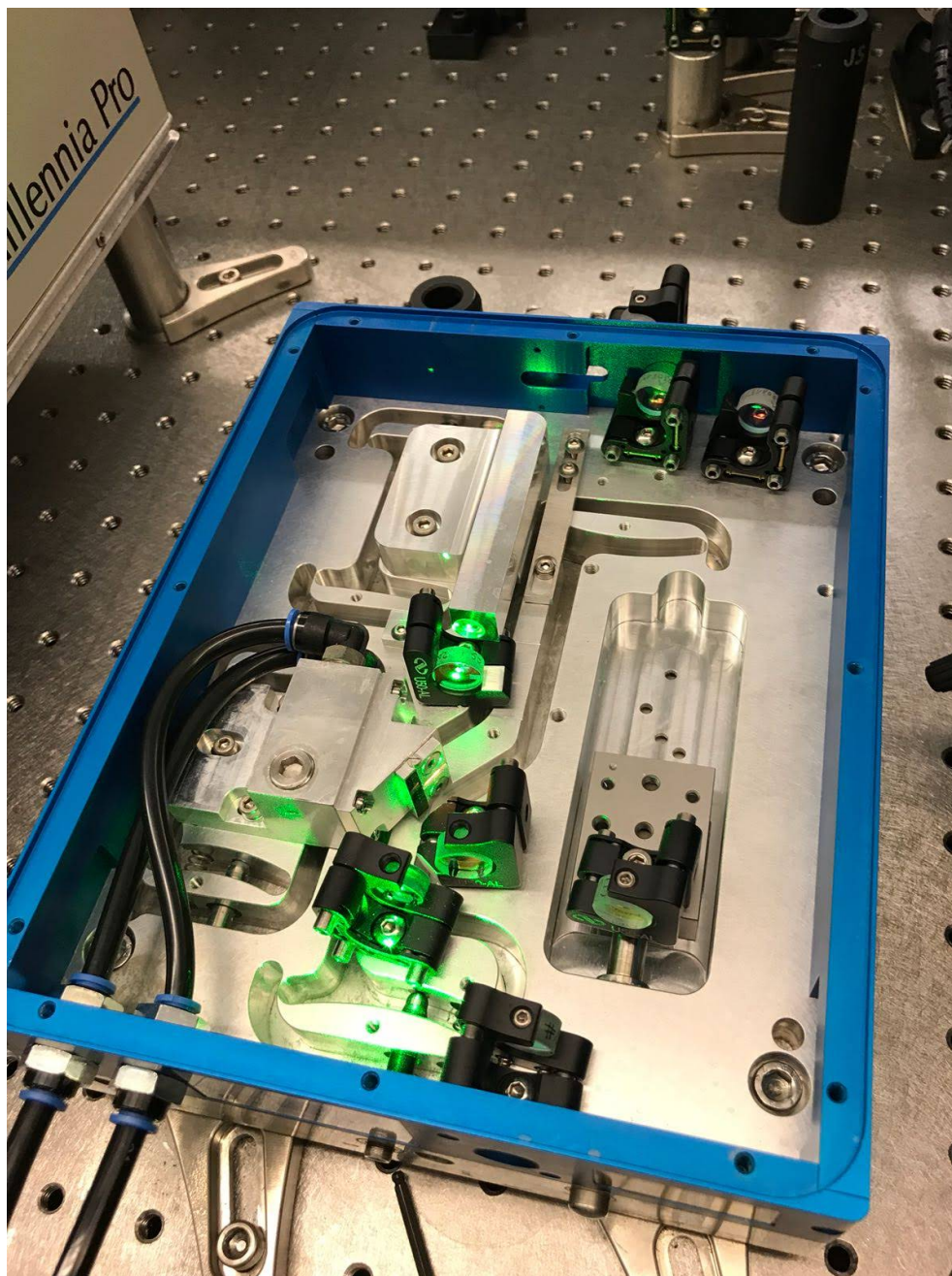


Figure 2.2: Oscillator with the roof removed to reveal the internal optics

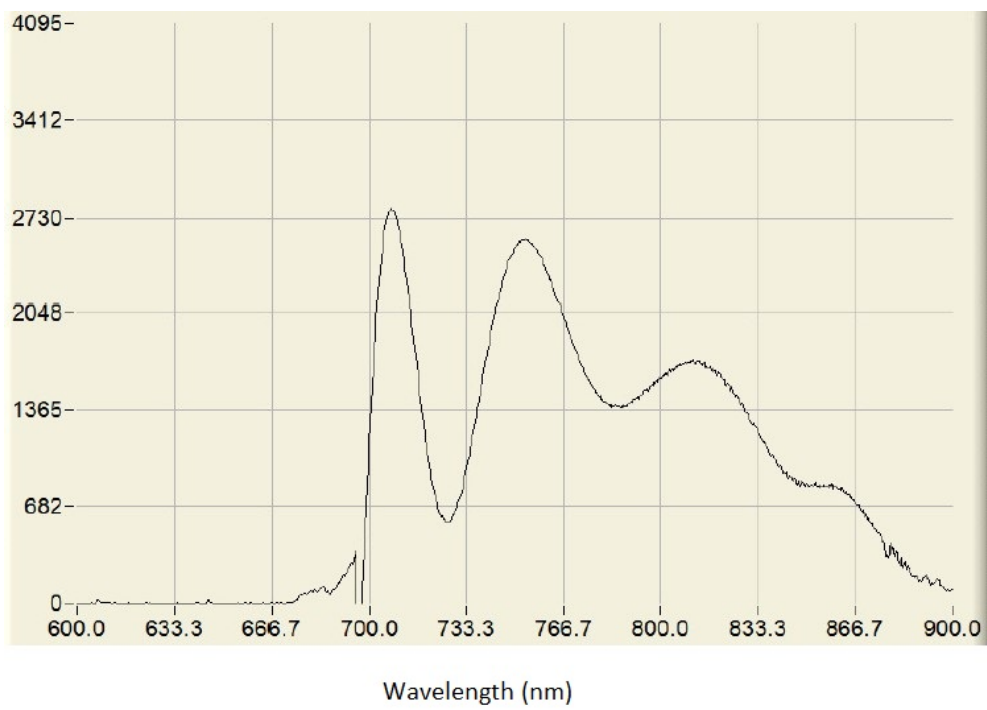


Figure 2.3: The measured spectrum of the oscillator.

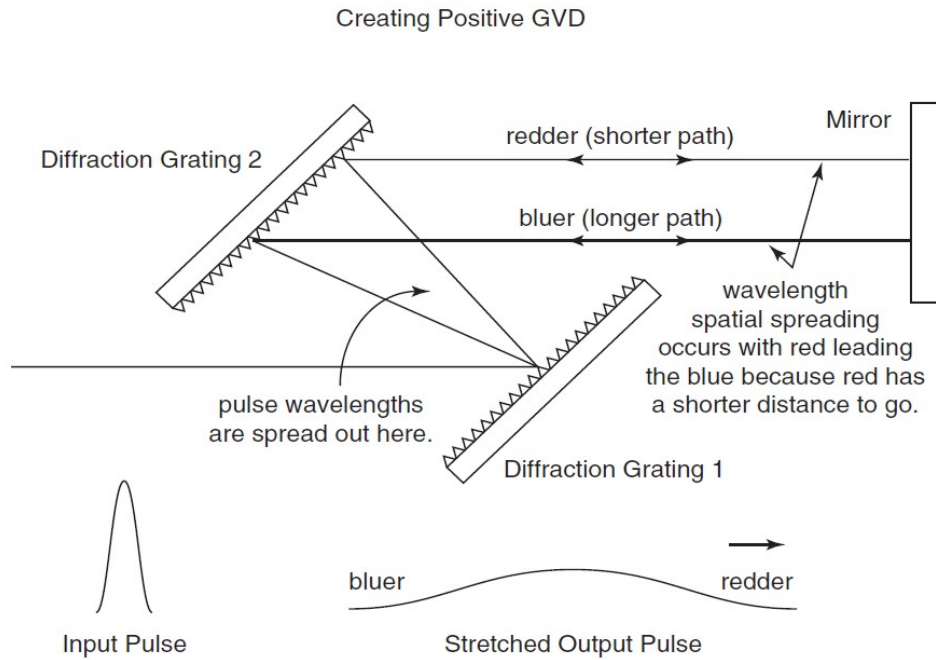


Figure 2.4: Diffraction grating stretcher using positive GVD (from [42, p. 3-5])

CPA is a three step process: pulse stretching, amplification, and pulse compression. The pulse must be stretched before amplification to reduce the peak power which prevents damage to the crystal. After amplification, the pulse is compressed back to its original time domain.

The oscillator pulses are fed into the Spitfire Ace CPA system through a port opening directly to the pulse stretcher. Stretching of a pulse can be done with two diffraction gratings such that incident light pulses are spectrally dispersed onto a second diffraction grating which collimates the pulses but leaves them spatially spread as shown in 2.4. The Spitfire Ace simplifies this design by using a single diffraction grating and a retroreflector mirror which reflects the pulses back onto the grating.

Once the pulses are stretched, the peak power is significantly reduced to prevent damage in the Ti:sapphire crystal during amplification. The pulses are directed into a pulse selector for retention and amplification in the amplifier cavity. Since the oscillator's repetition rate is on the MHz scale, not every single pulse can be amplified because the timing of the amplification process is much longer than the interval between the oscillator pulses. The repetition rate is reduced to 1 kHz to provide ample amplification. Amplifiers need to

Pulse duration	35 fs
Output power (avg.)	5 W
Repetition rate	1 kHz
Pulse energy	>5 mJ
Beam diameter	10 mm
Central wavelength	800 nm

Table 2.2: Regenerative amplifier Spitfire Ace-35F specifications

trade repetition rate for pulse energy, i.e., the lower the repetition rate, the higher the amplification of pulse energy. Pulse selection is done using electro-optic devices known as Pockels cells. A Pockels cell is a crystalline material which responds to an applied voltage and can act as a 1/4 waveplate that rotates transmitted light by 45°. Thus, two passes through an energized Pockels cell will rotate transmitted light by 90°. Pulses then can be selected from the MHz train of seed pulses with the proper timing of activating the Pockels cell with a polarizer mirror to trap pulses of certain polarization in the amplifier cavity. The other pulses are discarded. The pulse makes many passes through the Ti:sapphire crystal, acquiring energy with each pass. The Nd:YLF 527 nm pump laser falls nicely in the Ti:sapphire crystal’s absorption band which excites electrons just before the seed pulses passes through the crystal to stimulate the emission of infrared photons. Proper timing retains the pulses in the cavity for enough passes to saturate the gain (absorb all of the available energy in the crystal). The compressor system works the same way as the pulse stretcher in the opposite way.

2.4.1 CPA System Design

The CPA system is a Spitfire Ace-35F model from Spectra-Physics. The specifications are shown in Table 2.2. The layout of the Spitfire can be seen in Fig. 2.5. The measured spectrum can be seen in Fig. 2.6, exhibiting a central frequency of 798.8 nm and full-width at half maximum (FWHM) of 32.8 nm.

2.5 Coulomb Explosion Imaging Principles

The workflow of a general CEI experiment can be described as follows: ultrashort pulses are generated and shaped as desired, the pulses are characterized to ensure they possess the desired properties, the pulses induce Coulomb explosions of molecules, the fragments are

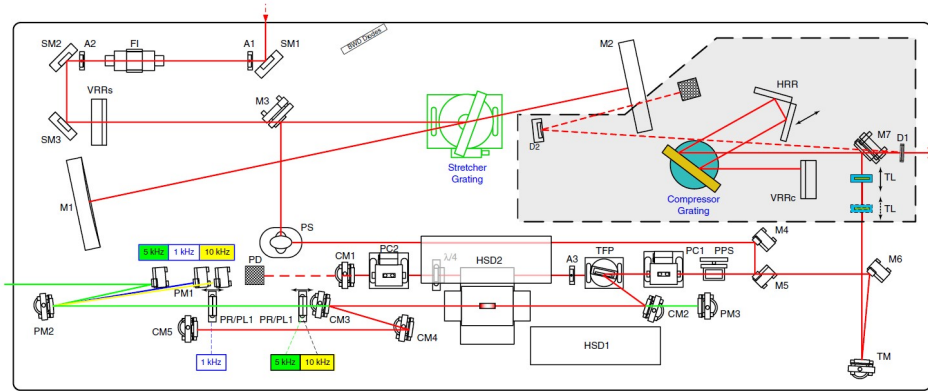


Figure 2.5: Schematic layout of Spitfire Ace-35F from Spectra-Physics (from [42, p. 8-1])

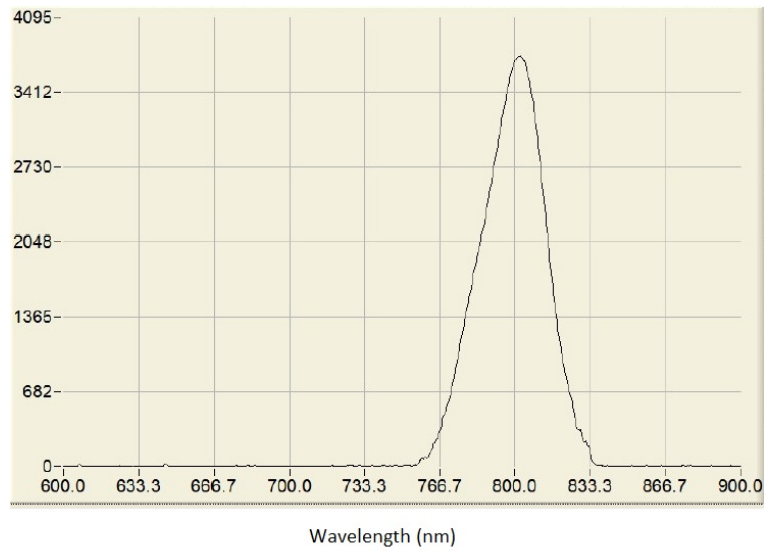


Figure 2.6: Measured spectrum of the Spitfire Ace with a central frequency of 798.8 nm and full-width at half maximum (FWHM) of 32.8 nm.

detected with position and time information which is used to infer the molecule's initial geometry.

Gaseous target molecules are effused into the CEI chamber, randomly bouncing around in the chamber until they find their way into the focal volume of an ultrashort pulse. Once they are engulfed in the volume they are rapidly stripped of electrons and their bonds broken. The ionic fragments of the molecule then accelerate away from each other due to the Coulomb repulsion force.

The Coulomb force law defines the force between two charges in space,

$$F_c = \frac{1}{4\pi\epsilon_o} \frac{q_1 q_2}{|\vec{r}_1 - \vec{r}_2|^2} \quad (2.6)$$

where ϵ_o is the electric permittivity of free space, q_1 and q_2 are point charges, and \vec{r}_1 and \vec{r}_2 are their corresponding position vectors. The electric potential energy associated with the Coulomb force for two charges is:

$$E(|\vec{r}_1 - \vec{r}_2|) = \frac{1}{4\pi\epsilon_o} \frac{q_1 q_2}{|\vec{r}_1 - \vec{r}_2|} \quad (2.7)$$

The period of time from ionization until the repulsion force between each ion becomes negligible can be referred to as the *Coulomb repulsion time*. During this period, the ions are being accelerated exclusively by their mutual repulsive forces. We ignore the acceleration due to the uniform electric field since it is negligible with respect to the Coulomb repulsion forces. At the instant this process begins, the total energy of the system of charged ions is in their potential energies. For example sake, let us assume a triatomic molecule was Coulomb-exploded, the total energy at t=0 is:

$$E_{total} = PE_1 + PE_2 + PE_3 \quad (2.8)$$

$$E_{total} = \frac{1}{4\pi\epsilon_o} \frac{q_1 q_2}{|\vec{r}_1 - \vec{r}_2|} + \frac{1}{4\pi\epsilon_o} \frac{q_1 q_3}{|\vec{r}_1 - \vec{r}_3|} + \frac{1}{4\pi\epsilon_o} \frac{q_2 q_3}{|\vec{r}_2 - \vec{r}_3|} \quad (2.9)$$

As the process progresses over time, the distance between each ion increases, causing the electric potentials to asymptotically approach zero; the potential energies convert to kinetic energy. At the end of the process (when the Coulomb force becomes negligible), the total energy of the system is in the kinetic energies of the ions:

$$E_{total} = KE_1 + KE_2 + KE_3 \quad (2.10)$$

$$E_{total} = \frac{\vec{p}_1^2}{2m_1} + \frac{\vec{p}_2^2}{2m_2} + \frac{\vec{p}_3^2}{2m_3} \quad (2.11)$$

Once the Coulomb repulsion process is over, the time-of-flight process begins where the ions feel no Coulomb repulsion. At time zero of the time-of-flight process, the ions are imparted initial momenta, \vec{p}_1 and \vec{p}_2 and \vec{p}_3 , from the Coulomb repulsion process. Within these momentum vectors lie all of the recoverable geometric information of the molecule prior to ionization. A momentum vector is related to the Coulomb force by:

$$\vec{p} = \int_0^\infty F_c(\vec{t})dt \quad (2.12)$$

where F_C is defined in Eqn. 2.6. Unfortunately Eqn. 2.12 is not invertible. Thus, if one knows the momentum vectors for a triatomic molecular explosion, the exact geometry cannot be determined [51, p. 6]. CEI, then, does not explicitly measure molecular geometries. It simply provides pertinent information subject to interpretation by some arbitrary imaging algorithm. A geometry reconstruction algorithm can be used, as the name suggests, to attempt to reconstruct the original geometry of the molecule as discussed by Ramadhan in [36].

The three-dimensional ion momentum vectors can be determined using their measured time and position tuple, (x,y,t):

$$p_x = m \frac{x - x_0}{t} \quad (2.13)$$

$$p_y = m \frac{y - y_0}{t} \quad (2.14)$$

$$p_x = \frac{qE}{2} \frac{t_0^2 - t}{t} \quad (2.15)$$

where q is the ion's charge, E is the uniform electric field of the TOF spectrometer, x_0 and y_0 are the positions where the ion would have landed on the detector from its original location in the absence of Coulomb repulsion (referred to as the ion's zero positions), and t_0 is the flight time of an ion in the absence of Coulomb repulsion (known as the ion's zero time).

2.6 Experimental Design and Techniques

The CEI experimental setups comprised three main components: optics, electronics, and mechanical systems. The optical systems are described in their own sections: pulse generation (Section 2.3), pulse amplification (Section 2.4), pulse compression (Section 3), and pulse characterization (Section 4). Electronics play a major role in the experiment, which consist of ion trajectory control, ion detection, and data acquisition. The mechanical systems in this case are specifically referring to the CEI chamber and time-of-flight (TOF) apparatus. This section will describe the electronic and mechanical components of the system. Both sets of components can become quite intertwined.

The CEI chamber is a vacuum chamber which houses all of the apparatus for Coulomb explosion measurements. High vacuum in the Coulomb explosion chamber is preferable in order to minimize experimental noise. Thus, it must be constructed entirely of vacuum compatible components able to take on high enough heat for vaporizing water molecules. The vacuum chamber is constructed of stainless steel with a copper gasket seal. The roof of the chamber has a knife edge which bites into the copper gasket when tightened, forming a vacuum seal. A vacuum turbo pump backed by a diaphragm pump evacuates the chamber, maintaining vacuum pressures normally at approximately 1.3×10^{-10} Torr as measured by a cold cathode gauge.

Within the vacuum chamber sits a position-sensitive time-of-flight mass spectrometer (PSToFMS). It differs from conventional time-of-flight mass spectrometers in that it is not only able to measure time of flight of an ion but also its position. Time and position information is recorded as a tuple of data: (x-position, y-position, time of flight) or (x,y,t).

A PSToFMS works by accelerating ions through an electric field of known strength toward a position- and time-sensitive detector. The time taken by each ion to the detector is dependent on its mass-to-charge ratio multiplied by an experimentally determined proportionality constant related to the electric field and distance travelled. The time is measured by a clock which begins when it receives a laser trigger signal and ends when the ion is detected. The theoretical equation for time of flight can be derived as follows.

The potential energy PE experienced by a particle of charge q in a uniform electric field with potential difference V is given by:

$$\text{PE} = qV$$

If d is the distance between two points in a uniform electric field E , the voltage can be expressed as:

$$V = Ed$$

Then we have,

$$\text{PE} = qEd$$

This potential energy plus the initial kinetic energy, KE_i , is converted to the final kinetic energy of the charged particle, KE_f , such that,

$$\begin{aligned} \text{PE} + \text{KE}_i &= \text{KE}_f \\ qEd + \text{KE}_i &= \frac{1}{2}mv_f^2 \\ v_f &= \sqrt{\frac{2}{m}}\sqrt{qEd + \text{KE}_i} \\ \frac{dd}{dt} &= \sqrt{\frac{2}{m}}\sqrt{qEd + \text{KE}_i} \\ \int_{t_o}^t dt &= \sqrt{\frac{m}{2}} \int_0^d (qEd + \text{KE}_i)^{-\frac{1}{2}} dd \\ t - t_o &= \frac{\sqrt{2m}}{qE} \sqrt{qEd + \text{KE}_i} \end{aligned}$$

Finally, we arrive at an expression for time of flight,

$$t = \frac{\sqrt{2m}}{qE} \sqrt{qEd + \text{KE}_i} + t_o \quad (2.16)$$

where t_o represents the time offset due to the electronics. Generally, we can ignore the initial kinetic energy since it is negligible in comparison to the potential energy due to the electric field.

The potential energy on C^+ ion due to our typical applied voltage of 3000 V is:

$$\begin{aligned} \text{PE} &= qV \\ \text{PE} &= (e^-)(3000\text{V}) \\ \text{PE} &= 4.81 \times 10^{-16}\text{J} \end{aligned}$$

Compared to the most probable kinetic energy of C^+ at 25 °Celsius [22]:

$$KE = 5.39 \times 10^{-21} \text{ J}$$

Thus, the initial kinetic energy is 5 orders of magnitude smaller than the potential energy due to the extraction field. So we can ignore the initial kinetic energy and arrive a simplified expression for time of flight,

$$t = \sqrt{\frac{2d}{E}} \sqrt{\frac{m}{q}} + t_o \quad (2.17)$$

Ions can be identified using a calibration technique described in Chapter 2.7.1 where $\sqrt{\frac{2d}{E}}$ becomes a proportionality constant.

The position of the ion is detected with a position sensitive detector (PSD). The PSD consists of a microchannel plate (MCP) coupled to a position sensitive anode known as a modified backgammon method with weighted capacitors (MBWC) anode [28]. The MCP receives an ion which initially produces a small number of electrons eventually amplifying into a cascade of electrons through its multiplying mechanism. The barrage of electrons is then cast upon the position sensitive anode which produces an electrical signal to four of its output ports on each corner. The signal strength of each port receives depends on its proximity to the electron barrage, i.e., the closer the cloud of electrons, the stronger the signal. Thus, a ratio of signal strengths can be taken to determine the position of the electron barrage on an x-y axis as shown in Fig. 2.7.

The PSToFMS has two main components: the extraction region and the detector. The extraction region is the stack of charged metallic plates which are separated equidistantly. Its function is to provide a uniform electric field to send ions to the detector (Fig. 2.8). The uniform electric field is generated by applying a voltage across the extraction region. Uniformity is achieved by ensuring equal spacing between plates and equally decrementing the voltage in magnitude from one end of the stack to the other end. Voltage is decremented using identical resistors between each metallic plate to create a voltage divider circuit. Equidistant spacing is done by using precision-cut identical Teflon spacers between each plate. The detector of course functions to measure the time and position of the ionic fragments. In normal operation, the detector sits atop the extraction region. Both the detector and stack of plates have sets of four holes which allow four threaded rods to be passed through them. The four rods are suspended from the top of the CEI vacuum chamber and the TOF spectrometer can be fastened to them. Teflon material was selected

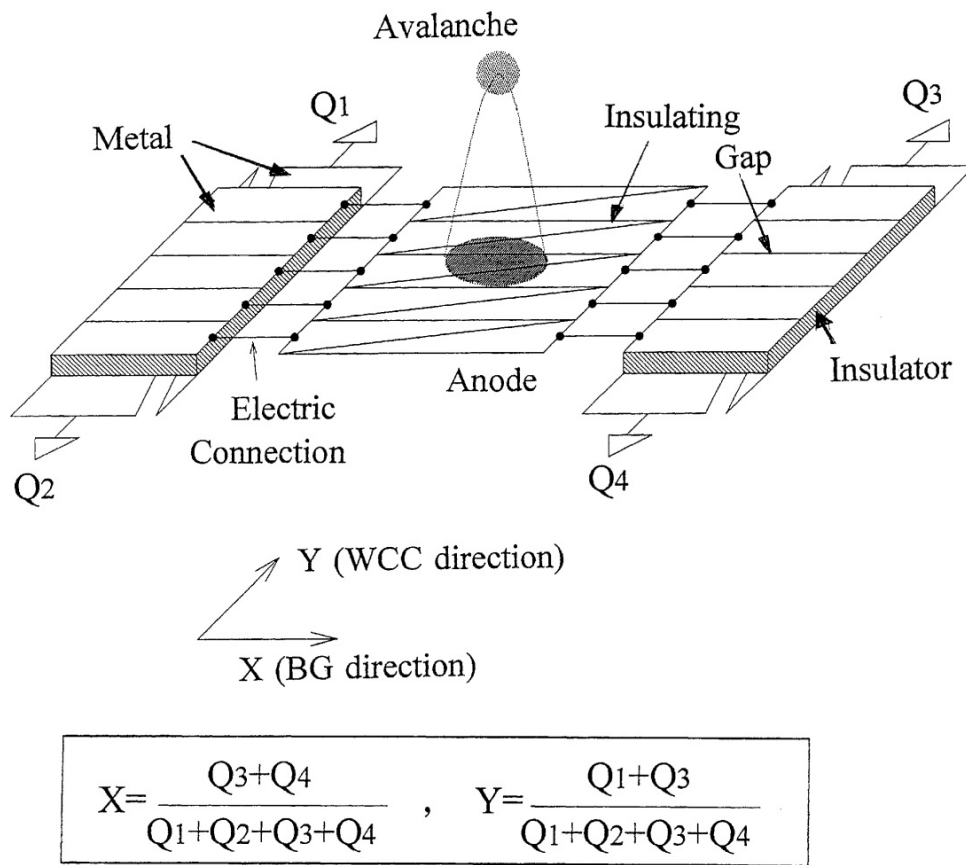


Figure 2.7: MCP with 4 signal. Reprinted from [29] with permission from Elsevier.

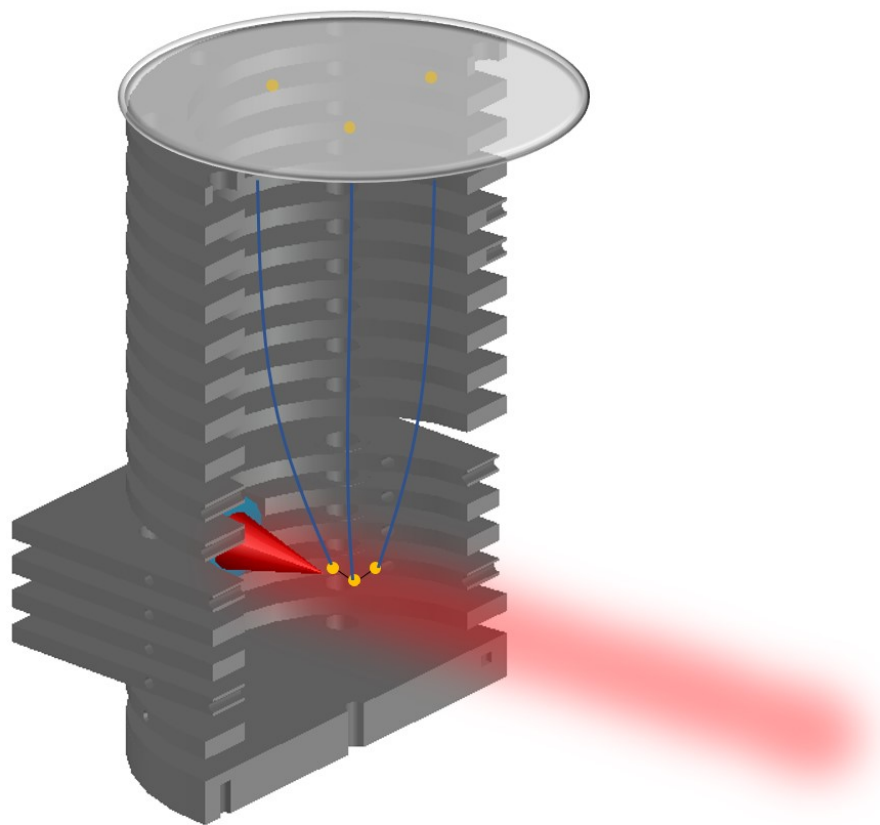


Figure 2.8: Visualization of the ion time-of-flight process after a Coulomb explosion in the TOF spectrometer.

for mounting and spacing since it is a great insulator with high heat resistance and vacuum compatibility. The PSToFMS can be seen in Fig. 2.9.

A parabolic focusing mirror is mounted onto the TOF stack to ionize molecules at the cross-sectional centre of the extraction region (looking from above). The Teflon mount sits between two plates. See Section 2.8 for discussion on the mirror mount.

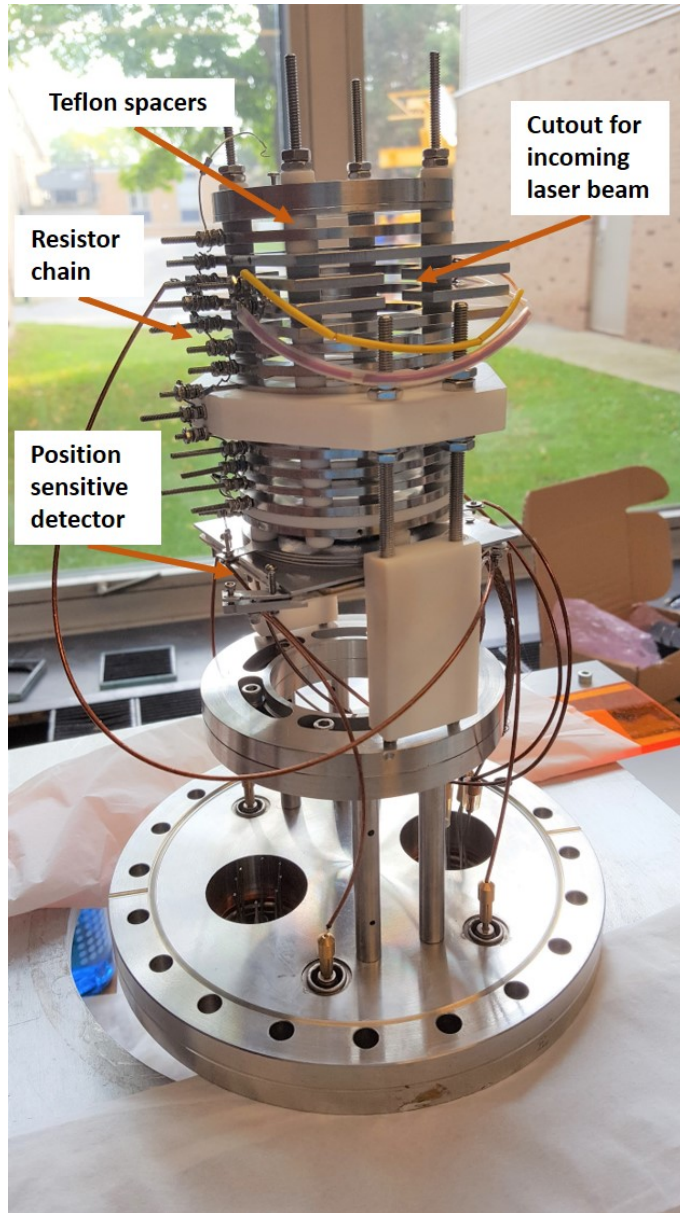


Figure 2.9: The TOF spectrometer oriented upside down as compared to normal operation. Each metallic plate (electrode) is separated by equally thick Teflon spacers. The stack is suspended from the flange by four threaded rods. There is a cutout to make the parabolic focusing mirror accessible to the laser beam. The resistor chain acts as a voltage divider circuit for the electrodes.

2.7 Experimental Data Acquisition and Analysis

The ion MCP discussed in Section 2.6 has 4 output signals that are detected by the DAQ system. These 4 signals provide position information about the ion by analyzing their ratios. The signals occur at the same time, so they are time stamped to provide time of flight information. An example of the signals that the DAQ system receives can be seen in Fig. 2.10. There is a single step in each of the signals indicating the detection of a single ion. The ratios of the signals determine its position (x,y), and the time of the signal step indicates the ion time of flight (t). Thus a tuple of data can be extracted for each ion with x-position, y-position, and time of flight: (x,y,t). Tuples are only recorded if all ions detected for a single laser pulse corresponds to the same molecule (i.e., if an H⁺ ion and an Ar⁺ ion is detected for a single laser shot, they could not have come from the same molecule, so the tuples are discarded). This is done by running the data through a coincidence algorithm developed by Wales et al. in [53]. Thus, not every laser shot will produce coincidence data since a single pulse may ionize more than one molecule.

2.7.1 Time-of-flight Histogram

A time-of-flight spectrum can be produced by plotting a histogram of flight times for all of the detected ions as shown in Fig. 2.14 and 2.15.

Ion Time-of-Flight Calibration

From Eqn. 2.17, we can substitute in a proportionality constant to obtain:

$$t = k\sqrt{\frac{m}{q}} + t_o \quad (2.18)$$

where $k = \sqrt{\frac{2d}{E}}$. Thus, we have an equation of a line (using more common notation, it is in $y = mx + b$ form) where k is the slope of the line and t_o is the y-intercept. If we know two points on this line, we can determine k and t_o . This requires some simple intuition and a small amount of CEI experience. Looking at Fig. 2.15, it should be understood that the lightest element will have the shortest time, hence the first peak must be H⁺. The experiment was done using CO₂, so the highest peak must correspond to CO₂⁺ since its relative pressure will be very high in comparison to the background ions. Thus we can obtain two points from Fig. 2.15 each with a time and a mass-to-charge ratio. These

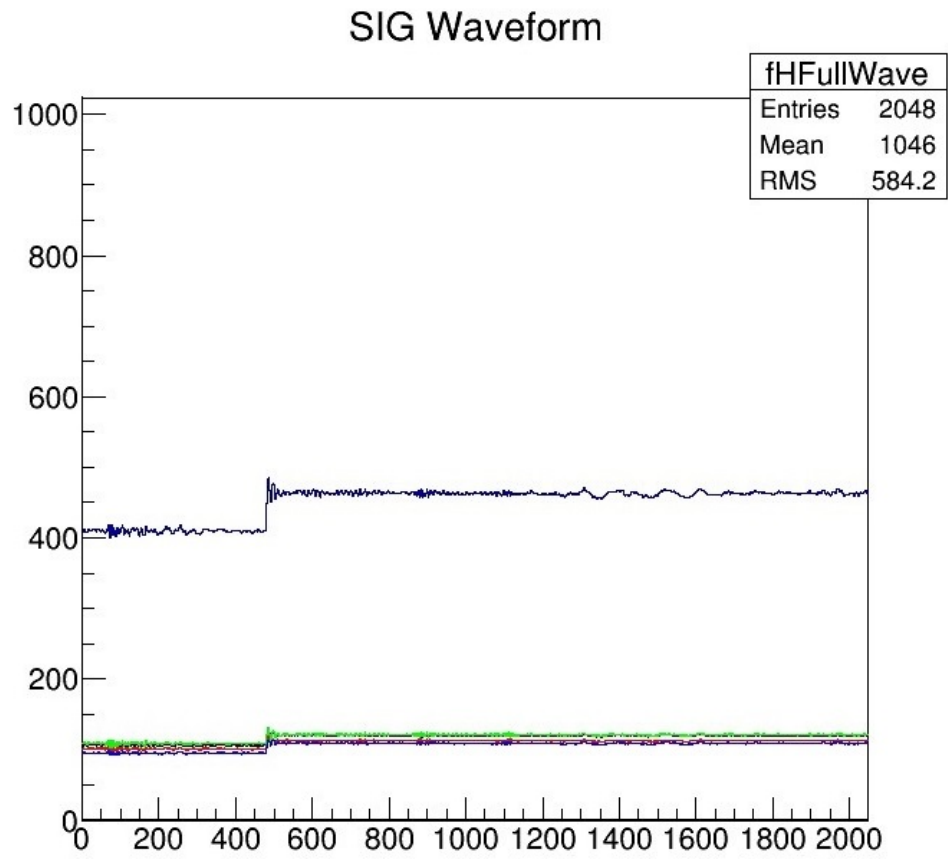


Figure 2.10: Sig waveform showing 4 detection signals (bottom) and their sum (blue signal, top).

two points can be plotted on a t versus $\sqrt{\frac{m}{q}}$ graph. The equation of the line can then be determined using basic geometrical mathematics, i.e., the slope k and y-intercept t_o from equation 2.18 determined. One can pick out peaks from the TOF spectrum and guess the ionic species (the mass-to-charge ratio) and plot the point using equation 2.18 to see if it falls on the line. If it falls perfectly on the line, the guess of mass-to-charge ratio was right. Intuition is sometimes involved to determine the ionic species since a single mass-to-charge ratio may correspond to more than one ionic species (i.e., O_2^+ and S^+ both have a mass-to-charge ratio of 32). This technique is used in Section 2.8.1.

A peak identification algorithm was made using this method where the calibration line is calculated based on two TOF inputs of peaks with known mass-to-charge ratios and likely ionic species are plotted on the TOF histogram to conveniently indicate the source of the peak. The code can be found in Appendix F.3.

2.8 TOF Spectrometer Modification

As part of the CEI imaging apparatus, a focusing mirror is required. The mirror can be mounted in various ways. In our apparatus it is mounted directly onto the TOF stack. In this case the mirror becomes part of the stack and needs to be electrically biased just like the metallic plates to ensure a uniform E-field. The mirror is an aluminum coated parabolic focusing type. The mirror must be placed in a mount that can fit between the two neighbouring plates. The difficulty in proper mounting of the mirror is that the extremely thin aluminum coating must be electrified. The aluminum coating is a thin layer on a concave parabolic face of a cylindrical piece of glass. There is no access to the aluminum coating from behind the mirror (i.e., a hole cannot be drilled through the glass to access the aluminum from the inside since it is extremely thin). The only way to charge the coating is on its mirror face. This presents many problems since it is very sensitive to damage and the laser beam must not be obstructed lest it affect the focal properties.

The single analytical tool used to assess the performance of the PSToFMS before and after the TOF modification is the width of the peaks of the TOF histogram. Eqn. 2.16 can be transformed into an uncertainty relation for TOF:

$$\Delta t = \frac{\sqrt{2m}}{q\Delta E} \sqrt{q\Delta E\Delta d + \Delta KE_i} + \Delta t_o \quad (2.19)$$

where ΔE represents the homogeneity of the electric field, Δd is the spatial distribution

of ionization, ΔKE_i is the initial kinetic energy distribution, and Δt_o is the distribution of time offsets due to the electronics.

The spatial distribution is dependent on the laser and focal parameters of the mirror, the initial kinetic energy distribution is dependent on the target molecule and its thermal energy, and the time offset distribution is dependent intrinsically on the electronics. The homogeneity of the electric field will be affected by geometry of the electrodes in the TOF spectrometer. Since all of the other uncertainties are independent of the TOF spectrometer modifications, only the homogeneity of the electric field, ΔE , will be affected. If we are able to keep all of the experimental conditions constant for both experiments with the exception of the changes due to the TOF spectrometer modification, the only change to the TOF peak widths will be due to ΔE .

Prior to Mirror Mount Modification

Fig. 2.11 shows what the mirror mount looked like prior to modification. The *wing* part of it (the slab of Teflon behind the square-shaped mirror holder) is the piece which fits in between the two adjacent metallic plates. Its thickness was found to be larger than the spacers used in the stack. This caused an asymmetry in the spacing of the plates where the mirror was mounted, shown in Fig. 2.12. Such an asymmetry will certainly warp the otherwise isotropic electric field of the extraction area. The time-of-flight data will then be affected.

The TOF spectrum exhibited abnormally wide peaks as compared to usual TOF peaks produced by the same experimental setup. The assumption is that the wide peaks are a direct result of the large time-spread due to a non-uniform electric field. The warping of the field most certainly must be a result of the deformed TOF stack, but also could have been due in part to the mirror not being electrified continuously. The electrification of the mirror was done by placing two copper beryllium contacts on either side of the mirror, which was wired rather crudely through the Teflon mount to the resistor circuit. Upon removing the mount, the mirror setup was tested for electrical continuity (i.e., to test if the copper beryllium electrodes making proper contact with the surface of the aluminum coating such that the mirror is electrically charged). The mirror electrification was found to be unstable, sometimes it was charged and sometimes it was not, due to the shaky electrodes. *Mis-charging* of the mirror would have played a part in warping the extraction E-field.

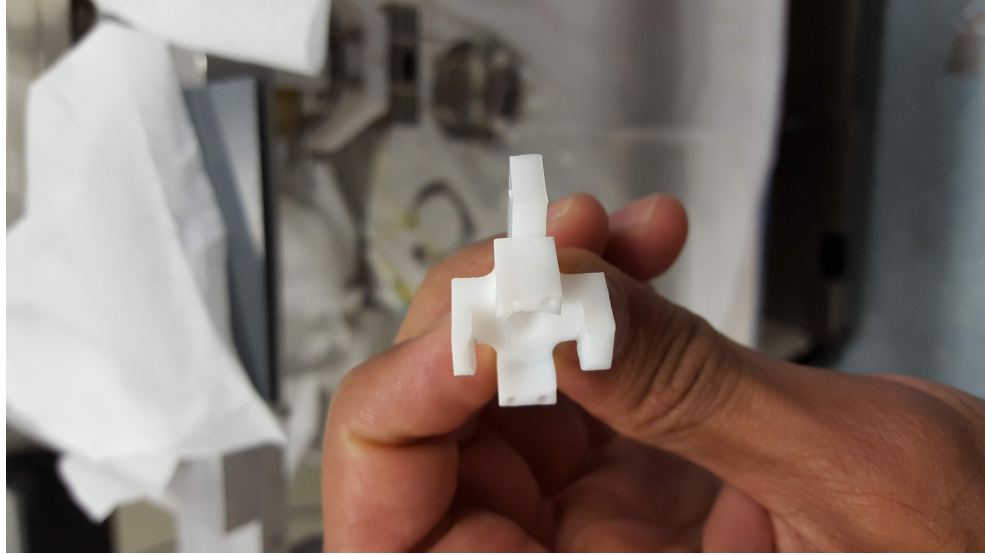


Figure 2.11: Mirror mount prior to modification

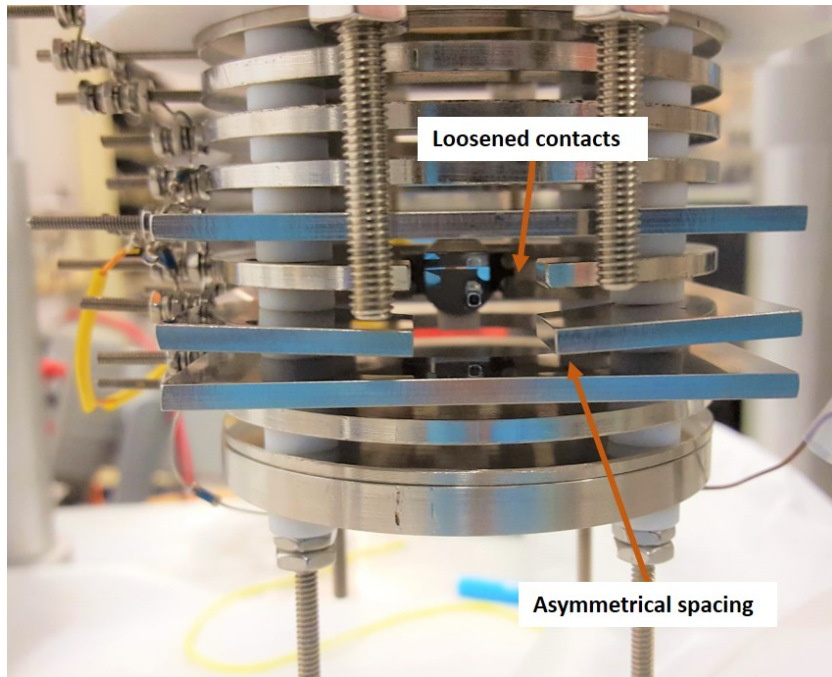


Figure 2.12: Overly thick mirror mount causing the metallic plates to bend outward.

Mirror Mount Modification

The new mirror mount sought to fulfill the following requirements:

1. Fix the spacing problem that caused the deformation of the TOF stack
2. Position the mirror so that the focal point of the laser is at the cross-sectional centre of the extraction field
3. Electrify the mirror with a more stable assembly

The new mirror mount design can be seen in Fig. 2.13. The mount consisted of two main components; the mirror holder and the Teflon *wing*. The wing acted both as a spacer for the metallic plates and an anchor for the mirror holder.

The spacing problem is easily fixed by precision machining the thickness of Teflon wing to match that of the rest of spacers in TOF assembly. The wing extended across the entire length of the metallic plates. This prevented the bending issue that occurred with the previous design where the spacer part was too thick and only spread a small proportion at the centre, causing the plates to bend outward. The wing had a backing that was fastened firmly against the side of the TOF stack.

The sturdier design facilitated more robust contact points for the electrodes on the mirror. Curved shaped copper beryllium electrodes were used to better fit the curvature of the mirror. The assembly was designed to be tolerant to heat since the TOF apparatus has to be regularly baked to remove condensed water. Heating and cooling will cause the materials to expand and contract. The electrodes had a slot in them such that it can fit around a screw which would hold it firmly in place. Thin screws had to be used since there was not much Teflon material surrounding the mirror. The electrodes had to be small enough to avoid any chance of a short-circuit by contacting the adjacent metallic plates. There need only be a single electrode making contact with the mirror, the other electrode is there as a back-up. Two holes were made on either side so that a wire could be fed from the back of the wing to the front of the mirror holder. The screws which clamped the electrodes to the mirror, have heads with small holes in them to allow the wires to be hooked to them. This created a more robust assembly to electrify the mirror with less chance of mis-charging.

Number 2 is also quite straight forward. The focal length of the mirror is 5 cm, so the surface of the mirror must be fixed 5 cm away from the centre of the extraction field. The wing was machined precisely so that it would set the mirror at the correct distance.

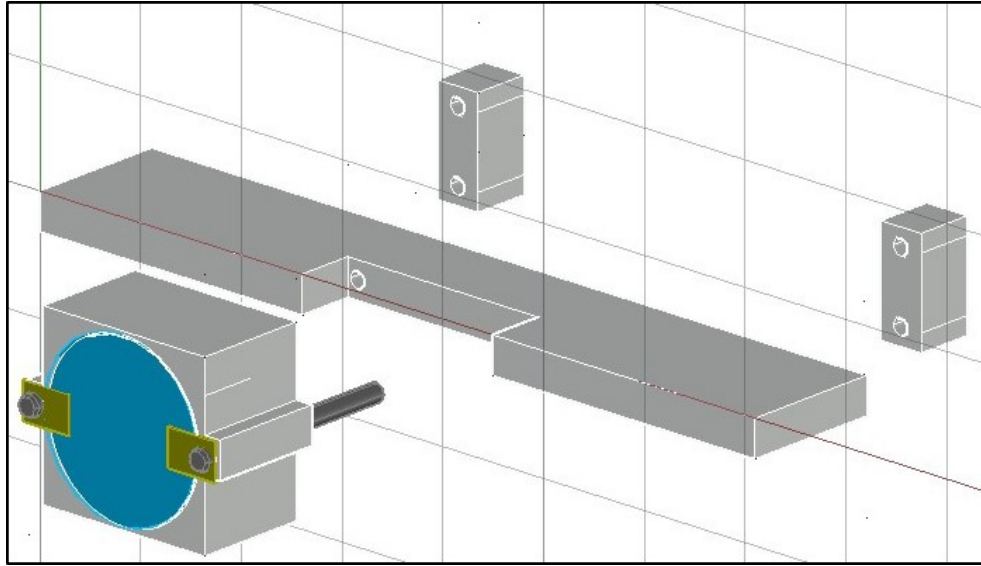


Figure 2.13: Autocad design for the new mirror mount.

2.8.1 Results

Two experiments were done, one before the TOF modification and one after. The experimental conditions which were the same for both experiments were: target molecule of CO_2 , pulse energy, pulse polarization, chamber pressure, and applied voltage on both the extraction region and ion MCP. The conditions which differed were: the changes due to the TOF modification and an apparent difference in relative pressure which will be pointed out.

The TOF histogram from before and after the TOF modification is shown in Figs. 2.14 and 2.15, respectively. By inspection, it is clearly observed that the peaks after the TOF modification are considerably narrower than before. The left-most peak in both plots must be H^+ since it is the lightest ion and will have the shortest flight time. The right-most peak must be CO_2^+ since it has the highest signal as it should since it was the target molecule and therefore had the highest relative pressure (other than H^+ in Fig. 2.14). These peak identifications were confirmed by the calibration method described in Chapter 2.7.1 using the peak identification algorithm in Appendix F.3. There is clearly more background ions in Fig. 2.14. This was likely due to a leak in CO_2 supply which allowed more background ions into the chamber. This cannot have an effect on the the KER or ion space distribution. The only affect it could have on the electronics is saturation of the detector, however this was not the case upon inspection of the detector signal waveforms. There is a possibility

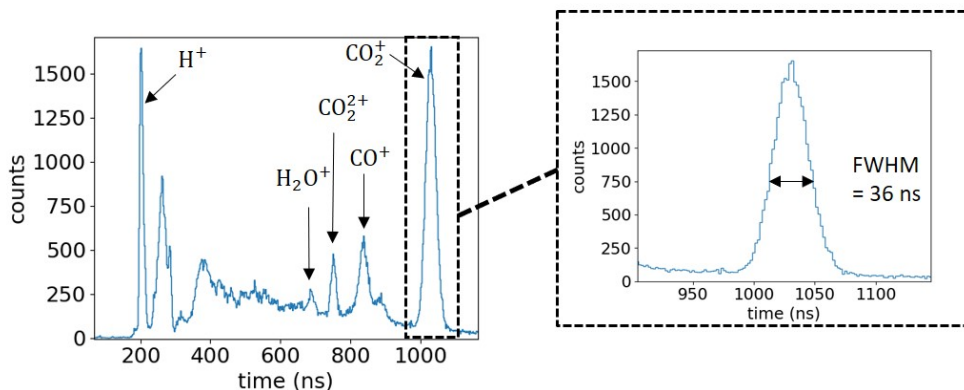


Figure 2.14: TOF histogram obtained using the mirror mount prior to modification.

that the alignment of the laser on the focusing mirror was different in both experiments which would affect the time spread due to the ion space distribution Δt_{space} . The intensity of the focus is dependent on the alignment of the laser and the shape of the focal volume of the pulses are dependent on intensity [10]. However, before each CEI experiment, a precise alignment technique (described in Appendix F.1) was carried out to minimize any change in alignment.

Since all the conditions were kept as similar as possible between both experiments, the changes in the TOF peak widths must be exclusively due to the changes to the geometry of the TOF spectrometer. The flight times were much shorter for the ions after the TOF modification. We can make sense of this if we assume the mirror was not being electrified prior to the modification which was highly supported by the testing that was done and discussed earlier. If this was the case, there would have been a strong decrease in electric field strength in the region proximal to the mirror. Thus the ions may have *drifted* for a period of time before being accelerated by the full-strength extraction field. The problem may have been compounded by the asymmetrical metallic plates from Fig. 2.12 which would have weakened the electric field in that region due to its larger spacing at the centre caused by the overly thick mirror mount.

We can calculate Δt for both TOF plots and compare them. We will look at the CO₂⁺ peaks since they are from the target molecule.

The FWHM of the peak before the TOF modification is calculated:

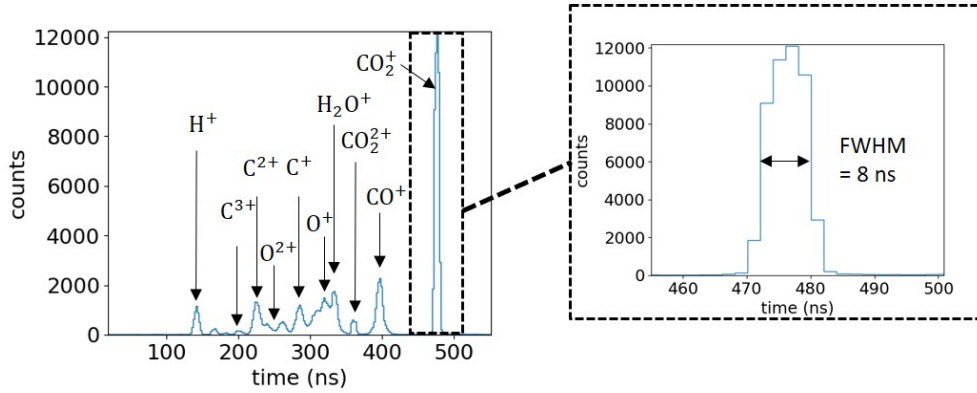


Figure 2.15: TOF histogram obtained using the newly modified mirror mount. The peaks are much more distinguishable than the TOF histogram in Fig. 2.14.

The max signal of the CO_2^+ peak is 1652, giving a half-max of 826.

$$\begin{aligned}\Delta t &= t_{\text{right}}(826) - t_{\text{left}}(826) \\ &= 1048 - 1012 \text{ ns} \\ &= 36 \text{ ns}\end{aligned}$$

And the FWHM of the peak after the modification:

The max signal of the CO_2^+ peak is 12094, giving a half-max of 6047.

$$\begin{aligned}\Delta t &= t_{\text{right}}(6047) - t_{\text{left}}(6047) \\ &= 480 - 472 \text{ ns} \\ &= 8 \text{ ns}\end{aligned}$$

Therefore the CO_2^+ peak after the modification is 77% narrower than the peak before the modification:

$$\left| \frac{36 - 8}{36} \right| = \left| \frac{24}{36} \right| = 77\%$$

We can calculate the time of flight difference for CO_2^+ between both TOF histograms. For complete comparison, the calibration line from the method described in 2.7.1 needs to be calculated for both TOF histograms.

For the TOF histogram prior to modification, we use Eqn. 2.18 and the most probable time of flight (centre of peak) for H^+ and CO_2^+ .

The most probable time for H^+ is 202 ns and for CO_2^+ is 1030 ns.

Thus, we form two equations:

$$202 = k\sqrt{\frac{1}{1}} + t_o$$

$$1030 = k\sqrt{\frac{44}{1}} + t_o$$

Rearrange and set both equal to k :

$$k = 202 - t_o$$

$$k = \frac{1030 - t_o}{12}$$

Now we have:

$$202 - t_o = \frac{1030 - t_o}{12}$$

And solve for t_o :

$$t_o = 0.00147$$

Then solve for k :

$$k = 54 \times 10^{-9}$$

We arrive at:

$$t = 0.00147\sqrt{\frac{m}{q}} + 54 \times 10^{-9}$$

We can do the same calculation for the TOF histogram after modification. It exhibits most probable times of flight for H^+ and CO_2^+ of 142 ns and 476 ns, respectively, resulting in the time-of-flight calibration line equation:

$$t = 0.00059\sqrt{\frac{m}{q}} + 82 \times 10^{-9}$$

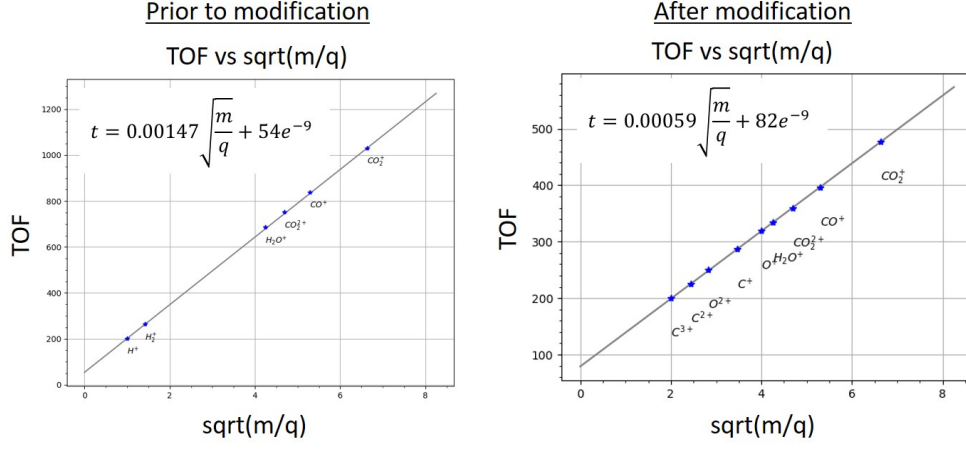


Figure 2.16: The calibration lines for the TOF histograms from prior to and after TOF the spectrometer modification. The most probable times for ionic species are plotted on the line.

The calibration line plots for both TOF histograms are shown in 2.16.

A ratio of both calibration equations can be taken. We can use the most probable arrival times of CO_2^+ and substitute $\sqrt{\frac{2d}{E}}$ in for k :

$$\frac{t_{old} - t'_o}{t_{new} - t_o} = \frac{\sqrt{\frac{m}{q}} \sqrt{\frac{2d}{E'}}}{\sqrt{\frac{m}{q}} \sqrt{\frac{2d}{E}}}$$

where, t_{old} and t_{new} are respectively the old and new arrival time of CO_2^+ ,

t'_o and t_o are respectively the old and new time offsets,

and E' is the old electric field.

$$\frac{1030 - 54 \text{ ns}}{476 - 82 \text{ ns}} = \frac{\sqrt{\frac{m}{q}} \sqrt{\frac{2d}{E'}}}{\sqrt{\frac{m}{q}} \sqrt{\frac{2d}{E}}}$$

Since all variables were kept constant except for the electric field,

we can cancel them and arrive at:

$$\frac{976 \text{ ns}}{394 \text{ ns}} = \sqrt{\frac{E}{E'}} \quad (2.20)$$

From the comparison of times, we can see that there is a 60% decrease in time of arrival of CO_2^+ :

$$\frac{976 - 394}{976} \times 100\% = 60\% \text{ faster}$$

which also means there is an increase in the strength of electric field. We can use the following formula to show this percentage difference:

$$\frac{E - E'}{E'} \times 100\%$$

which shows the percentage change from the old electric field to the new electric field. From Eqn. 2.20, we have:

$$\frac{E}{E'} = \frac{976^2}{394^2}$$

Subtract 1 from both sides:

$$\frac{E}{E'} - \frac{E'}{E'} = \frac{976^2}{394^2} - \frac{394^2}{394^2}$$

$$\frac{E - E'}{E'} = \frac{976^2 - 394^2}{394^2}$$

$$\frac{E - E'}{E'} = 5.13$$

$$\frac{E - E'}{E'} \times 100\% = 513\%$$

Thus, there is a 513% increase in the average strength of the electric field following modifications done to the TOF spectrometer.

Since the homogeneity of the ion extraction field is wholly dependent on the geometry of the TOF spectrometer, its improvement is a direct result of the the modifications done to the TOF spectrometer. The TOF peak width of CO_2^+ narrowed from 36 ns to 8 ns in the new TOF spectrometer. The most probable arrival time of CO_2^+ shortened from 976 ns to 394 ns (accounting for the time offset) indicating a 60% decrease. This decrease in time of flight indicates a 513% increase in average electric field strength.

Chapter 3

Hollowfibre Pulse Compression: Few-Cycle Generation

3.1 Introduction

In Section 2.3 it was alluded to that the Ti:Sapphire crystal in the oscillator was an excellent gain medium for ultrashort pulses due to its particularly broad emission bandwidth. Indeed, there is a direct relationship between pulse duration and frequency bandwidth. For a Gaussian-shaped pulse, the temporal FWHM (Δt) of the pulse's intensity function is related to the frequency FWHM ($\Delta\nu$) of the pulse's power spectrum through the Time-Bandwidth product (TBP):

$$\Delta\nu\Delta t \geq \frac{2\ln 2}{\pi} \approx 0.441 \quad (3.1)$$

This inequality states that the product of the two is constrained in the lower limit to 0.441. When a Gaussian pulse's TBP is 0.441 it is said to be *bandwidth-limited*. A more general version of the TBP is,

$$\Delta\nu\Delta t \geq K \quad (3.2)$$

where K depends on the shape of the pulse.

A bandwidth-limited pulse is as short as it can possibly be given its spectral bandwidth. According to Eqn. 3.2, the temporal width can be decreased only by increasing the spectral

width. However, broadening the pulse’s spectrum does not automatically guarantee a shorter pulse, it simply grants the *opportunity* to achieve a shorter pulse. Pulse compression then relies upon a spectral broadening mechanism to yield a *nonbandwidth-limited* pulse followed by a compressive operation to approach the bandwidth-limit.

Hollowfibre compression is a technique whereby a hollow core fibre exploits nonlinear optical effects to spectrally broaden pulses followed by a re-phasing operation to compress the pulses to the bandwidth limit. Specific to our setup, the hollow core fibre is filled with Argon gas to provide a nonlinear optical medium, and the compressive optical setup is a sequence of ‘chirped’ mirrors.

As a pulse propagates through a nonlinear optical medium it is mainly affected by two phenomena: group velocity dispersion (GVD) and self-phase modulation (SPM) [37, p. 175]. It is well known in nonlinear optics that the refractive index of a nonlinear medium is dependent on the intensity of a pulse, such that,

$$n = n_0 + \frac{1}{2}n_2I(\vec{r}, t) \quad (3.3)$$

where n is the nonlinear refractive index and $I(\vec{r}, t)$ is the light intensity with spatial and time dependencies. The intensity distribution in space is responsible for the Kerr lens effect, which in fact is central to the modelocking process in Ti:Sapphire crystals discussed in Section 2.3. The intensity distribution in time changes the nonlinear index in such a way to bring about changes in the frequency spectrum of a propagating pulse. To understand this phenomenon we can introduce an equation for a propagating pulse in nonlinear media:

$$E(t, x) = E_0e^{i\omega_0t - kx} \quad (3.4)$$

with,

$$k = \frac{\omega_0}{c}n(t) \quad (3.5)$$

where E_0 is the electric field amplitude and ω_0 is the central frequency. The phase can be defined as:

$$\Phi(t) = \omega_0t - kx \quad (3.6)$$

The instantaneous frequency ω_0 is the time derivative of the phase,

$$\omega_0 = \frac{\partial}{\partial t} \Phi = \omega_0 - \frac{\omega_0}{c} x \frac{\partial n(t)}{\partial t} \quad (3.7)$$

The second term in Eqn. 3.7 describes how much the frequency changes with respect to ω_0 ; it is commonly known as the frequency variation $\delta\omega(t)$. It can be obtained by further evaluating $\frac{\partial n(t)}{\partial t}$, to give:

$$\delta\omega(t) = \omega(t) - \omega_o = -\frac{\omega_0 n_2}{2c} x \frac{\partial I(t)}{\partial t} \quad (3.8)$$

Thus, we can see that new frequency components (modulations) are created in the pulse envelope as it propagates through a nonlinear medium. This is the process of SPM. GVD plays an important role as well. Any pulse propagating through a transparent medium suffers dispersive effects. Positive GVD is applied to the new frequency components as they propagate, in other words they are positively chirped (redder in the leading edge, bluer in the trailing edge). Since the pulse is chirped, meaning the frequency is not constant with time (see Fig. 3.1), it is a nonbandwidth-limited pulse. It must be *rephased* so that the bluer components can ‘catch-up’ to the redder components to achieve a flat phase thereby being a bandwidth-limited pulse (maximally compressed). A dispersive optical setup must be used to apply a negative GVD to compensate for positive GVD acquired during propagation. This is done by ensuring the red-shifted components have a longer optical path than the blue-shifted, thus allowing all of the frequency components to arrive in phase. Chirped mirrors can be used for this task which are multilayered to reflect different frequencies at different depths [25]. This can be followed by a pair of silica wedges which can be finely adjusted to vary the thickness of silica traversed by the pulse. The chirped mirrors may apply too much negative GVD, so the silica wedges will provide a tunable amount of positive GVD to compensate.

3.2 Experimental Design and Techniques

The pulses are steered through a polarization-changing periscope, half-wave plate, a focusing lens of 1 m focal length, two beam-steering mirrors, before finally entering the hollowfibre chamber. The chamber is constructed of plastic and sealed by rubber gaskets. The windows of the chamber are silica with the incident window angled downwards to avoid damage to the optical components due to back reflection. The hollow core fibre is a hollowed 1 m silica fibre with a 250 μm inner diameter. It sits inside the chamber atop an

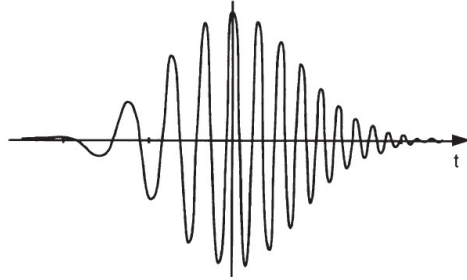


Figure 3.1: Linearly chirped pulse with positive GVD

aluminum cylinder with a wedge cutout. The entire chamber sits on two x-y translation stages, one to control the front of the chamber and the other to control the back. A copper tubing gas line is threaded into the top of the chamber for pressure control. The gas line is connected to a vacuum pump and an Argon gas cylinder. The hollow fibre compressor setup can be seen in Fig. 3.2.

The chamber is filled with Argon gas of certain pressures to create a nonlinear optical medium for the pulses. Pulses of 1 mJ are focused at the entrance of the hollow core fibre where the nonlinear processes are set to begin, then exit to be incident upon a germanium plate. The germanium plate is set at the Brewster angle which will allow power control from the half wave plate: the germanium plate will only reflect vertically polarized light where the proportion of vertical polarization is controlled by rotating the half wave plate. This scheme is an effective way to control power since the SPM process is polarization-independent and thus not affected by the rotation of the half-wave plate. The pulses out of the hollow fibre are diverging since they were initially focused down by a 1 m focal length lens prior to entry. The pulses are re-collimated by a 1 m focal length lens then directed through a sequence of chirped mirrors to compress the pulses. After the chirped mirrors, the pulses go through 2 silica wedges that sit on translation stages, allowing for fine-tuned GVD compensation of the pulses. The final output is a train of pulses which are desired to be bandwidth-limited pulses of much shorter duration than the input pulses.

The spectrometer used was a USB4000 model, manufactured by Ocean Optics. The USB4000 exhibited a loss of detection efficiency as it approached 900 nm. This resulted in some ambiguity in the actual signal intensity near 900 nm.

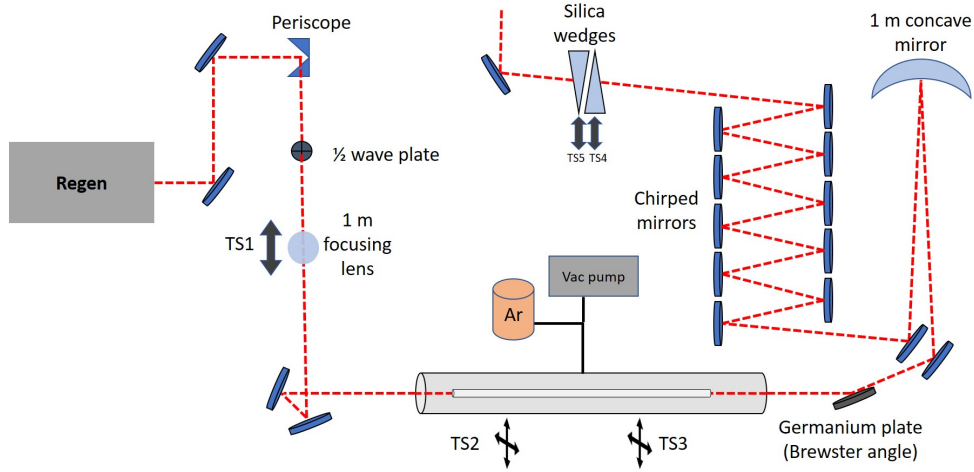


Figure 3.2: Experimental setup of the hollow fibre compressor system.

3.3 Results

The hollow core fibre employed in our experiment was provided by Femtolasers who published their spectral broadening results [11]. Their ideal spectral broadening test result is shown in Fig. 3.3. Naturally, a reasonable goal was to reproduce this spectrum as accurately as possible.

The two main parameters for the hollow fibre pulse outputs were: the compressor position in the Spitfire Ace and the pressure in the hollow fibre chamber. The input energy was kept constant at approximately 1 mJ. The output was also quite sensitive to alignment of the laser and the hollow core fibre, which is not necessarily considered a parameter since it cannot be defined by a single metric but certainly had an effect on the spectrum. The main objective for alignment was to maximize the transmission power while ensuring the output mode was the fundamental mode, the latter being of higher importance.

In order to best match the reference spectrum, an experiment was done to analyze the pressure dependence on spectral width and modulations. For each spectrum taken at a different pressure, the hollow fibre was tuned to an optimized alignment such that the fundamental mode was found. The fundamental mode was increasingly difficult to obtain as the pressure increased. While the pressure affected the spectral width and the number of modulations, the compressor position in the Spitfire Ace had the greatest effect on the spectral profile of the pulses. The compressor in the Spitfire Ace was scanned in both directions until a position was found which produced a spectral profile that best mimicked

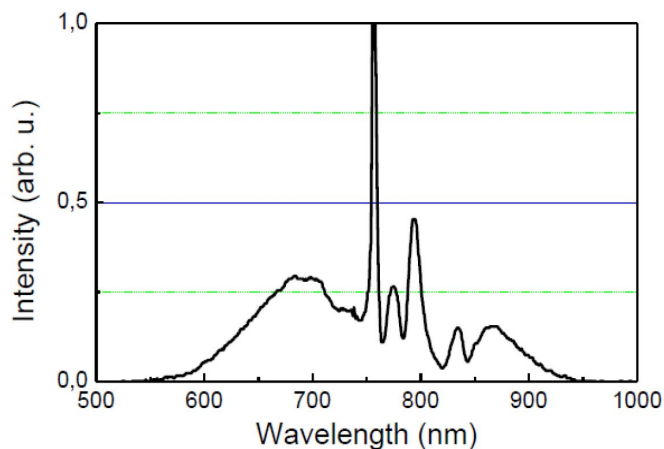


Figure 3.3: Ideal spectral broadening result from [11]

the reference spectrum. The set of spectra is shown in Fig. 3.4 with the pressures and compressor position labelled. The bandwidth and pressure values are tabulated and plotted in Fig. 3.5. The number of modulations and pressure values are tabulated and plotted in Fig. 3.6.

The reference spectrum exhibits 6 modulations and has a bandwidth at full base ranging from approximately 550 nm - 950 nm. Upon inspection of the spectra shown in Fig. 3.4 and analysis of the bandwidth and number of modulations from Fig. 3.5 and 3.6, respectively, it is apparent that the optimal pressure range is 353 Torr to 760 Torr. Thus, we home in on this range of pressures and fine-tune the parameters.

The closest matching spectra to the reference spectrum were produced at 379 Torr. Fig. 3.7 shows the two closest matching spectra, also overlaid on the reference spectrum for comparison.

It is shown that the spectra which best match the reference spectrum from Femtolasers are produced at an optimal pressure of 379 Torr with a compressor position range from 8000 to 8200. The degree of agreement was determined by comparing the bandwidth and number of modulations of the obtained spectra with the reference spectrum. The number of modulations increased with pressure. The spectral profile of the hollowfibre outputs are strongly correlated with the compressor position of the Spitfire Ace. The compressor position will change the amount of GVD that the pulses have prior to entering the hollowfibre system. The compression results can only be analyzed by simulation or by experimental pulse characterization which is discussed in Chapter 4.

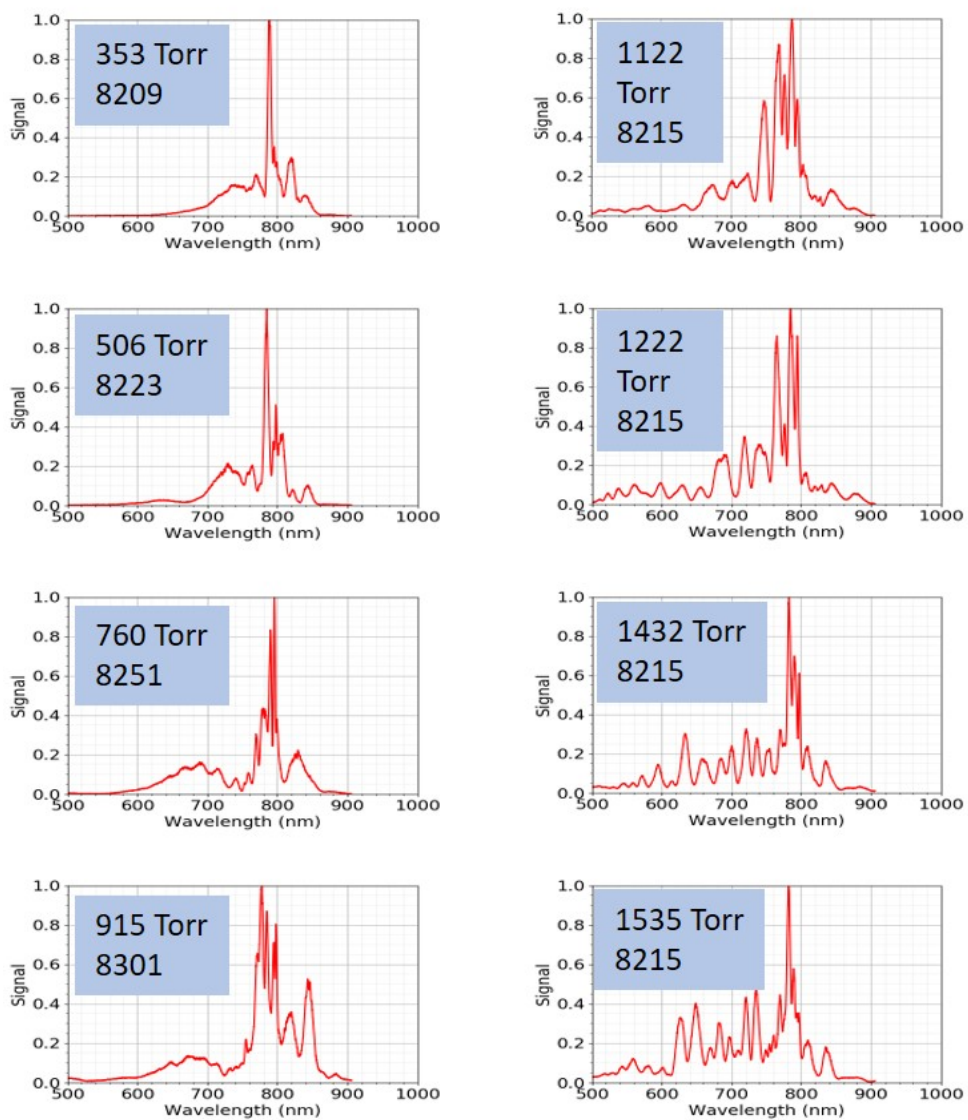


Figure 3.4: Series of spectra with varying pressure and by varying the compressor position of the Spitfire Ace.

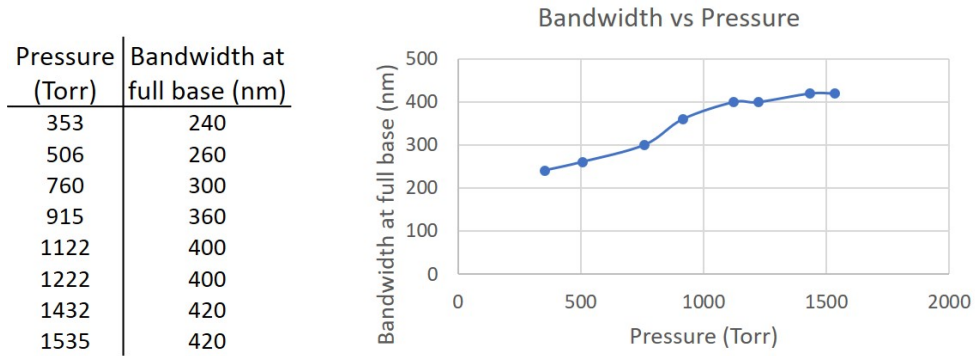


Figure 3.5: Table (left) and plot (right) of bandwidth vs. pressure.

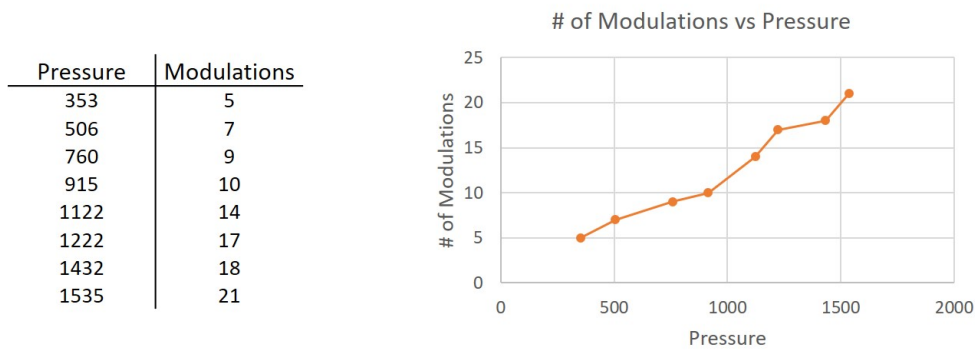


Figure 3.6: Table (left) and plot (right) of the number of modulations vs. pressure.

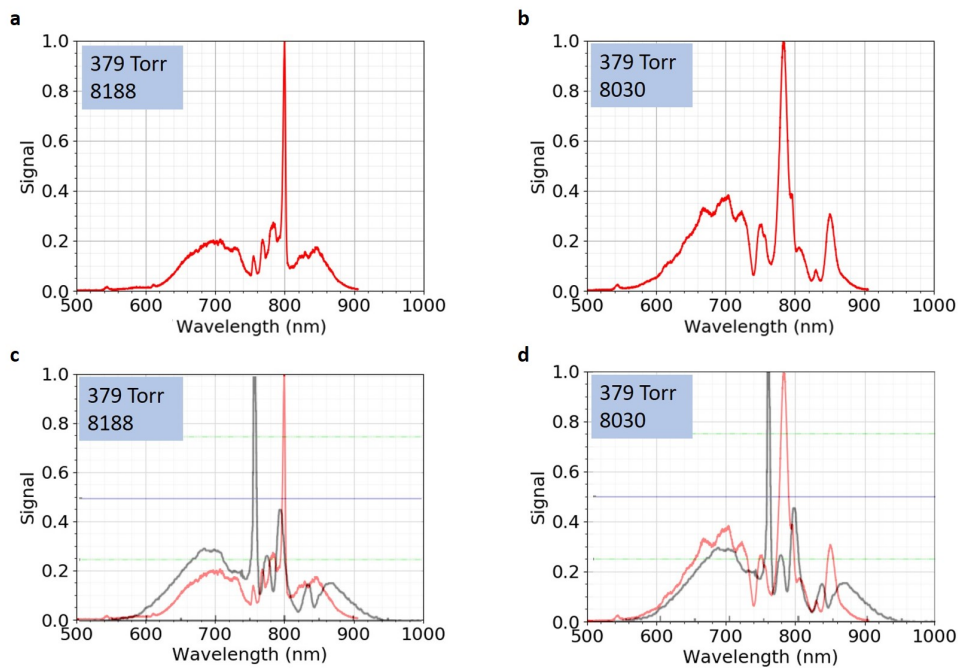


Figure 3.7: (a) and (b) show the two closest matching spectra to the reference spectrum. (c) and (d) show the spectra from (a) and (b), respectively, overlaid on the reference spectrum for comparison. The spectrum in (a) spans from approximately 600 nm to 900 nm and exhibits 6 modulations. The spectrum in (b) spans from approximately 540 nm to 900 nm and exhibits 7 modulations.

Chapter 4

Pulse Characterization

4.1 Introduction

The purpose of ultrashort pulses with respect to this thesis is to measure properties of molecules and study their dynamics. They are tools for molecular imaging. If they are going to be used as tools we ought to know as much about their properties as possible before we begin an experiment. CEI experimenters are generally most concerned about pulse length since it is the most important factor, however the phase can certainly have an effect on the the CEI results [58].

How ever the measurement is made, how can we be confident that the results are accurate? For many measurement techniques, there do not exist robust validation methods to check the results. The frequency-resolved optical gating (FROG) measurement (which encompasses a host of setups that produce a FROG trace) is one of the few methods in which independent checks exist to validate the results.

Ultrashort pulses are among the shortest events that have been created and controlled by humans. Their brevity in duration allow them to measure processes which occur on extremely short timescales. So how can we measure the *measurer*? In order to measure anything, one needs something which is finer in scale than the sample. For example, if we would like to measure the time duration of a single year on earth, we need something which has an event time shorter than a year. We can use the number of times a full moon appears, 12. To determine the periodicity of full moons, we can count the number of sun rises, then count, say, the number of pendulum swings between sun rises and so on. Galileo famously used his heartbeat to time events with a temporal resolution close to 0.1 seconds [49, p.

3]. Modern timing devices utilize fast electronic processes to achieve timing accuracy on the picosecond (10^{-12} s) time scale. Eventually we arrive at an extremely short event: an ultrashort pulse. There really aren't any shorter events in our control, or else we would be using those events instead of ultrashort pulses. The only possible approach is to use the pulse to measure itself. And this is exactly how ultrashort pulse lengths are measured. The most common technique to date where the pulse measures itself is the autocorrelator. It is a fairly simple technique which produces limited information of which is not independently verifiable. The researcher does not necessarily know if the pulse length measurement is truly accurate. Also, the autocorrelator does not measure the phase of the pulse. The FROG technique, however, is much more informative and can be independently verified. Encapsulated in a FROG trace is all of the pertinent information of a pulse: intensity and phase versus frequency, and intensity and phase versus time.

Rick Trebino, one of the inventors of the FROG, has an entire, very well written book dedicated to this topic [49]. Much of these descriptions closely follow the subject of the book.

In Section 2.2, it was mentioned that only the electric field of the pulses are considered in this thesis. Even though we may have simplified the full description of electromagnetic waves by only considering the electric field, still the electric field can be a rather unnecessarily complicated function of space and time for our purposes. We can further simplify things by ignoring the spatial and vectorial properties of the pulse and express the E-field as a scalar with only the temporal dependencies. Thus, we can write the temporal dependence of the pulse's electric field:

$$E_{temporal} = \frac{1}{2} \sqrt{I(t)} e^{i\omega t - \phi(t)} + c.c. \quad (4.1)$$

where $I(t)$ is the intensity ($\sqrt{I(t)}$ then is the electric field magnitude), ωt is the carrier wave, $\phi(t)$ is the phase, and "c.c." is the complex conjugate.

We can take Trebino's approach and the approach of many other books by taking what is known as the analytical signal approximation by ignoring the complex conjugate term and the rapidly varying carrier wave of Eqn. 4.1 and multiply it by 2 to obtain:

$$E(t) = \sqrt{I} e^{i\phi(t)} \quad (4.2)$$

This greatly simplifies the expression for the pulse electric field and the mathematics required while retaining its temporal characteristics. The expression is in time-space but we can also write it in frequency space by Fourier Transformation:

$$\tilde{\mathcal{E}}(\omega) = \sqrt{S(\omega)}e^{i\phi(\omega)} \quad (4.3)$$

where $S(\omega)$ is the power spectrum and $\phi(\omega)$ is the spectral phase.

Thus, in order to obtain a pulse's electric field, which would in turn allow us to completely characterize it, we can do it in either of two ways:

1. For Eqn. 4.2 we work in time-space and determine the pulse intensity $I(t)$ and phase $\phi(t)$
2. For Eqn. 4.3 we work in frequency-space and determine the spectrum $S(\omega)$ and spectral phase $\phi(\omega)$

So what sort of devices can be conceived to characterize pulses? And how many of which are capable of *completely* characterizing pulses temporally; that is, how many can return the pulse electric field as defined in Eqn. 4.2?

In the frequency domain, the main device is the spectrometer, which does an excellent job of measuring pulse spectra. Unfortunately they cannot tell us the spectral phase. Nor can the spectral phase be retrieved from the spectrum in combination with additional constraints[49, p. 63]. In the time domain there is the intensity autocorrelator which is examined in Section 4.2. In Section 4.3, the FROG is discussed which has proven to be one of the most powerful characterization techniques yet.

The autocorrelation method and FROG method to be described rely on a process of second harmonic generation (SHG). SHG is a nonlinear optical effect and a purely quantum-mechanical process where two photons of the same frequency ω are destroyed while a single photon of double the frequency, 2ω , is simultaneously created.

4.2 Single-Shot Autocorrelator

The single-shot autocorrelator system measures the width of a pulse by transforming its temporal information to measurable spatial information. The first demonstration of this was by Salin et al. [39] which was based on the theoretical framework laid out by Jansky et al. [21]. The idea is to use a 50/50 beamsplitter to produce two identical pulses which are set to cross each other in a nonlinear crystal to produce an image of the crystal at the second-harmonic frequency, as shown in Fig. 4.1. The image can be measured by a simple camera. The spatial image yields the second-order autocorrelation function:

$$A^{(2)}(\tau) = \int_{-\infty}^{\infty} I(t)I(t - \tau)dt \quad (4.4)$$

where τ is the delay. Both of the pulses must be incident on the crystal at a large angle from either side. The SH signal will be produced wherever the pulses coincide spatially and temporally. When both pulses traverse the crystal, certain parts of each pulse will arrive earlier or later than the other; the difference in time between each pulse is the delay. The centre of both pulses arrive at the exact same time, thus corresponding to zero delay. This process is nicely depicted in Fig. 4.2. The SHG signal is cast upon the photodetector; the autocorrelation signal is most intense at the position where the centres of both pulses coincide, then the signal falls off in space. The spatial image can then be converted to temporal information using a calibration technique. The calibration is done by adding a micrometre delay stage to one of the replica beams. As the delay is varied, the SHG image of the crystal will scan across the photodetector. You can then take the known distance Δd that is applied to the delay stage as a ratio of the number of pixels P that the SHG image traverses, $\frac{\Delta d}{P} \left(\frac{\text{mm}}{\text{pixels}} \right)$, then convert the distance to delay using the speed of light c :

$$\frac{\Delta d/c}{P} \text{ delay} \left(\text{units: } \frac{\text{fs}}{\text{pixels}} \right)$$

Since the autocorrelation is in time-space, we need the intensity and phase vs. time to completely characterize the pulse. The problem here is that the intensity cannot be uniquely determined from the autocorrelation Eqn. 4.4 [46]. Thus, an autocorrelation is clearly proportional to, and can provide some measure of, pulse length but there is ambiguity since it cannot uniquely yield the intensity function $I(t)$. In addition, any experimental error that the autocorrelator suffers is difficult to identify since there exists no independent checks to validate the measurement other than the requirement of symmetry [38] along the delay axis and that it does not violate the TBP inequality [46].

The autocorrelator can be quite effective when it is used to *relatively* measure the pulse width as a function of compressor position rather than *absolutely* measure the pulse width. If the autocorrelation becomes narrower when the compressor position of the CPA system is adjusted, one can be quite sure that the pulse width has become shorter with the new compressor position. The optimal compressor position can then be found by simply adjusting it to produce an autocorrelation function as narrow as possible.

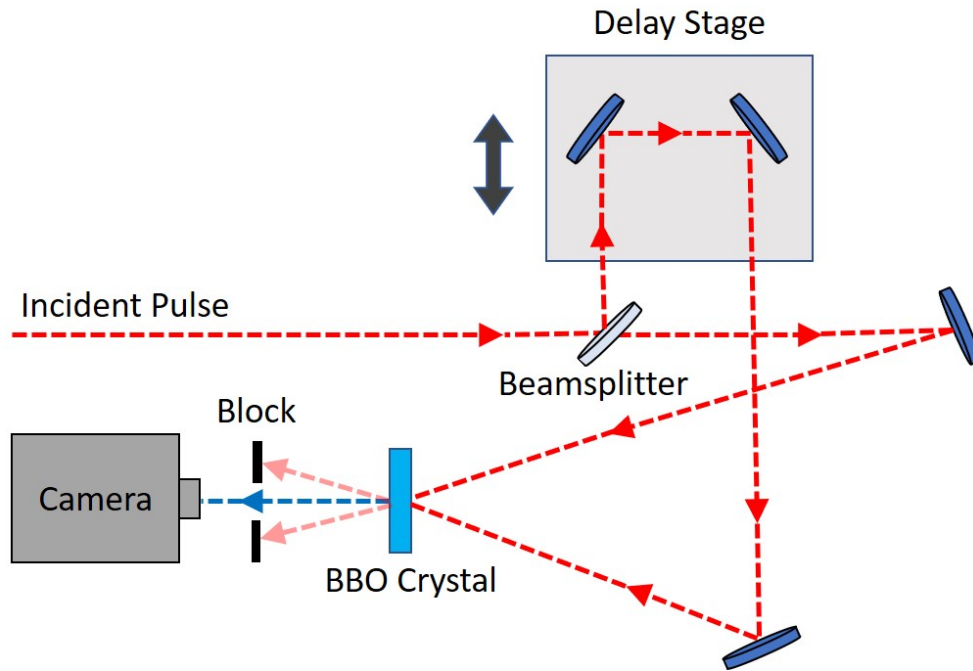


Figure 4.1: Autocorrelator diagram

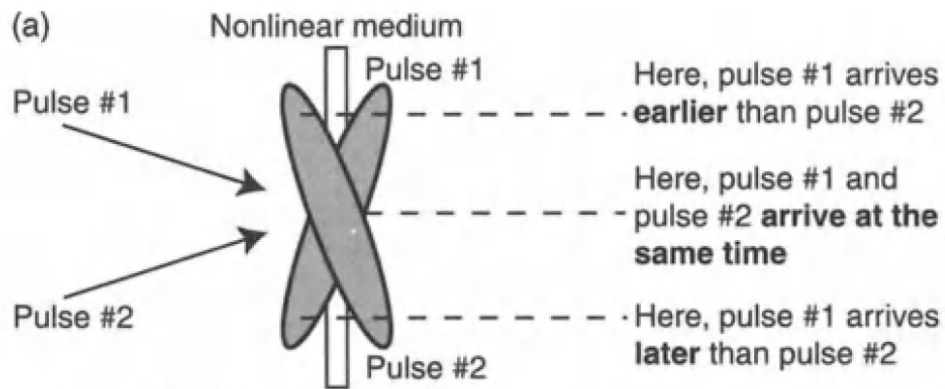


Figure 4.2: Visualization of a single-shot autocorrelation (from [49]).

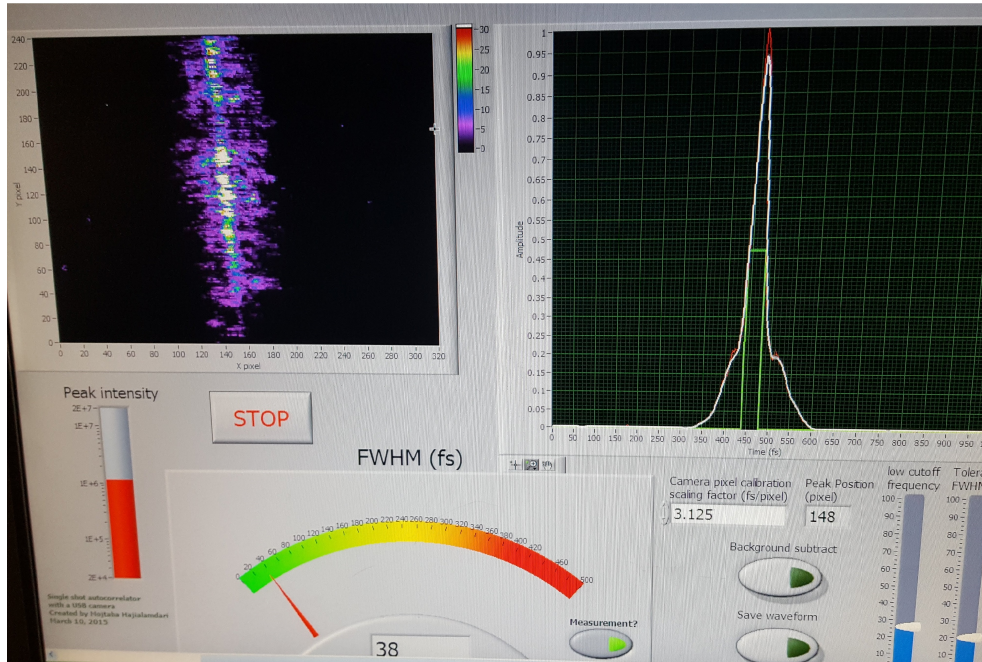


Figure 4.3: Autocorrelation result with the spatial image on the left and the retrieved intensity function $I(t)$ on the right. The temporal FWHM was measured as 38 fs.

4.2.1 Experimental Design and Techniques

The autocorrelator system was in an interferometric setup with a delay stage. The incident pulses are split in equal parts by a 50/50 beamsplitter (diagram shown in Fig. 4.1). The transmitted pulse strikes a mirror and reflects to a Type I BBO crystal. The reflected pulse goes through a delay stage before being reflected towards the BBO crystal. Both pulses are crossed at a large angle in the crystal, a requirement for single-shot autocorrelation. The image of the crystal in the second-harmonic is cast upon a photodetector. The width of the image is shown in pixels which can be counted by any software, in this case, LabView.

4.2.2 Results

The FWHM of the intensity function which was retrieved from the autocorrelation was 38 fs, shown in Fig. 4.3.

The requirement of symmetry along the delay axis is fulfilled and the TBP inequality is not violated, shown below.

The FWHM of the spectrum shown in Fig. 2.6 is 28.8 nm which converts to $\frac{c}{\lambda^2}\lambda = \frac{c}{(800 \times 10^{-9} \text{ m})^2} \times 28.8 \times 10^{-9} \text{ m} = 12.6 \text{ THz}$ and the measured pulse width from Fig. 4.3 is 38 fs, giving us:

$$12.6 \times 10^{12} \text{ Hz} \times 38 \times 10^{-15} \text{ s} = 0.479 > 0.441$$

This was the shortest pulse width that was obtained as the compressor position in the Spitfire Ace was scanned. The retrieved intensity function is not guaranteed to be unique.

4.3 GRENOUILLE: FROG Trace

Frequency-resolved optical gaating was first developed by Kane and Trebino in 1993 [23]. The FROG trace is a three dimensional plot with frequency on the y-axis, delay on the x-axis, and intensity depicted as a heat map. It effectively measures the *spectrogram* of the pulse. It is the pulse's spectrum vs. delay (in comparison to the autocorrelator: signal energy vs. delay) with intensity information on a heat map.

The spectrogram (also called sonograph in some fields) is an age-old plotting technique used in many fields, especially in acoustics such as music, speech recognition, sonar research, and even seismology. Spectrograms display the frequency of a signal as it evolves over time with a heat map to depict intensity. The electric field, $E(t)$, as defined in Eqn. 4.2, can be completely determined from the spectrogram with the exception of a few insignificant ambiguities [49, p. 102].

A spectrogram can be generated by *gating* the frequency spectrum of a signal as time or delay is varied. Music spectrograms use an electronic gate signal which is much shorter in duration than the music signal to generate a spectrogram. As discussed earlier, we know that there is no gate which is shorter than the ultrashort pulse, so we must use the pulse to gate itself; just like the autocorrelator. The FROG trace then is really a spectrally resolved autocorrelation signal. We can refer to the spectrogram of the pulse as a FROG trace. The FROG signal intensity at each point on the heat map is a function of two variables: frequency and delay. A visualization of how a FROG trace is generated is shown in Fig. 4.4. A gate function is scanned across the pulse waveform where the spectrum is computed for each gated portion. The end result is a two-dimensional plot with spectra vs. delay.

The E-field contains all of the information for complete temporal characterization of the pulse. With $E(t)$ we can use Eqn. 4.2 to determine intensity vs. time,

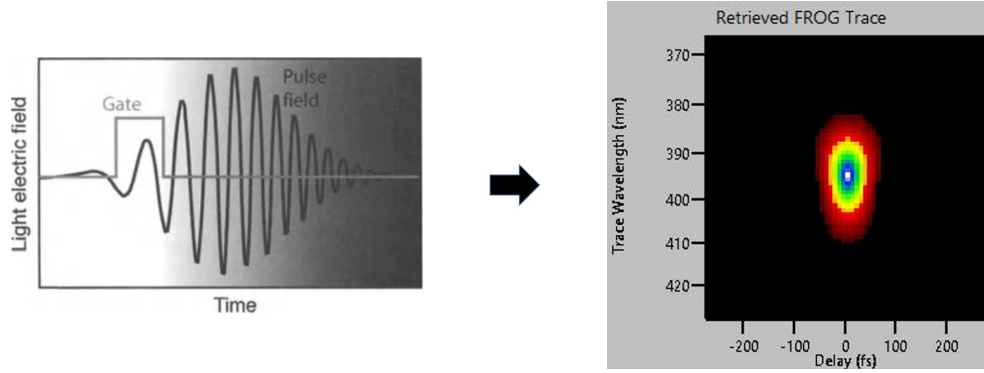


Figure 4.4: A visualization of how a FROG trace is generated. A gate function is scanned across the pulse waveform where the spectrum is computed for each gated portion (the depiction on the left is from [49, p. 102]).

$$I(t) = |E(t)|^2 \quad (4.5)$$

and solve for the phase vs. time:

$$\phi(t) = -\tan^{-1} \left[\frac{\text{Im}(E(t))}{\text{Re}(E(t))} \right] \quad (4.6)$$

From Eqn. 4.3 we know we can express the E-field in frequency space and thus can retrieve the spectrum by,

$$S(\omega) = |\tilde{\mathcal{E}}(\omega)|^2 \quad (4.7)$$

and the spectral phase by,

$$\phi(\omega) = -\tan^{-1} \left[\frac{\text{Im}(\tilde{\mathcal{E}}(\omega))}{\text{Re}(\tilde{\mathcal{E}}(\omega))} \right] \quad (4.8)$$

Since the FROG is a spectrally resolved autocorrelation signal, the experimental setup required to produce a FROG trace will include some type of autocorrelation. Indeed, there are many ways to produce a FROG trace, each of them will use a different type of autocorrelator. The GRENOUILLE (**G**Rating-**E**liminated **N**o-nonsense **O**bservation of

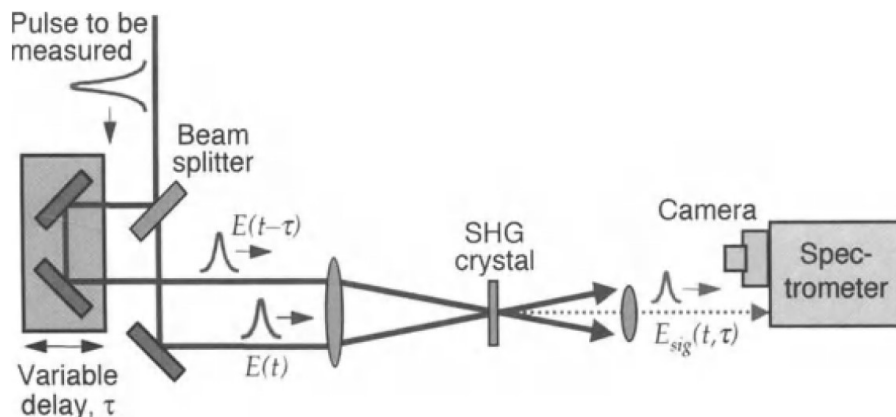


Figure 4.5: Schematic of a non-collinear SHG FROG (from [49, p. 126])

Ultrafast Laser Light **E**-fields, interestingly is also the French word for “frog”) uses an SHG autocorrelator (Figure 4.5) setup which operates single shot.

Typical FROG apparatus consists of an autocorrelator and a spectrometer. The apparatus for an autocorrelator is required, which consists of a beam splitter, delay stage, focusing lens, thin SHG crystal, along with a spectrometer (shown in Fig. 4.5). It requires multiple shots, where a spectrum is recorded at each delay to create a set of spectra plotted against a varied delay - a FROG trace.

The GRENOUILLE seeks to significantly simplify things while retaining all of the capability of a traditional FROG. The GRENOUILLE is touted as one of the simplest pulse characterization devices. The beamsplitter, delay line, and focusing lens is replaced by a single optic: a Fresnel biprism. The thin SHG crystal is unintuitively replaced by a thick SHG crystal which eliminates the need for the spectrometer. This radical simplification does not lead to any loss of capability of a traditional FROG. In fact, the GRENOUILLE is one of the more sensitive devices since the SHG signal scales with crystal thickness. The general layout of elements which comprise a GRENOUILLE can be seen in Fig. 4.6

The Fresnel biprism is convenient in that it splits an incident collimated beam into two beamlets and sets the transmitted beamlets on beam paths that are angled towards each other such that they are destined to cross at some point in space as can be seen in Fig. 4.8. The SHG crystal can be set such that the beams cross within the crystal. As described in Section 4.2, when two pulses cross at a large angle in a crystal, a single shot SHG autocorrelation signal is produced. In this way, the beamsplitter and delay stage are no longer needed since the biprism splits the beam into two beamlets and the delay is provided

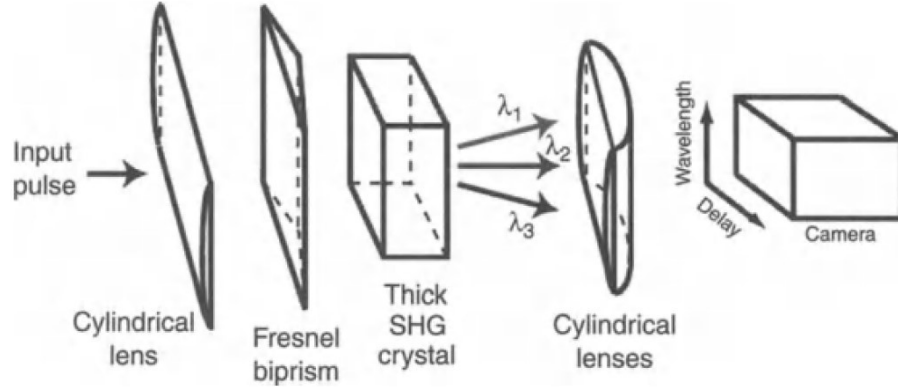


Figure 4.6: Optical layout of GRENOUILLE apparatus (from [49, p. 231])

by the large angle crossing of the pulses. The beam combining optic (the focusing lens) is not required either since the two beamlets are set to cross after transmitting through the biprism.

The thick SHG crystal has two useful properties, it can act as a nonlinear spectrometer [2, 4] and it produces stronger SH signals than thinner crystals [33]. Thus, the thick SHG crystal will simultaneously produce a single shot autocorrelation and disperse the spectrum with reasonable resolution compared to conventional spectrometers [4]. The resulting signal can be cast upon a photodetector to produce an image of frequency on one axis vs. the single shot SHG autocorrelation signal on the other axis; all with intensity information measured by the photodetector the same way it measures any autocorrelation signal. Thus it produces a spectrogram equivalent to an SHG FROG trace but with higher sensitivity.

Dithering Crystal

The downfall of the especially thick crystal is that it has a narrow bandwidth. Thin crystals have wider bandwidths since the nonlinear-optical phase-matching bandwidth is inversely proportional to the crystal thickness [32].

An extremely short pulse (i.e., sub-15 fs), must, courtesy of the Time-Bandwidth relationship Eqn. 3.2, have a very wide bandwidth. The bandwidth may be much wider than the narrow bandwidth offered by the thick SHG crystal. Thus the thick SHG crystal may only measure a small portion of a wide spectral bandwidth pulse. The incidence angle of

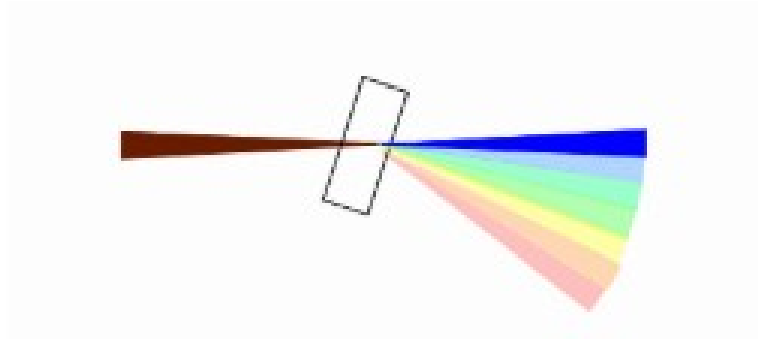


Figure 4.7: Visualization of angle dithering the SHG crystal. Reprinted with permission from [32].

the pulse upon the crystal corresponds to a certain range of wavelengths that are phase-matched in the crystal [32]. Using this idea, the SHG crystal can be set atop a motor which rotates the crystal to change the angle of incidence (visualized in Fig. 4.7). At each incidence angle, a measurement can be taken until the entire bandwidth is accounted for, resulting in a single complete FROG trace. Thus, the FROG trace would be a multi-shot measurement. This is known as *angle-dithering*, first suggested by Nack et al. [30] and then demonstrated by O’Shea et al. in [32]. This process then enables a thick SHG crystal to have comparable bandwidths of thinner crystals while harnessing the sensitivity of thick crystals.

4.3.1 Experimental Design and Techniques

We used a GRENOUILLE 8-9-122-THICK-USB model from Swamp Optics (a Rick Trebino company) with a centre-wavelength range of 700 - 1100 nm, spectral range @ 800 nm of 300 nm, and pulse-length range @ 800 nm of 10 - 100 fs. The GRENOUILLE was on loan to us from Dr. Kevin Resch at the Institute for Quantum Computing (IQC). Since it is a commercial device, there is limited information on the elements that comprise the device. So a typical GRENOUILLE setup will be described.

Two beam steering mirrors are required to properly align the pulses into the GRENOUILLE, to allow 4 degrees of freedom of the beam. The pulses first go through a cylindrical lens which applies a horizontal line focus onto the Fresnel biprism. The biprism splits the beam into two beamlets and crosses them on a thick SHG crystal. The crystal sits atop a motor which dithers it in angle. Each incident pulse on the crystal produces a single-shot SHG autocorrelation which comprises only a portion of the pulse bandwidth. The range

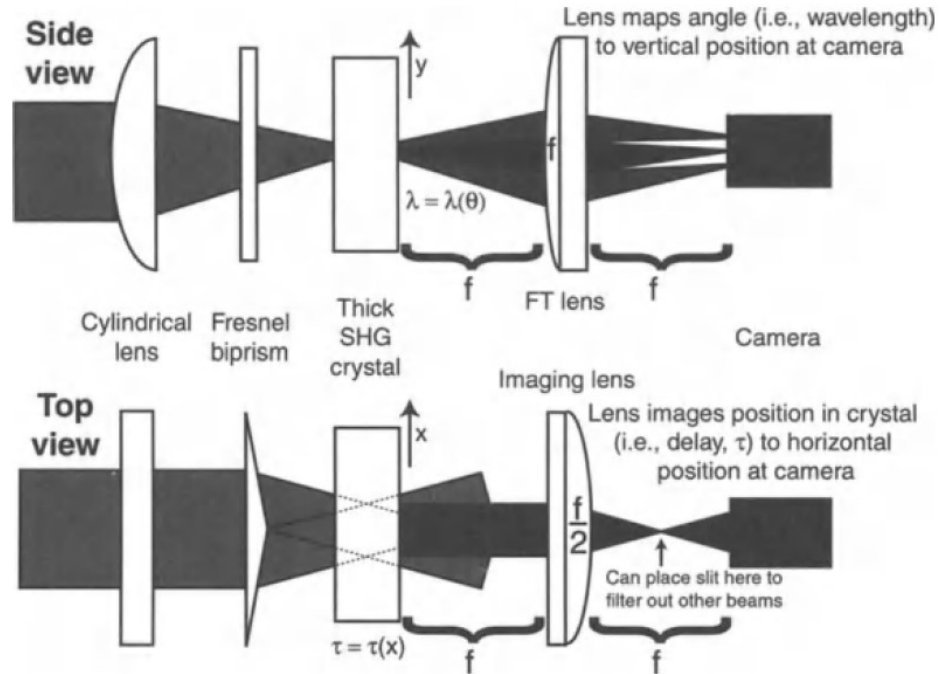


Figure 4.8: The side-view and top-view of the GRENOUILLE beam geometry (from [49, p. 231])

of wavelengths that is covered in the spectrally resolved single-shot SHG autocorrelation is dependent on the pulse incident angle on the crystal. So for a complete FROG trace, each pulse must be incident on the dithering crystal at a sufficient number of angles to cover the entire bandwidth of the pulse. The motor which controls the dithering of the crystal is controlled by an electronic driver with phase control: tuning the frequency of the dithers to phase-match with the repetition rate of the laser, and amplitude control: tuning the range of incidence angles of the pulses on the crystal (i.e., tuning how much the crystal is able to rotate on each dithering rotation). A cylindrical lens is set after the crystal to map the spectrally resolved SHG autocorrelation signal, with frequency on the vertical axis and delay on the horizontal axis, onto a camera. The side-view and top-view of the beam geometries are shown in Fig. 4.8.

4.3.2 Results

Since the GRENOUILLE was a commercial device and not a tabletop setup with its elements readily accessible, physical diagnostics could not be carried out to ensure each component was working as designed. Instead, an analytical approach was taken to analyse the validity of the final FROG traces. Fortunately, FROG devices offer robust independent checking opportunities that are not available for other pulse measurement schemes.

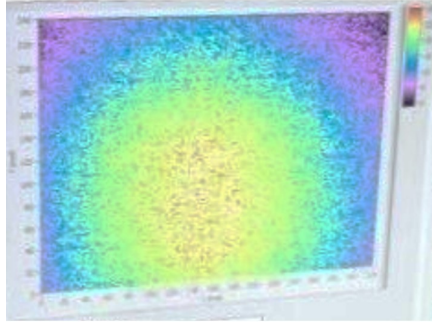
The GRENOUILLE was used to characterize pulses from two devices: the Spitfire Ace CPA system and the hollowfibre compressor. The most rigorous analytical validation method is the *autoconvolution* test which compares the autoconvolution of the pulse's independently measured spectrum with the *frequency marginal* of the FROG trace. Before arriving at the autoconvolution test, there are more qualitative cues along the way to assess the validity of the measurement. Visual inspection of the span of the trace in the frequency and delay axes are an easy way to determine if the FROG has captured the entirety of the pulse [8]. A FROG trace offers various sets of information, and though a FROG trace may prove to be unreliable by the autoconvolution test, its information can still hold merit in certain aspects. The internal optics of the GRENOUILLE were inaccessible and thus any errors produced in the measurements must be either because of human error (incorrect operation of the device) or faultiness of the GRENOUILLE itself. The points of discussion are focused on scrutinization of the FROG traces.

The pulses from the Spitfire Ace were a good place to start since they are shaped by a commercial device designed for stability and their characteristics are quite simple. The spectrum of the pulses is shown in Fig. 2.6. The FWHM and centroid were measured to be 32.8 nm and 798.8 nm, respectively. The spectrum measured by the USB4000 spectrometer will be referred to as the *actual* spectrum. The assumption was that the USB4000 was working correctly since it was calibrated by a mercury lamp and matched the spectra produced by a separate spectrometer.

Once the pulses are detected by the GRENOUILLE, we follow a step-by-step process to produce an accurate measurement. The first step is to ensure that the beam is spatially centred on the GRENOUILLE's spatial camera. The beam profile should be circular and the intensity should drop off as a gaussian from the centre. The detected beam profile seemed to match the manufacturer specifications and that of an independent beam profiler, so we were confident moving onto the next step. The beam profile comparison is shown in Fig. 4.9 and a photo of the independent beam profiler setup is shown in Fig. 4.10.

Since the spatial properties seem to be in order, the temporal and spectral features are next in focus. Due to the nature of SHG FROG, the traces must be symmetrical along

Independent Beam Profile



Beam Profile from GRENOUILLE

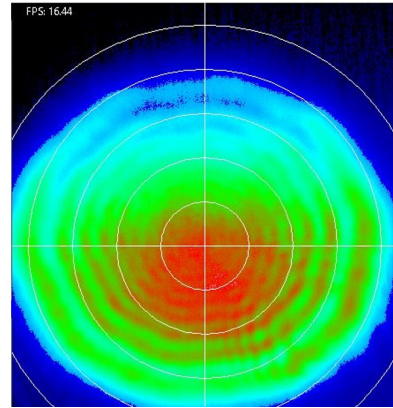
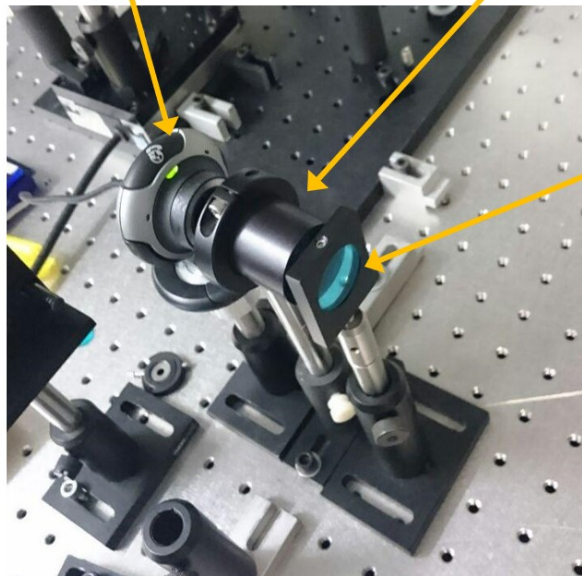


Figure 4.9: Comparison of the independently measured beam profile (left) and the beam profile measured by the GRENOUILLE (right).

Microsoft LifeCam VX-3000

Telescopic lens



Filter

Figure 4.10: Independent beam profiler setup.

the delay axis [8]. The beam steering mirrors must be slightly adjusted until symmetry is achieved. It was found extremely difficult to achieve a symmetric trace, which is an early indication of a physical error in the system.

All FROG traces that are discussed here are the retrieved traces rather than the experimental (measured) traces. This is due to the fact that the retrieved FROG traces are generally more accurate than the experimental traces [13]. If two FROG measurements are taken which produce: 1. a noisy FROG trace that still allows the FROG algorithm to converge (i.e, a trace which is not so noisy that the FROG algorithm cannot cope), and 2. a noise-free FROG trace that the FROG algorithm easily converges. When the FROG algorithm converges, it yields a retrieved pulse, that is an intensity and phase is returned. The result is that the retrieved pulse from the noisy experimental FROG trace produces a retrieved FROG trace which better approximates the noise-free experimental FROG trace [13]. Essentially, the retrieved FROG trace from a *bad* measurement better approximates an experimental FROG trace from a *good* measurement. This impressive result stems from the *overdetermination* of the FROG. From an informational standpoint, to retrieve a pulse, one needs N data points from the intensity $I(t)$ plus N points from the phase, so $2N$ data points. The FROG is an image of N^2 data points (or pixels) resulting in a redundancy in data.

We can analyze the FROG trace shown in Fig. 4.11. First off, there is too much signal on the right-hand side causing an asymmetry. This alone would indicate a false FROG measurement since asymmetry violates the laws of physics for SHG FROG. Also, we have prior assumptions of the pulse shape, such that its functions $I(t)$ and $S(\omega)$ should be gaussian as stated by the manufacturer specifications and supported by the autocorrelation and spectrometer measurements. Intuitively then, the FROG trace seems to exhibit a bit too much complexity to represent a gaussian pulse. Furthermore, by inspection, the trace does not seem to span the actual entire spectral bandwidth of the pulses. The wavelength values on the axis correspond to the frequency doubled wavelengths, thus we can double the wavelengths to see the original wavelengths. We can see that it ranges from $390 \text{ nm} \times 2 = 780 \text{ nm}$ to $410 \text{ nm} \times 2 = 820 \text{ nm}$, which is considerably less than the range seen in Fig. 2.6. These observations are sufficient without further analysis to conclude that the measurement is inaccurate.

We can be confident that the spatial alignment from our side is good due to the image on the spatial camera. The pulse is perhaps experiencing dispersion and has become distorted, so the compressor in the Spitfire Ace can be adjusted to compensate for any GVD. As the compressor was scanned, the FROG trace looked increasingly less complex while measuring to be shorter in pulse duration. One can also tweak the background subtraction settings to get rid of as much noise as possible while retaining pulse information. We need not

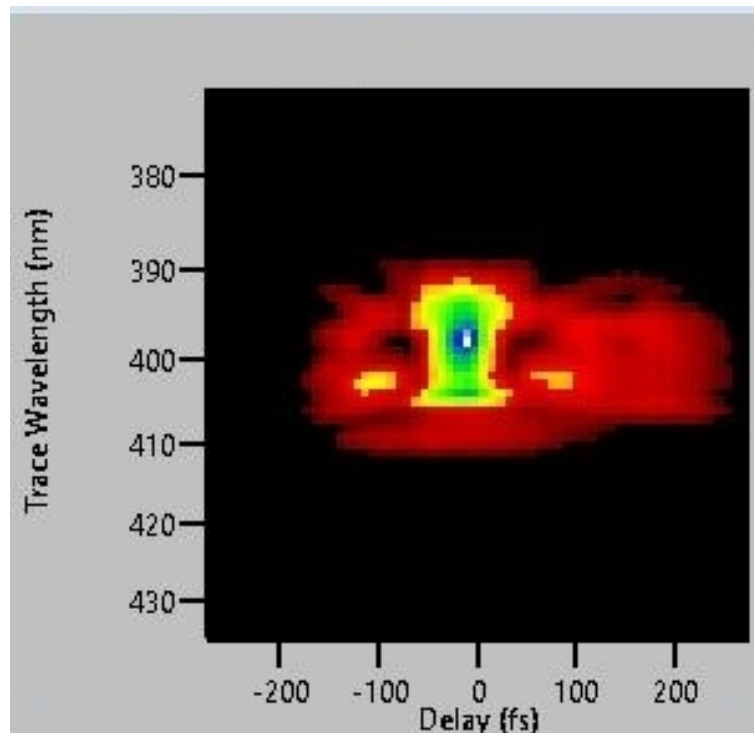


Figure 4.11: Retrieved FROG measurement of pulses from the Spitfire Ace with a notable asymmetry on the right-hand side.

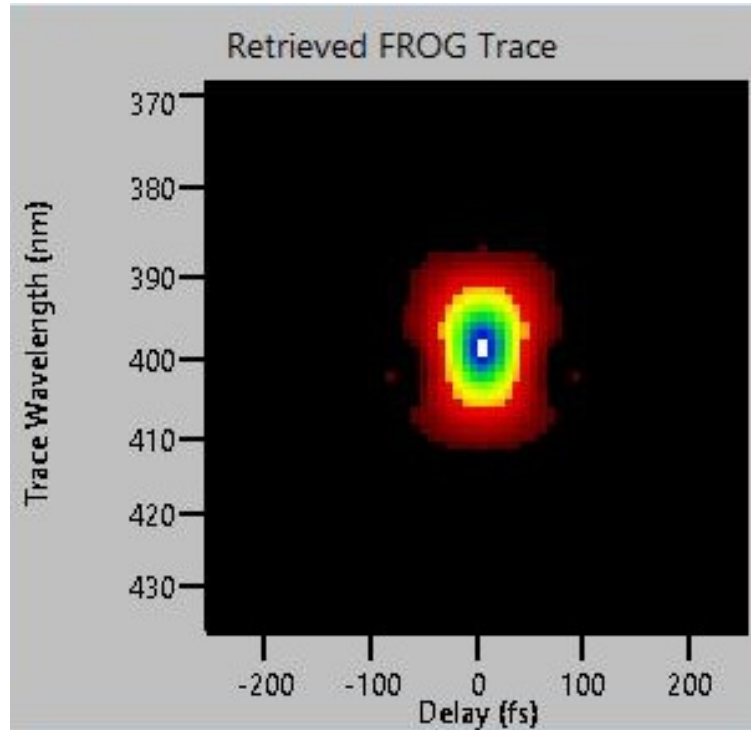


Figure 4.12: Retrieved FROG measurement of pulses from the Spitfire Ace. Both axes exhibit Gaussian forms.

worry about tweaking the background subtraction settings to produce a fake measurement because, ultimately, the trace will be subject to the rigorous autoconvolution test. After scanning the compressor and applying a manual background subtraction, the FROG trace shown in Fig. 4.12 was produced. The trace looks symmetrical along the delay axis for starters. Better yet, it looks decently gaussian along both axes. The bandwidth however still seems narrower than the actual bandwidth. Let us take a deeper look by extracting the spectral intensity $S(\omega)$ and spectral phase $\phi(\omega)$ as a function of wavelength, shown in Fig. 4.13. Indeed, the observed FWHM bandwidth of 26.8 nm does not match the actual spectral bandwidth of the pulse (Fig. 2.6). This is significant evidence that the measured FROG trace is unreliable. But for reassurance, let us apply the most robust test that is available for the FROG: the autoconvolution of the actual spectrum versus the frequency marginal of the FROG trace. It states that the frequency marginal of the SHG FROG trace must be equal to the autoconvolution of the independently measured spectrum [8].

The frequency marginal is the integration of a FROG trace over the delay variable:

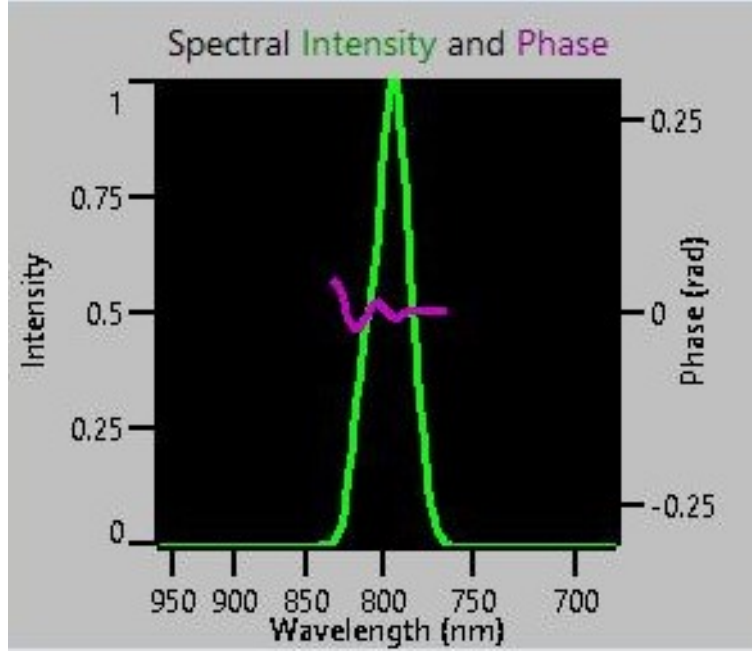


Figure 4.13: Retrieved spectrum and phase from the FROG measurement of Fig. 4.12

$$F_{\omega}(\omega) = \int_{-\infty}^{\infty} I_{FROG}(\omega, \tau) d\tau \quad (4.9)$$

where I_{FROG} is the FROG signal value at a given frequency ω and delay τ .

The frequency marginal of the SHG FROG trace, $F_{\omega}^{SHG}(\omega)$ must be equal to the auto-convolution of the spectrum:

$$F_{\omega}^{SHG}(\omega - 2\omega_0) = S(\omega - \omega_0) * S(\omega - \omega_0) \quad (4.10)$$

where S is the independently measured spectrum, ω_0 is the carrier frequency, and the asterisk means convolution (S is convolved with itself). The frequency shifts of $2\omega_0$ and ω_0 simply centres both functions at zero, however any arbitrary frequency shift can be chosen so long as the frequency shift is doubled for the frequency marginal of the SHG FROG trace.

Detailed discussions regarding this relationship can be found in [1, 3, 8]. It is born out of the field of analytical signal processing which is beyond the work presented here.

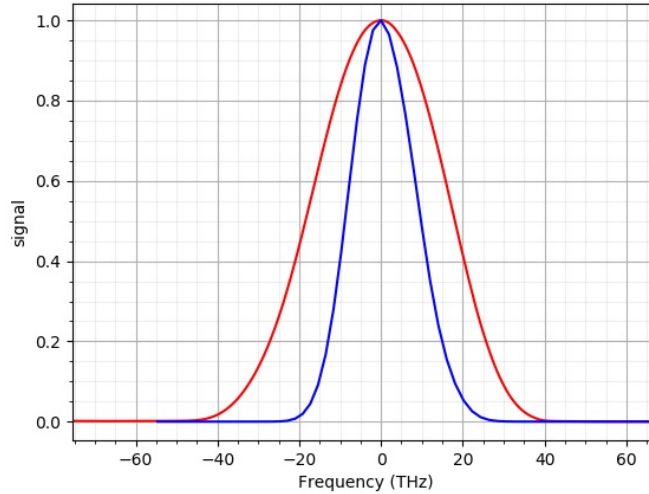


Figure 4.14: Autoconvolution test: Comparison of the autoconvolution (red line) of the independently measured Spitfire Ace spectrum (blue line) from Fig. 2.6 with the frequency marginal of the FROG trace of Fig. 4.12. The autoconvolution is observed to have a considerably larger full range causing the autoconvolution test to fail.

The relationship will be taken as a fact. Many works based on FROG characterization incorporate the autoconvolution in their analytical methods, including its use to even correct FROG traces as done by Taft et al. in [46].

Now we have a powerful validation technique that compares two independent measurements. If Eqn. 4.10 is not satisfied, there must be an error present in the system [49, p. 205]. We apply the autoconvolution to the spectrum from Fig. 2.6 and compare to the frequency marginal of the FROG trace from Fig. 4.12, shown in Fig. 4.14. It is clearly observed that the autoconvolution full range (red line) is much wider than that of the frequency marginal (blue line), indicating that, a. Eqn. 4.10 is not satisfied, and b. the spectral range of the FROG trace is insufficient, which agrees with the previous observation. Important to note was that the FROG trace obtained in Fig. 4.12 was the best one measured. Failure of the autoconvolution test must certainly mean that there is an error somewhere in the system.

What is interesting is that retrieved intensity function shown in Fig. 4.15 from the FROG trace in Fig. 4.12 has an FWHM of 37.6 fs which is not far off from the 38 fs FWHM of the retrieved intensity function from the autocorrelation in Fig. 4.3. Since the

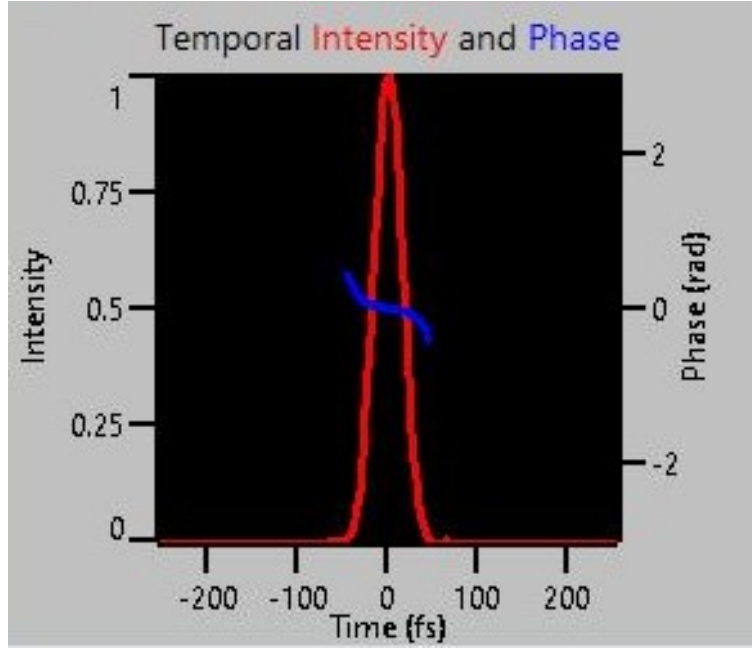


Figure 4.15: Retrieved intensity and phase from the FROG measurement of Fig. 4.12.

autoconvolution test failed, we must treat the FROG measurement as unreliable. However, let us check to see if the FROG algorithm has returned a physically unrealizable pulse. We can check to see if the TBP in Eqn. 3.1 still holds. The FWHM of the spectrum shown in Fig. 4.13 is 28.8 nm which converts to $\frac{c}{\lambda^2} \lambda = \frac{c}{(800 \times 10^{-9} \text{ m})^2} \times 28.8 \times 10^{-9} \text{ m} = 12.6 \text{ THz}$ and the measured pulse width from Fig. is 37.6 fs, giving us:

$$12.6 \times 10^{12} \text{ Hz} \times 37.6 \times 10^{-15} \text{ s} = 0.474 > 0.441$$

Thus, the FROG algorithm still returned a physically realizable pulse since it did not violate the TBP inequality in Eqn. 3.1. It is impossible to tell if the agreement of the pulse width measurement of the FROG with the autocorrelation is mere coincidence or a true representation of reality.

The end goal of the work in this thesis is to generate and characterize few-cycle pulses. The hollowfibre compressor system has been employed to generate these pulses, so let us task the GRENOUILLE to characterize them. Fig. 4.16 shows the spectrum of pulses which were output from the hollowfibre compressor. The spectrum was taken just before

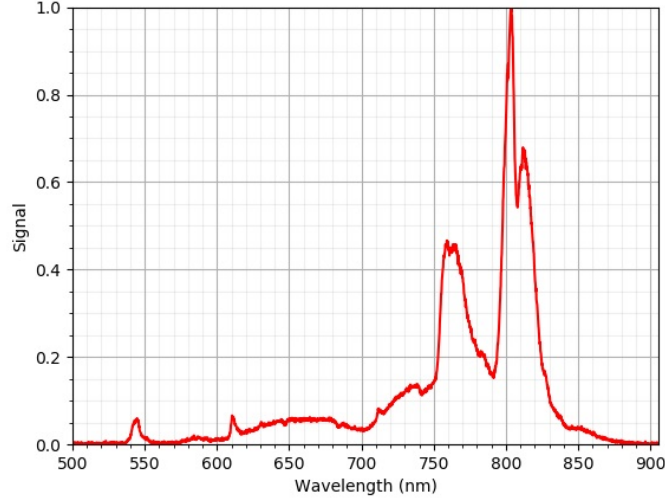


Figure 4.16: Independently measured spectrum of hollowfibre compressed pulses.

it entered the GRENOUILLE to best compare to the FROG output. The corresponding FROG trace is displayed in Fig. 4.17, which exhibits complexity as would be expected for such a frequency modulated pulse [8]. The retrieved spectrum and phase from the FROG measurement can be seen in Fig. 4.18. The accuracy of the measurement can first be evaluated by comparing the independently measured spectrum (Fig. 4.16) with the retrieved spectrum from the FROG trace (Fig. 4.18). This comparison can be seen in Fig. 4.19. As shown, both spectra exhibit very similar spectral peaks and features. However, the spectral range of the spectrometer measurement again is much wider than that of the FROG spectrum retrieval. To examine further, the autoconvolution test is applied and shown in Fig. 4.20. The difference in spectral range is clearly evident where the autoconvolution of the actual spectrum is much wider than the FROG frequency marginal. It is quite apparent that there is a bandwidth problem with the GRENOUILLE. The device manufacturers indeed confirmed upon inspection that the GRENOUILLE was suffering from insufficient bandwidth due to internal misalignment.

Both spectra shown in Fig. 4.19 and the autoconvolution test in Fig. 4.20 show agreements in spectral features. In the autoconvolution test, the frequency marginal clearly exhibits the same two large peaks and a small shoulder on the left as the autoconvolution. This indicates an amount of accuracy in the FROG data even though the autoconvolution test failed.

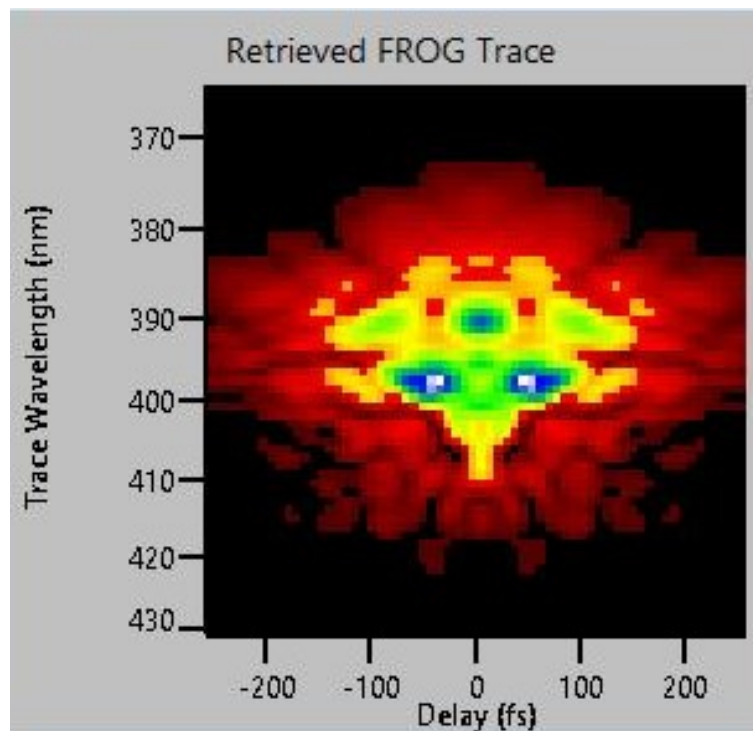


Figure 4.17: Retrieved FROG measurement of the same hollowfibre compressed pulses which correspond with Fig. 4.16

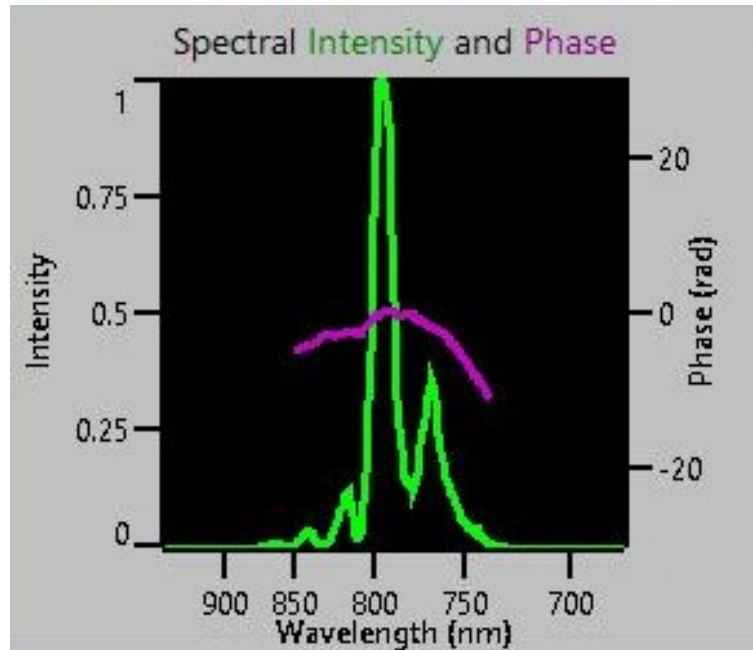


Figure 4.18: Returned spectrum and phase from the FROG measurement of Fig. 4.17.

The phase of the pulse is a very important gauge on the amount of compression that has been applied. With the measurement of the Spitfire Ace, the width of the trace in the delay axis scales with the position of the Spitfire Ace's compressor. Even if the FROG trace is not measuring the pulse width accurately in absolute terms, it can still provide some measure relative to the Spitfire Ace compressor position (i.e., it can measure changes). The same can be done in the hollowfibre compression setup with the two silica wedges which can apply an amount of positive GVD to compensate for too much negative GVD from the chirped mirrors. By scanning the wedges, the amount of pulse chirp should either increase or decrease, depending on the GVD compensation. It is seen in Fig. 4.21 that the spectral phase of the pulse has a rather complex form when the silica wedges were at a certain position. As the silica wedges were scanned to reduce the amount of material that the pulses experienced, thereby reducing the amount of added positive GVD, the phase approached the quadratic form shown in Fig. 4.16. A quadratic phase indicates a linearly chirped pulse which is much easier to deal with than a 3rd order or higher phase function [14]. The linear chirp can be corrected by simply fine-tuning the silica wedges to minimize the total GVD as discussed in Chapter 3. Third order phase compensation requires a much more complicated optical setup such as the one in [14]. Due to severe difficulty in obtaining a FROG trace with the faulty GRENOUILLE device, further exploration of

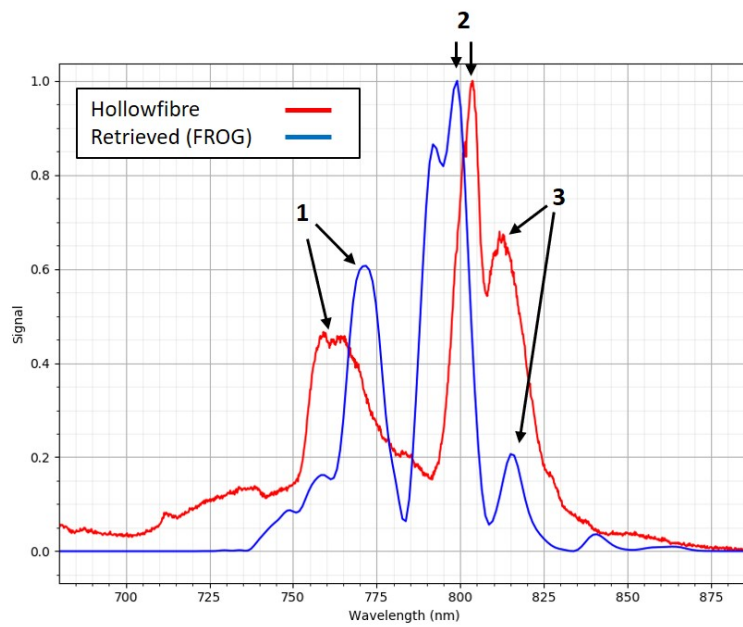


Figure 4.19: Comparison of the hollowfibre spectra measured by the USB4000 (red) and returned from the GRENOUILLE (blue). The arrows indicate spectral peaks which are similar for both spectra.

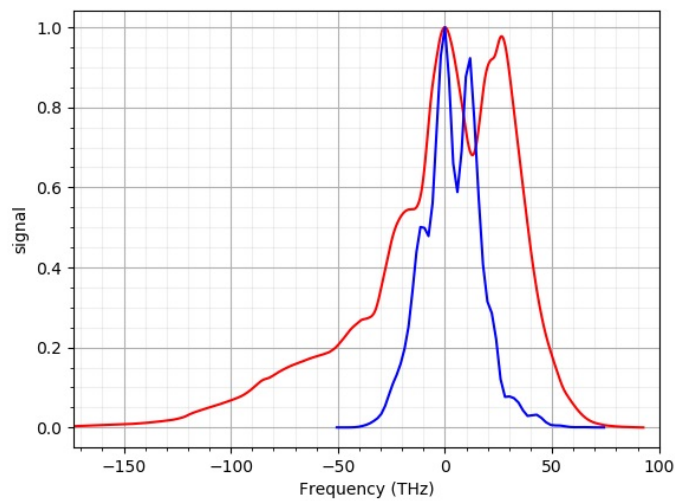


Figure 4.20: Autoconvolution test: Comparison of the autoconvolution (red line) of the independently measured hollowfibre spectrum (blue line) from Fig. 4.16 with the frequency marginal of the FROG trace of Fig. 4.17. The autoconvolution is observed to have a considerably larger full range causing the autoconvolution test to fail. However, both curves exhibit similar spectral features. Both are double-peaked with a small shoulder on the left peaks.

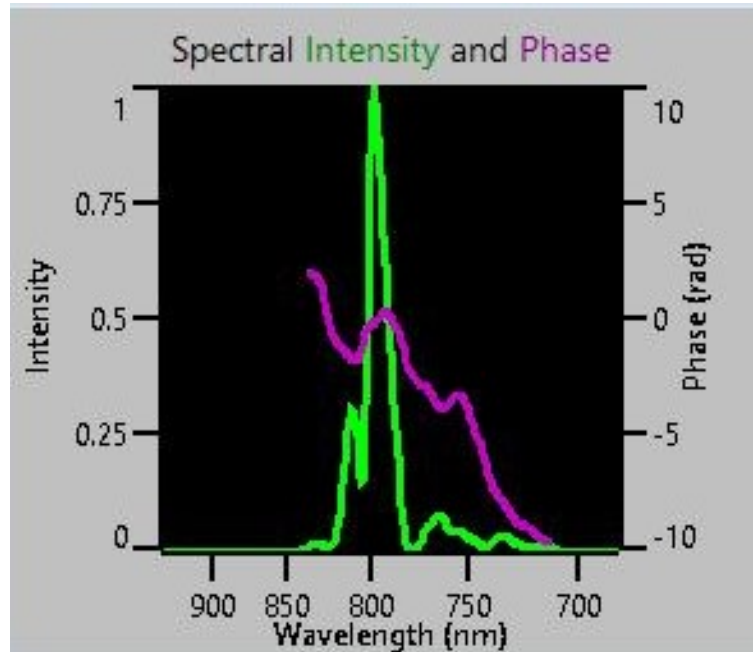


Figure 4.21: Retrieved spectrum and phase from a FROG measurement of hollowfibre compressed pulses. The phase exhibits a complex form as opposed to the phase function in Fig. 4.18.

phase functions was left incomplete.

The temporal shape and phase of the pulse is shown in Fig. 4.22. The quadratic phase is also observed. However, unlike the spectrum, there was no independent measure of the pulse temporal shape (i.e., $I(t)$), hence there is no real way to tell if the temporal shape has any sort of accuracy other than if it passed the autoconvolution test. The autocorrelator from Section 4.2 is not capable of producing a measurement of the hollowfibre pulses since it lacks sufficient bandwidth (i.e., the crystal is too thick). The retrieved temporal shape cannot be reasonably trusted.

A step-wise methodology of assessing FROG traces has been demonstrated by first using qualitative methods, then turning to the quantitative autoconvolution method. Though the autoconvolution test failed in all cases, the FROG data seemed to exhibit a certain amount of accuracy in some of its data, in particular it provided useful relative measurements of phase as values of GVD were varied. The validation methods indicated that the FROG traces were suffering from systematic measurement errors. The errors were confirmed to be those of faultiness in the GRENOUILLE device as indicated by the device manufacturers

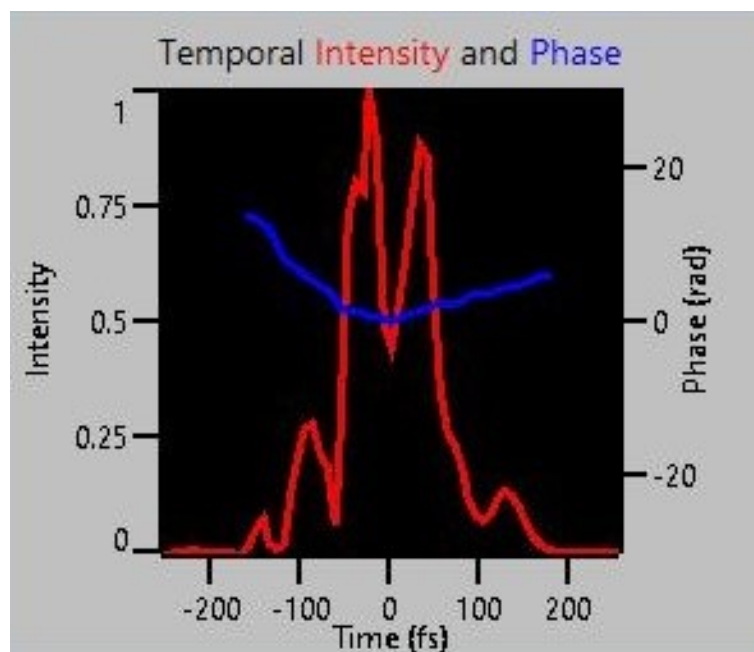


Figure 4.22: Returned intensity and phase from the FROG measurement of hollowfibre compressed pulses of Fig. 4.17.

upon inspection. If a FROG trace passes all the methods of analysis from above within a level of agreement, one can be confident that the FROG trace is reliable in its all of its information.

Chapter 5

Conclusion and Future Work

This thesis reports on improvement and progression of three different aspects of a CEI experiment: the TOF spectrometer, the hollowfibre compressor, and the GRENOUILLE pulse characterization device.

The TOF spectrometer was modified to correct asymmetries in its geometry. The modification was shown to improve the homogeneity of the ion extraction field by analysis of the TOF histograms. The new TOF histogram showed a 77% narrowing in FWHM of the CO_2^+ peak. The CO_2^+ time of flight decreased by 60%, indicating a 513% increase in the average strength of the electric field.

Pressure, Spitfire Ace compressor position, and transmission mode, were varied to reveal how they were correlated with the output spectra of the hollowfibre compressor. The output spectra were compared against a published ideal spectrum of that same hollow core silica fibre model. A study of pressure and Spitfire Ace compressor position was carried out to determine their optimal settings for reproducing the reference spectrum. It was found that the bandwidth at full base and the number of modulations increased with pressure. The optimal pressure was found to be 379 Torr. The compressor position in the Spitfire Ace was strongly correlated with the spectral profile of the output. The optimal Spitfire Ace compressor position range was 8000 to 8200. The fundamental mode was found to be the best transmission mode.

The FROG traces from the GRENOUILLE device were subject to analysis through both qualitative and quantitative means. A methodology was presented to assess the validity of FROG measurements. The FROG traces were found to be invalid in all cases but still held some merit in subsets of its information. It was found particularly useful in measuring changes to pulses. There were signs of some accuracy in the agreement of spectral profiles

between the independent and FROG retrieved spectra. The autoconvolution was the final test of validity for the FROG traces and failed in all cases. The consistent problem was the insufficient bandwidth as indicated by the autoconvolution test and the comparison of independent and retrieved spectra. The device manufacturers eventually confirmed this finding upon inspection of the device.

The work on these three subjects may provide a stepping stone for future experimental work in CEI.

Future Work

The hollowfibre chamber can be improved by replacing the current plastic chamber with a metal one (aluminium is the standard choice) for superior vacuum performance and stability. Viewports can be added for observation of both tips of the hollowfibre to assist with alignment. The new chamber can have three gas-line connections for: pressurization (input gas), evacuation (vacuum connection), and pressure measurement (pressure gauge). This will replace the current setup which only uses a single connection to do all three of these tasks. The pressurization and evacuation ports can be on either sides of the chamber to provide an inlet and outlet. The gas-lines should be flexible tubing which is fastened to the optical table. The flexibility will allow the chamber to be movable during alignment without resistance from stiff copper tubing. The fastening to the optical bench will prevent disturbance to the hollowfibre chamber when valves are being adjusted on the gas-lines.

Once the GRENOUILLE is confirmed to be functioning correctly and producing reliable measurements, its full power can be harnessed to help maximize the hollowfibre compression. Measurements can be taken at 3 different points of the system: prior to entry of the hollowfibre, directly at the exit of the hollowfibre, and after the sequence of chirped mirrors. Knowledge of the pulse width and phase prior to entry and directly at exit of the hollowfibre will help understand the correlation between the Spitfire Ace compressor position and the output spectral shape. Perhaps a negative GVD prior to entry is preferable to pre-compensate for the positive GVD that the pulse acquires during the pulse's propagation in the hollowfibre. Characterization at exit of the hollowfibre will certainly indicate the compression that will be required to achieve a bandwidth-limited pulse. The hope will be that the pulse is linearly chirped (quadratic phase) with positive GVD at the exit, allowing the chirped mirrors to easily compensate with negative GVD and fine-tuning with the positive GVD of the silica wedges. If the pulses have a cubic phase distortion, a more complicated compressor setup consisting of a combination of gratings and prisms in a certain geometry will be required, as in [14], or the hollowfibre parameters should be adjusted to produce a simple linear chirp.

For future experiments, a kinematic mirror can be set just before entering the CEI chamber to intercept the beam and send it to the GRENOUILLE. This will provide the most accurate characterization of the pulses that will be interrogating the molecules. The GVD can be set to pre-compensate for the silica window of the chamber to ensure the shortest possible pulses in the chamber.

Finally, a pump-probe experiment can be done with few-cycle pulses to investigate the bending and stretching processes observed by Wales et al. in [\[52\]](#).

References

- [1] Martin H Ackroyd. Short-time spectra and time-frequency energy distributions. *The Journal of the Acoustical Society of America*, 50(5A):1229–1231, 1971.
- [2] AG Akmanov, AI Kovrigin, and PODSOTSK. NK. Frequency discrimination in laser radiation, 1969.
- [3] Richard A Altes. Detection, estimation, and classification with spectrograms. *The Journal of the Acoustical Society of America*, 67(4):1232–1246, 1980.
- [4] DH Auston. Nonlinear spectroscopy of picosecond pulses. *Optics Communications*, 3(4):272–276, 1971.
- [5] Irina Bocharova, Reza Karimi, Emmanuel F Penka, Jean-Paul Brichta, Philippe Lassonde, Xiquan Fu, Jean-Claude Kieffer, André D Bandrauk, Igor Litvinyuk, Joseph Sanderson, et al. Charge resonance enhanced ionization of co 2 probed by laser coulomb explosion imaging. *Physical review letters*, 107(6):063201, 2011.
- [6] Robert W Boyd. *Nonlinear optics*. Elsevier, 2003.
- [7] Robert J Cotter. Time-of-flight mass spectrometry: An increasing role in the life sciences. *Biomedical & environmental mass spectrometry*, 18(8):513–532, 1989.
- [8] Kenneth W DeLong, Rick Trebino, and Daniel J Kane. Comparison of ultrashort-pulse frequency-resolved-optical-gating traces for three common beam geometries. *JOSA B*, 11(9):1595–1608, 1994.
- [9] Meirong Dong, Jidong Lu, Shunchun Yao, Jun Li, Junyan Li, Ziming Zhong, and Weiye Lu. Application of libs for direct determination of volatile matter content in coal. *Journal of Analytical Atomic Spectrometry*, 26(11):2183–2188, 2011.

- [10] AAA El-Zein, P McKenna, WA Bryan, IMG Johnston, TRJ Goodworth, JH Sanderson, ID Williams, WR Newell, PF Taday, EJ Divall, et al. A detailed study of multiply charged ion production within a high intensity laser focus. *Physica Scripta*, 2001(T92):119, 2001.
- [11] FEMTOLASERS, FEMTQLASERS Produktions GmbH. *Users manual for Ultra Broadband Dispersive Mirror Compressor*, 2005.
- [12] Bernold Feuerstein and Uwe Thumm. Mapping of coherent and decohering nuclear wave-packet dynamics in d 2+ with ultrashort laser pulses. *Physical Review A*, 67(6):063408, 2003.
- [13] David N Fittinghoff, Kenneth W DeLong, Rick Trebino, and Celso L Ladera. Noise sensitivity in frequency-resolved optical-gating measurements of ultrashort pulses. *JOSA B*, 12(10):1955–1967, 1995.
- [14] Richard L Fork, CH Brito Cruz, PC Becker, and Charles V Shank. Compression of optical pulses to six femtoseconds by using cubic phase compensation. *Optics letters*, 12(7):483–485, 1987.
- [15] M Gaft, E Dvir, H Modiano, and U Schone. Laser induced breakdown spectroscopy machine for online ash analyses in coal. *Spectrochimica Acta Part B: Atomic Spectroscopy*, 63(10):1177–1182, 2008.
- [16] LB Guo, ZQ Hao, M Shen, W Xiong, XN He, ZQ Xie, M Gao, XY Li, XY Zeng, and YF Lu. Accuracy improvement of quantitative analysis by spatial confinement in laser-induced breakdown spectroscopy. *Optics express*, 21(15):18188–18195, 2013.
- [17] David W Hahn and Nicoló Omenetto. Laser-induced breakdown spectroscopy (libs), part i: review of basic diagnostics and plasma–particle interactions: still-challenging issues within the analytical plasma community. *Applied spectroscopy*, 64(12):335A–366A, 2010.
- [18] Zhongqi Hao, Lianbo Guo, Changmao Li, Meng Shen, Xiaoheng Zou, Xiangyou Li, Yongfeng Lu, and Xiaoyan Zeng. Sensitivity improvement in the detection of v and mn elements in steel using laser-induced breakdown spectroscopy with ring-magnet confinement. *Journal of Analytical Atomic Spectrometry*, 29(12):2309–2314, 2014.
- [19] Jiajia Hou, Lei Zhang, Wangbao Yin, Shunchun Yao, Yang Zhao, Weiguang Ma, Lei Dong, Liantuan Xiao, and Suotang Jia. Development and performance evaluation of self-absorption-free laser-induced breakdown spectroscopy for directly capturing

- optically thin spectral line and realizing accurate chemical composition measurements. *Optics express*, 25(19):23024–23034, 2017.
- [20] Heide Ibrahim, Benji Wales, Samuel Beaulieu, Bruno E Schmidt, Nicolas Thiré, Emmanuel P Fowe, Éric Bisson, Christoph T Hebeisen, Vincent Wanie, Mathieu Giguère, et al. Tabletop imaging of structural evolutions in chemical reactions demonstrated for the acetylene cation. *Nature communications*, 5:4422, 2014.
- [21] J Janszky, G Corradi, and RN Gyuzalian. On a possibility of analysing the temporal characteristics of short light pulses. *Optics Communications*, 23(3):293–298, 1977.
- [22] Karl Jousten. *Handbuch Vakuumtechnik*. Springer-Verlag, 2018.
- [23] Daniel J Kane and Rick Trebino. Characterization of arbitrary femtosecond pulses using frequency-resolved optical gating. *IEEE Journal of Quantum Electronics*, 29(2):571–579, 1993.
- [24] EP Kanter, PJ Cooney, DS Gemmell, K-O Groeneveld, WJ Pietsch, AJ Ratkowski, Z Vager, and BJ Zabransky. Role of excited electronic states in the interactions of fast (mev) molecular ions with solids and gases. *Physical Review A*, 20(3):834, 1979.
- [25] FX Kärtner, N Matuschek, T Schibli, U Keller, HA Haus, C Heine, R Morf, V Scheuer, M Tilsch, and T Tschudi. Design and fabrication of double-chirped mirrors. *Optics letters*, 22(11):831–833, 1997.
- [26] Mitchell Leslie. The man who stopped time. *Stanford Magazine*, Jun 2001.
- [27] Deepak Mathur. Multiply charged molecules. *Physics reports*, 225(4):193–272, 1993.
- [28] Tatsumi Mizogawa, Yohko Awaya, Yasuhito Isozumi, Rintaro Katano, Shin Ito, and Nobuhiro Maeda. New readout technique for two-dimensional position-sensitive detectors. *Nuclear Instruments and Methods in Physics Research Section A: Accelerators, Spectrometers, Detectors and Associated Equipment*, 312(3):547–552, 1992.
- [29] Tatsumi Mizogawa, Haruo Shiromaru, Michiyuki Sato, and Yoshiro Ito. A two-dimensional position-sensitive ion detector based on modified backgammon method with weighted-coupling capacitors. *International Journal of Mass Spectrometry*, 215(1-3):141–149, 2002.
- [30] Ch Nacke, W Bathe, F Kieseling, M Seemann, H Stolz, Ch Heyn, S Bargstädt-Franke, W Hansen, and D Heitmann. Phase sensitive resonant ultrafast reflection from gaas quantum wells. *physica status solidi (b)*, 206(1):307–314, 1998.

- [31] Reinhard Noll. Laser-induced breakdown spectroscopy. In *Laser-Induced Breakdown Spectroscopy*, pages 7–15. Springer, 2012.
- [32] Patrick OShea, Mark Kimmel, Xun Gu, and Rick Trebino. Increased-bandwidth in ultrashort-pulse measurement using an angle-dithered nonlinear-optical crystal. *Optics Express*, 7(10):342–349, 2000.
- [33] Patrick Oshea, Mark Kimmel, Xun Gu, and Rick Trebino. Highly simplified device for ultrashort-pulse measurement. *Optics letters*, 26(12):932–934, 2001.
- [34] Avishekh Pal, Robert D Waterbury, Edwin L Dottery, and Dennis K Killinger. Enhanced temperature and emission from a standoff 266 nm laser initiated libs plasma using a simultaneous 10.6 μm co 2 laser pulse. *Optics Express*, 17(11):8856–8870, 2009.
- [35] Jhon Pareja, Sebastian López, Daniel Jaramillo, David W Hahn, and Alejandro Molina. Laser ablation–laser induced breakdown spectroscopy for the measurement of total elemental concentration in soils. *Applied Optics*, 52(11):2470–2477, 2013.
- [36] Ali Ramadhan. Molecular movies and geometry reconstruction using coulomb explosion imaging. Master’s thesis, University of Waterloo, 2017.
- [37] Claude Rulliere et al. *Femtosecond laser pulses*. Springer, 2005.
- [38] K Sala, G Kenney-Wallace, and G Hall. Cw autocorrelation measurements of picosecond laser pulses. *IEEE Journal of Quantum Electronics*, 16(9):990–996, 1980.
- [39] François Salin, Patrick Georges, Gérard Roger, and Alain Brun. Single-shot measurement of a 52-fs pulse. *Applied optics*, 26(21):4528–4531, 1987.
- [40] ACF Santos, WS Melo, MM SantAnna, GM Sigaud, and EC Montenegro. Fragmentation and mean kinetic energy release of the nitrogen molecule. *Nuclear Instruments and Methods in Physics Research Section B: Beam Interactions with Materials and Atoms*, 261(1-2):200–203, 2007.
- [41] Jagdish P Singh and Surya Narayan Thakur. *Laser-induced breakdown spectroscopy*. Elsevier, 2007.
- [42] Spectra-Physics, 3635 Peterson Way, Santa Clara, CA 95054. *Spitfire Ace*, 2011.
- [43] Jacob Davis Babcock Stillman, Eadweard Muybridge, et al. horse in motion as shown by instantaneous photography, 1882.

- [44] Donna Strickland and Gerard Mourou. Compression of amplified chirped optical pulses. *Optics communications*, 55(6):447–449, 1985.
- [45] Robert Szipöcs, Kárpát Ferencz, Christian Spielmann, and Ferenc Krausz. Chirped multilayer coatings for broadband dispersion control in femtosecond lasers. *Optics letters*, 19(3):201–203, 1994.
- [46] Greg Taft, Andy Rundquist, Margaret M Murnane, Ivan P Christov, Henry C Kapteyn, Kenneth W DeLong, David N Fittinghoff, Marco A Krumbugel, John N Sweetser, and Rick Trebino. Measurement of 10-fs laser pulses. *IEEE journal of selected topics in quantum electronics*, 2(3):575–585, 1996.
- [47] Thermal velocity. <https://www.pfeiffer-vacuum.com/en/know-how/introduction-to-vacuum-technology/fundamentals/thermal-velocity/>.
- [48] L Torrisi, F Caridi, and L Giuffrida. Comparison of pd plasmas produced at 532 nm and 1064 nm by a nd: Yag laser ablation. *Nuclear Instruments and Methods in Physics Research Section B: Beam Interactions with Materials and Atoms*, 268(13):2285–2291, 2010.
- [49] Rick Trebino. *Frequency-resolved optical gating: the measurement of ultrashort laser pulses*. Springer US, 2000.
- [50] Z Vager, R Naaman, and EP Kanter. Coulomb explosion imaging of small molecules. *Science*, 244(4903):426–431, 1989.
- [51] Benjamin Wales. *Ultrafast Imaging of Molecular Processes in Small Molecules Using Coulomb Explosion Imaging*. PhD thesis, University of Waterloo, 2017.
- [52] Benji Wales, Éric Bisson, Reza Karimi, Samuel Beaulieu, Ali Ramadhan, Mathieu Giguère, ZiJian Long, Wing-Ki Liu, Jean-Claude Kieffer, François Légaré, et al. Coulomb imaging of the concerted and stepwise break up processes of ocs ions in intense femtosecond laser radiation. *Journal of Electron Spectroscopy and Related Phenomena*, 195:332–336, 2014.
- [53] Benji Wales, Eric Bisson, Reza Karimi, Jean-Claude Kieffer, Francois Légaré, and Joseph Sanderson. A coincidence detection algorithm for improving detection rates in coulomb explosion imaging. *Nuclear Instruments and Methods in Physics Research Section A: Accelerators, Spectrometers, Detectors and Associated Equipment*, 667:11–15, 2012.

- [54] Zhe Wang, Ting-Bi Yuan, Siu-Lung Lui, Zong-Yu Hou, Xiong-Wei Li, Zheng Li, and Wei-Dou Ni. Major elements analysis in bituminous coals under different ambient gases by laser-induced breakdown spectroscopy with pls modeling. *Frontiers of Physics*, 7(6):708–713, 2012.
- [55] WC Wiley and Ii H McLaren. Time-of-flight mass spectrometer with improved resolution. *Review of scientific instruments*, 26(12):1150–1157, 1955.
- [56] James D Winefordner, Igor B Gornushkin, Tiffany Correll, Emily Gibb, Benjamin W Smith, and Nicolás Omenetto. Comparing several atomic spectrometric methods to the super stars: special emphasis on laser induced breakdown spectrometry, libs, a future super star. *Journal of Analytical Atomic Spectrometry*, 19(9):1061–1083, 2004.
- [57] Rongxing Yi, Lianbo Guo, Changmao Li, Xinyan Yang, Jiaming Li, Xiangyou Li, Xiaoyan Zeng, and Yongfeng Lu. Investigation of the self-absorption effect using spatially resolved laser-induced breakdown spectroscopy. *Journal of Analytical Atomic Spectrometry*, 31(4):961–967, 2016.
- [58] Cai-Ping Zhang and Xiang-Yang Miao. Effects of the chirped pulse on dissociation and ionization processes for hydrogen molecular ions at low vibrational states. *Spectroscopy Letters*, 47(4):267–280, 2014.
- [59] Yang Zhao, Lei Zhang, Shu-Xia Zhao, Yu-Fang Li, Yao Gong, Lei Dong, Wei-Guang Ma, Wang-Bao Yin, Shun-Chun Yao, Ji-Dong Lu, et al. Review of methodological and experimental libs techniques for coal analysis and their application in power plants in china. *Frontiers of Physics*, 11(6):114211, 2016.

APPENDICES

Appendix A

Laser Induced Breakdown Spectroscopy (LIBS): An Industrial Application

A.1 Introduction

Laser-induced breakdown spectroscopy has grown significantly in popularity due to its speed of analysis, minimal sample preparation, and range of applicability (see bibliography for significant references). It is a spectroscopic technique that analyzes characteristic plasma plumes ejected from a material upon irradiation by intense pulsed laser light. This document describes the setup of a LIBS system through a collaboration between Sciencetech and University of Waterloo (University of Waterloo, Laser Matter Interaction group), the setup of the system is described, and then tested primarily, by analyzing plasma excitation-ionization spectra from complex alloys.

A.2 Laser System

The Empower laser (Figure [A.1.](#)) is a kHz Q switched laser 35 W 100 ns at 527 nm which is usually used to pump fs Ti:sapphire regenerative amplifier. The turning mirror directs the beam from the green laser to the sample chamber (Figure [A.5.](#)). It is normally used in the CPA (chirped pulse amplification) system. Nd:YLF lasers are multi-mode

and produce elongated rectangular beams with relatively high divergence. A cylindrical telescope system was introduced to produce a collimated beam of 5 mm diameter.

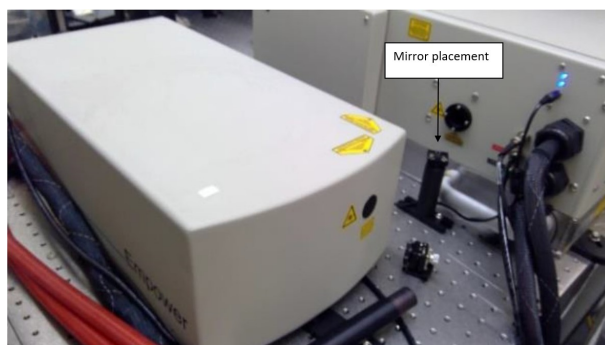


Figure A.1: Empower 30 Q-Switched Green Laser.

A.3 Apparatus

The apparatus (Figure A.2.) consists of a sample chamber which can be evacuated where the sample is mounted vertically on a rotating post, in order to provide a constantly fresh surface. The Empower achieves a laser fluence upward of 50 J/cm^2 and irradiances of approx. 0.5 GW/cm^2 .

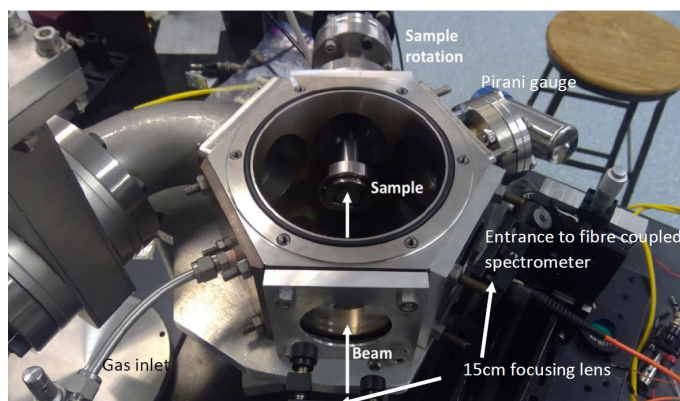


Figure A.2: Sample chamber.

A.4 Ablation Characteristics

Figure A.3. shows an image of a typical crater generated by 150 mm focal length lens (grid line spacing = 1 mm) typically around 0.2 mm diameter.

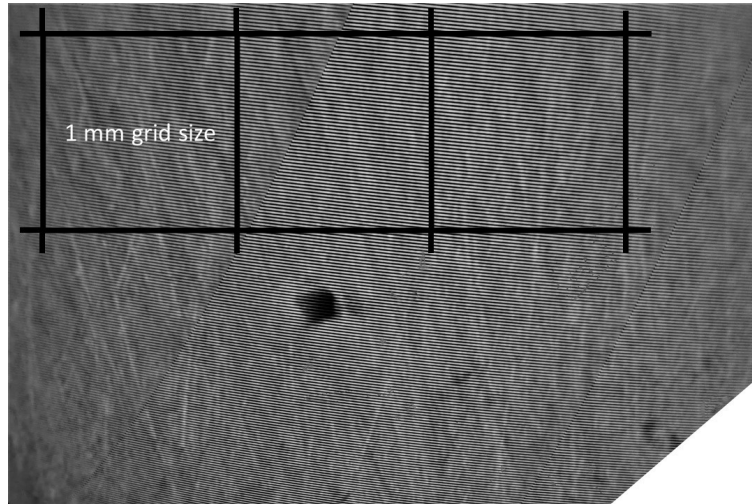


Figure A.3: Ablation spot.

A.5 Spectra Collection

The Empower delivers the beam to the chamber as shown in Figure A.5. where the LIBS signal is collected by an ultraviolet fibre optic cable with single objective (Figure A.4.) and sent to the Ocean Optics HR4000 spectrometer. The spectra range from 275 nm - 500 nm with a resolution of 3500 @ 400 nm (0.12 nm FWHM). Spectral intensities were corrected using convolution of grating efficiency and sensor quantum efficiency.

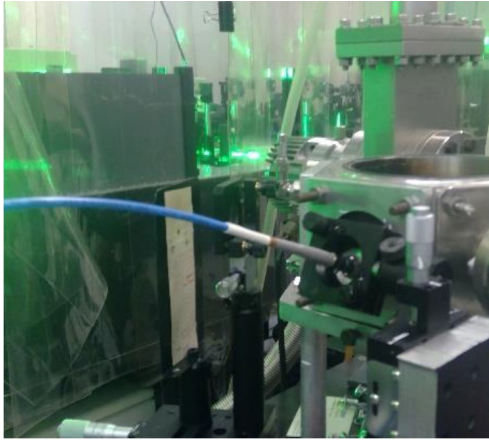


Figure A.4: Spectra collection setup

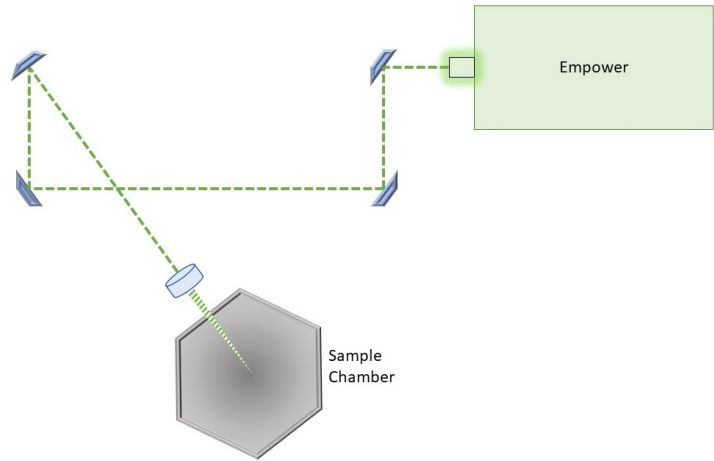


Figure A.5: Schematic

A.6 LIBS Test Results

A.6.1 Coating analysis: demonstration of LIBS for a prime handheld application

Figure A.6 shows the spectra of the super-alloys compared to the Fe reference in the full 275 nm to 500 nm spectral range of the HR4000 spectrometer. The spectra look to be complex and some seem to be indistinguishable to one another at a glance. This is not that case which will be demonstrated as we zoom in to identify key features.

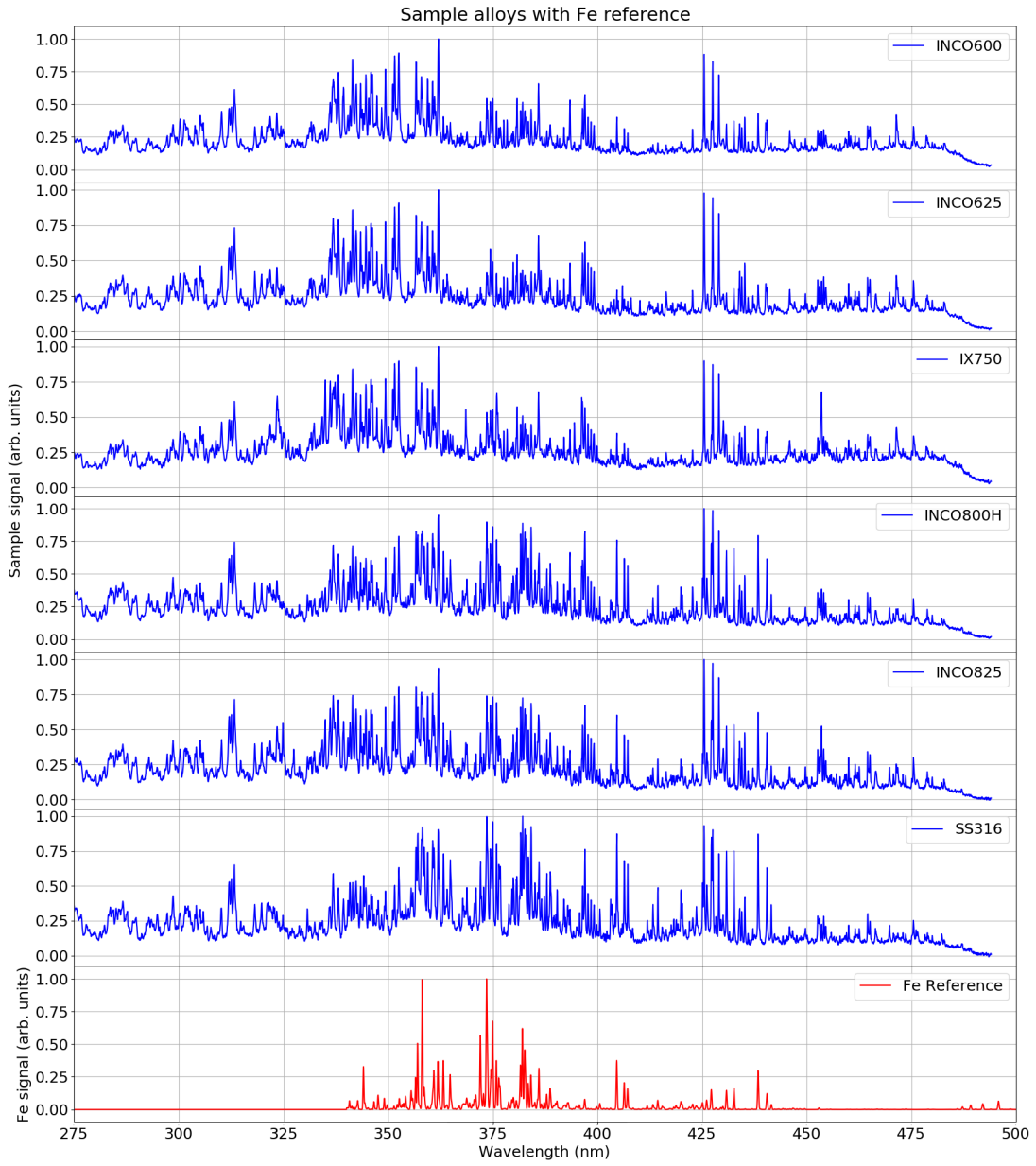


Figure A.6: Spectra of the super-alloys compared to the Fe reference in spectral range of the HR4000

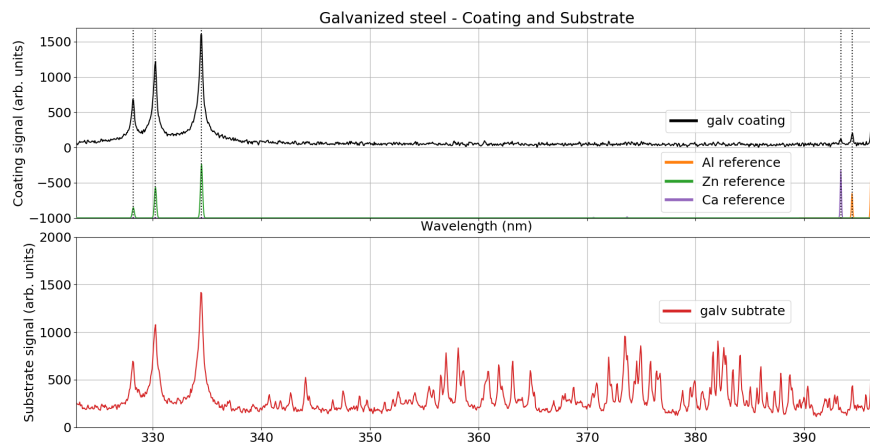


Figure A.7: The coating signal (top plot) is obtained by a rapid exposure to the laser, only ablating the surface coating of the galvanized steel. The coating signal is compared to reference spectra with accurate peak matching of Zn (328 nm, 330 nm, 334 nm), Ca (393 nm), and Al (394 nm and 396 nm). The substrate signal (bottom plot) is acquired by using a delayed exposure to ablate through the surface to the Fe reference.

Our first test is designed to show the power of LIBS to distinguish materials in close proximity varying by depth. One of a few methods for depth profiling and coating analysis has been demonstrated (Figure A.7.) for a sample of galvanized steel. Two exposures are needed for this method - a rapid ablation for the galvanized coating, and a delayed ablation for the substrate.

A.6.2 Mixed metals analysis: sorting common metal alloys and super-alloys with very complex spectra

For this test we have irradiated a series of alloys which have complex spectra and show that we can identify the samples by comparing their spectral features with each other and reference data.

Visible and longer wavelength excitation in the ns regime works well for relatively opaque samples like metals. Samples (Table A.1.) include: SSS316, INCONELs 600, 625, and X-750, INCOLOYs 800H and 825 (concentrations are within ranges). Figure A.9 shows INCONEL and INCOLOY spectra in comparison with iron (Fe) and molybdenum (Mo)

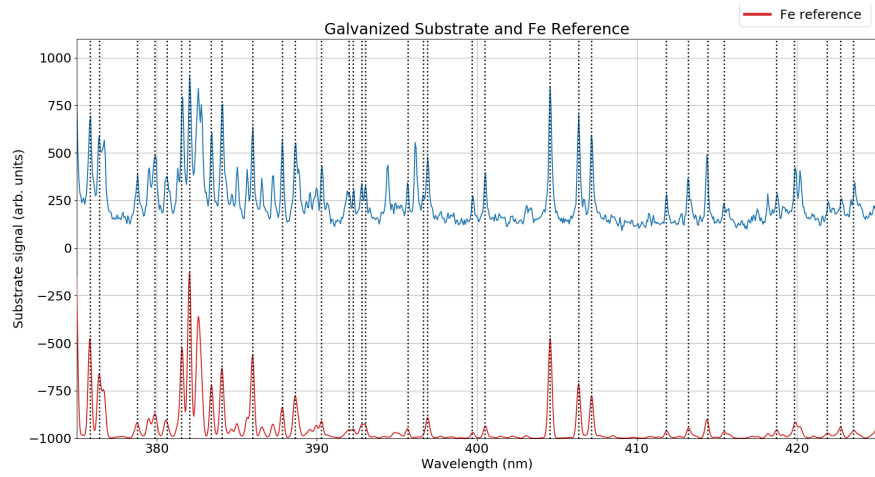


Figure A.8: Spectral segment from 375 to 425 nm to show wavelength accuracy and relative intensities for the Fe reference spectrum and the Empower LIBS spectrum.

reference spectra. Several Fe peaks clearly show INCOLOY 800H spectrum as having high Fe. INCONEL 625 has a high Mo content as identified by the peak at 386.411 nm.

The most sensitive Ni lines reside in the 340 nm - 355 nm region (see Section A.6.3.). INCONEL 600 spectrum is identified as the third member of this high Ni content alloy group.

Sample	Matrix	Unit	C	Al	Si	P	S	Ti	Cr	Mn	Fe	Co	Ni	Cu	Nb	Mo
SS316	Ni-Cr	%	0.1	0.4	0.5	0.015	0.015	0.4	21.5	0.5	5	1	58	3.6	9	
INCONEL 600	Ni-Cr	%	0.15		0.5		0.015		16	1	9.8		72	0.5		
INCONEL 625	Ni-Cr	%	0.1	0.4	0.5	0.015	0.015	0.4	21.6	0.5	5	1	58		3.5	9
INCONEL X-750	Ni-Cr	%	0.08	1	0.5		0.01	2.5	15.4	1	7	1	70	0.5	1	
INCOLOY 800H	Fe-Ni-Cr	%	0.1	0.6				0.6	23		43.2		32.5			
INCOLOY 825	Ni-Fe-Cr	%	0.05	0.2	0.5		0.03	1	23	1	22.7		46	2.5		3

Table A.1: Composition of samples.

A.6.3 Ni-Cr-Mo alloys: quantitative analysis and the selection of key elements for calibration

In general, most of these alloys (often called super-alloys) are comprised of a combination of these elements (with iron) and can be determined by examining the region from 350 400

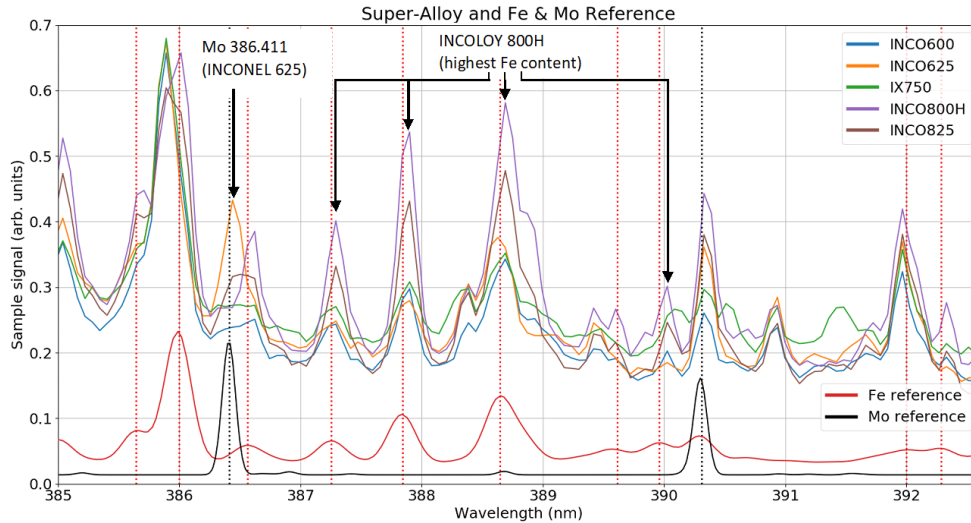


Figure A.9: INCONEL and INCOLOY spectra with Fe and Mo reference spectra for peak-matching.

nm (Figure A.10.). Figure A.11. shows SS316 spectra with minor interference from Fe and marked lines for Ni, Mo, and Cr. This analysis can be used for identification and rapid sorting of alloys. Calibrations based on these lines would yield quantitative information.

A.6.4 Diagnostics: an example of a measurement that is critical for quantitative LIBS

During early phases of the plasma, opacity is high, ions are not in thermodynamic equilibrium, and self-absorption is common. A delayed timing for spectrometer sync is required to avoid this so called self-absorption/self-reversal. Figure A.12. shows self-absorption of AL6160 alloy. The quickest identification of self-absorption is the discrepancy between the reference Al spectrum and the LIBS spectrum; the ratio of the two LIBS peaks should match the 1:2 ratio from the reference spectrum rather than the 1:1 ratio measured. See Figure A.13. for a literature example of self-absorption from [57].

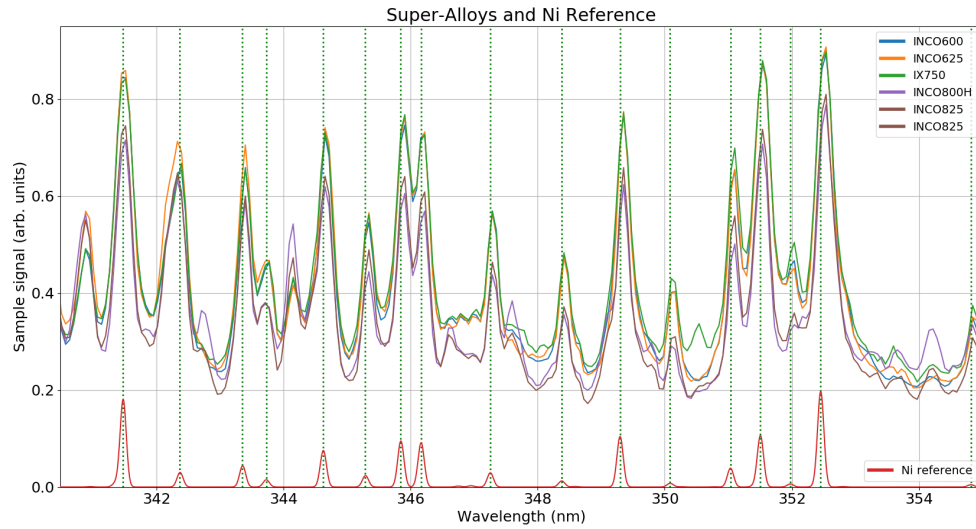


Figure A.10: INCONEL and INCOLOY narrow spectral segment 340 nm - 355 nm with Ni reference spectra for peak-matching.

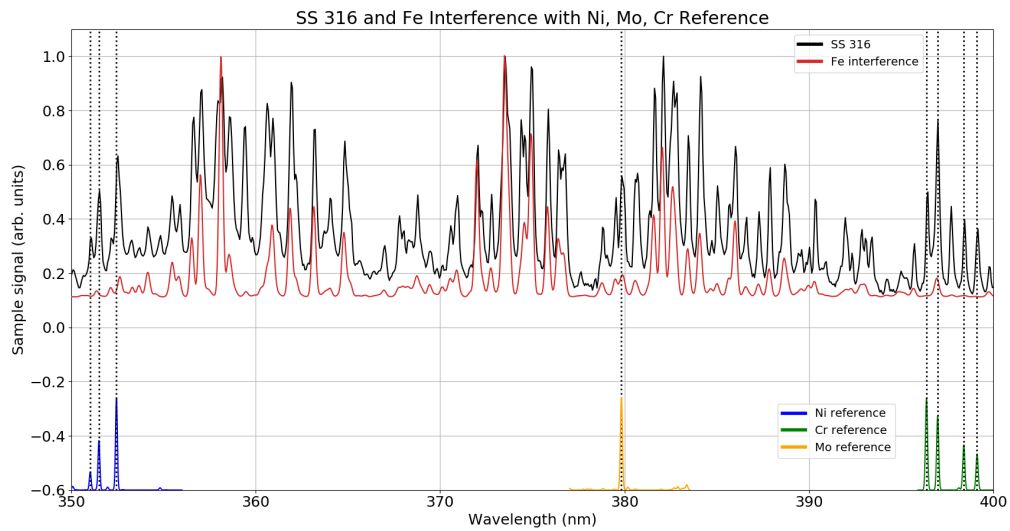


Figure A.11: SS316 with Fe interference and identification lines for Ni, Mo, and Cr.

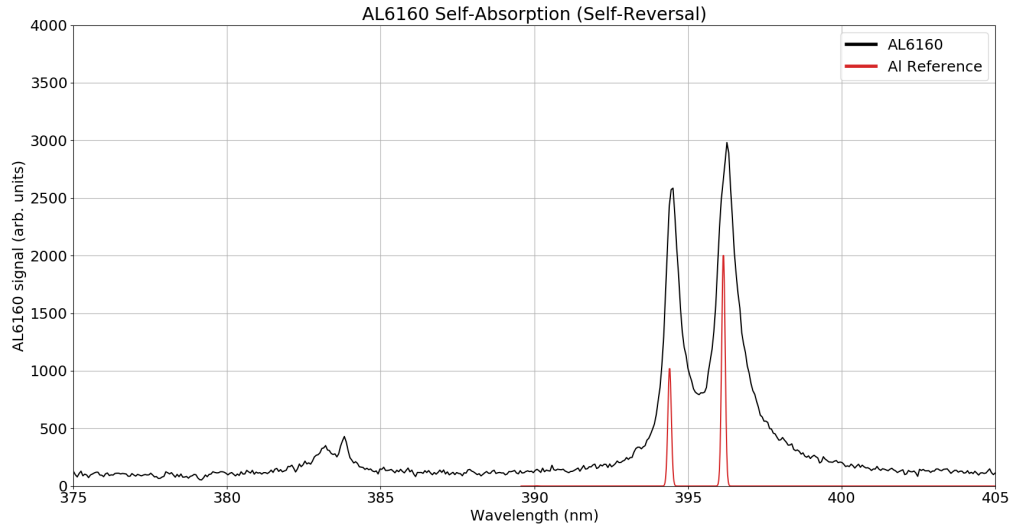


Figure A.12: The discrepancy between peak ratios of LIBS AL6160 spectrum and Al reference spectrum is good indication of self-absorption. The ratio of left peak to right peak in the reference spectrum is 1:2 as compared to the approx. 1:1 ratio in LIBS spectrum.

A.7 Conclusion and Future Work

We have constructed a LIBS system which is capable of generating plasma in opaque metallic targets and recording across the visible spectrum. We have tested the system on metal targets, and shown that we can perform surface and subsurface analysis, distinguish complex alloys by comparing data with reference spectra from the NIST database. Lastly, we have identified the presence of self absorption, a phenomenon which affects quantitative analysis and can be addressed in later setups.

The system which has potential for 100Hz - 1kHz repetition rate can be adapted for rapid scanning analysis which is a significant advantage over typical 10Hz systems. Further development of the spectrometer triggering setup can allow for time dependant plasma sampling in order to better assess parameters such as electron temperature accurately, for control of nanoscale processing. Finally, introduction of frequency doubling of the 527 nm laser light can allow us to probe transparent materials.

Literature Examples of Self-Absorption and Reversal

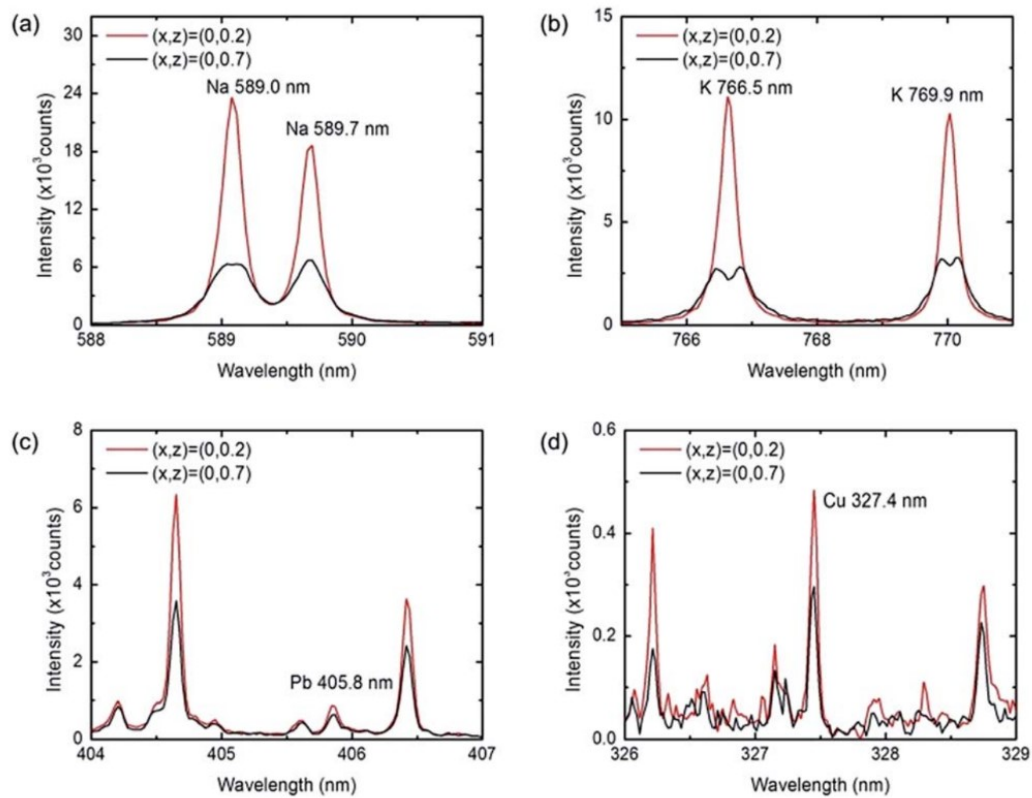


Figure A.13: Self-absorption example from [57].

Appendix B

Oscillator Optimization Technique

A simple optimization technique was followed to increase the output power of the oscillator. The full optimization methods can be found in the user manual for the oscillator. This technique involves adjustment of two different optics: a cavity mirror via an allen key knob, and the optical coupler. The power metre is placed directly behind the optical coupler. The oscillator should not be in modelock. The allen key should be turned until the power is maximized. Once at a maximum, the two knobs which control the horizontal and vertical tilt of the optical coupler must be adjusted to achieve maximum power. You can return to the allen key and slightly adjust to try and maximize power again. Then return to the optical coupler. The user should alternate between the two until a power of 650 mW to 700 mW is reached. The next step is to measure the modelock power output - optimal power is 400 mW. However, the modelock region needs to be *found* again. An easy way to do this is to turn the allen key in one direction until the power is approximately 350 mW. Modelock should be attempted in this region via the modelock button. If modelock cannot be found, the allen key should be turned in the other direction until the power is approximately 350 mW. Modelock should then be produced in this region. If modelock is not produced in one of the two directions, there is likely an issue which should be resolved by referring to the user manual or laser technician.

Appendix C

Spitfire Ace CPA System Techniques

C.1 Electronic Components

Fig. C.2 shows the electronic components for the Spitfire Ace. The laptop has the Spitfire Ace GUI control software which gives the user full control of the laser parameters, shown in Fig. C.1. The Spitfire Ace full manual [42] should be referred to for full details on operation.

C.1.1 Start-up from Standby Mode

For cold start procedure, refer to the Spitfire Ace manual. In Standby Mode, the Empower 45 power supply, the Timing and Delay Generator (TDG), and the Temperature Control Unit (TCU) will be turned on via their power switches, but the key-switch on the Empower 45 power supply and TDG will be off. To start from Standby Mode, follow the steps below.

1. Turn on the key-switch for Empower 45 power supply.
2. Turn on the key-switch for the TDG.
3. Ensure the “Current” setting on the Spitfire GUI software is set to 14 Amps.
4. Turn on the Empower 45 by pressing and holding the “Empower on/off” button on the Spitfire GUI software.

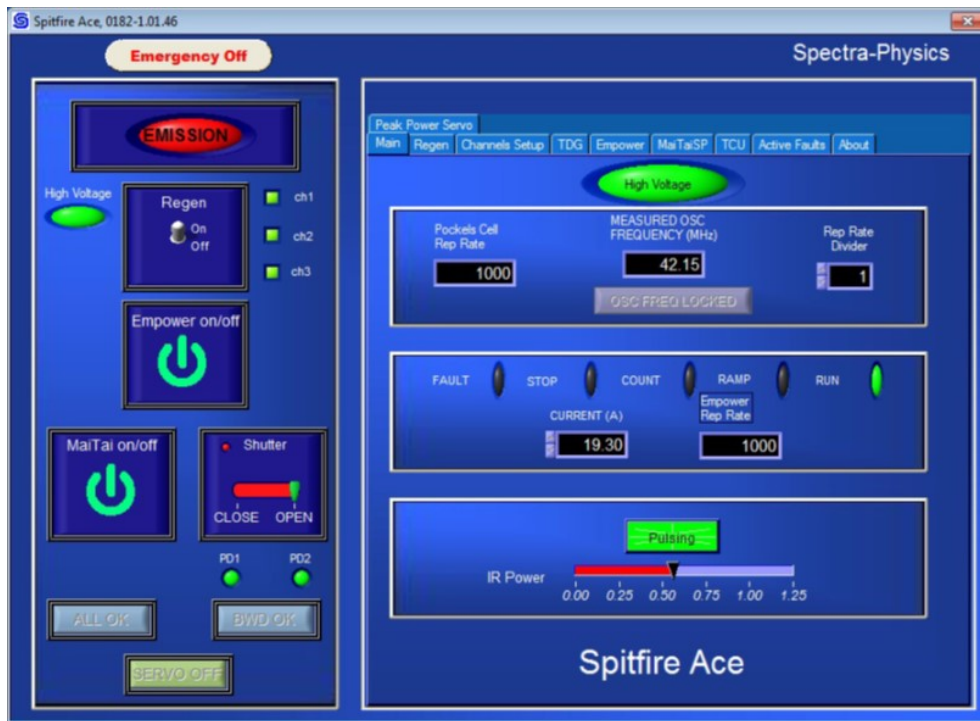


Figure C.1: The Spitfire Ace GUI control software. Reprinted from [42].

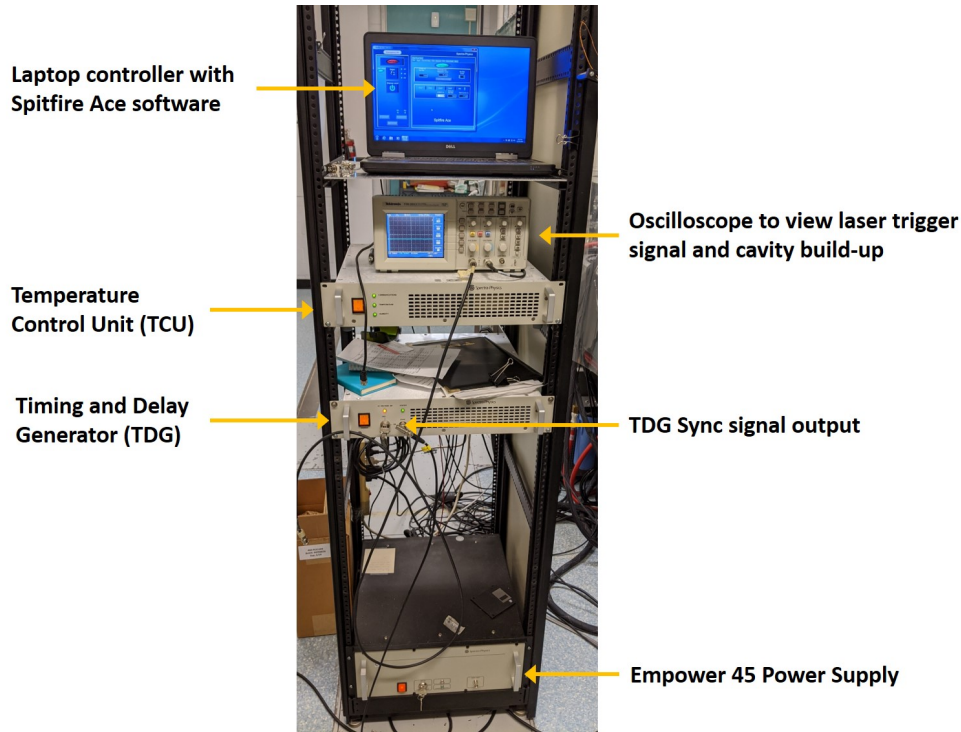


Figure C.2: Photo of the electronic components for the Spitfire Ace

5. Once the Empower is turned on, the Ti:Sapphire crystal begins to cool down. The temperature status can be seen on the TCU box. When the “Temperature” light is amber, the crystal is still cooling. When the light turns green, the crystal is cooled sufficiently. The temperature status can also be viewed on the “TCU” tab on the Spitfire software.
6. Once the crystal is cooled sufficiently, the regenerative amplifier can be turned on by clicking the “Regen” switch on the software.

C.1.2 Cable Connections

The cavity build-up can be viewed on the oscilloscope by connecting a coaxial cable from the Spitfire Ace coaxial output (where the chiller connections are located) to the oscilloscope. The build-up signal must be triggered from the “TDG Sync signal”. In order to trigger

from the TDG Sync signal, a coaxial cable must be connected from the TDG Sync output indicated in Fig. C.2 to the oscilloscope.

C.1.3 Optimization techniques

Over time, the performance of the Spitfire Ace slowly deteriorates. Optical alignment slowly falls off axis due to many reasons such as the constant vibrations that the optical bench experiences or changes in humidity and other environmental changes. The Spitfire will periodically require a ‘tune-up’ to regain peak performance. The Spitfire manual completely outlines the realignment procedures. Many times, a complete realignment is unnecessary; minor alignments can be done to improve performance.

There are two diagnostics that are used in the minor alignment techniques: power measurements and the build-up time signal. The main objective during optimization is to minimize the build-up time and then to maximize power. The build-up time can be viewed on an oscilloscope (connection instructions can be found in the manual). The build-up signal shows the amplification of the pulses as they travel back and forth through the crystal. The pulse signal starts off very small due to its low energy and then amplifies (*builds up*) after each successive pass through the crystal. An example of the build up signal can be seen in Fig. C.3. The timing of the pockel cells should release the pulse from the cavity at its highest amplification or conversely put, you don’t want to keep the pulse in the cavity after its highest peak. The build up signal should have minimum amplified spontaneous emission (ASE) as well. The amount of ASE can be seen by taking a ratio of the peak of the pulse signal average to the average amount of *rise* of the valley. The idea of build-up time reduction is to minimize the number of passes the pulse takes through the cavity for it to reach its highest peak. Once the build-up time has been minimized, the power of the pulses should be maximized by observing the power metre as you adjust the beam steering mirrors. There is logged performance information for reference and comparison.

There are two beams that need to be aligned in the crystal: the pump beam and the seed beam (beam from the oscillator). The most common reason for decreasing laser performance is misalignment of the seed beam in the Spitfire. The oscillator seems to be much more sensitive to weather changes than the Spitfire. It also doesn’t help that the oscillator beam travels a long distance before it ultimately reaches the Ti-Sapph crystal. These two reasons make the seed beam much more susceptible to misalignment than the pump beam. When aligning either the pump beam or seed beam, you always need access to two beam steering mirrors (in fact, two beam steering mirrors are almost always required

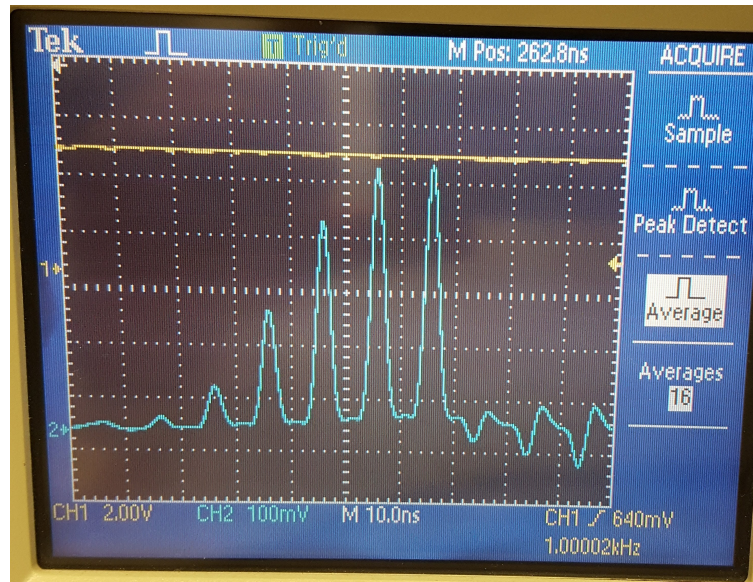


Figure C.3: Build-up signal showing the amplification of pulses after each pass through the Ti:Sapphire crystal.

for any alignment task). The two diagnostics explained above must be used for alignment of both beams.

The first attempt should be to align the seed. Two seed beam steering mirrors can be easily accessed from just outside of the Spitfire. If that fails, the interior of the Spitfire must be accessed. You can choose a pair of seed mirrors in the Spitfire to adjust. If that fails, you must adjust a pair of pump mirrors. When adjusting any pair of mirrors, you must use the two diagnostics explained above. Sometimes you might find it easy to alternate between all three pairs of mirrors. The results from this technique can be found in [C.2](#).

C.2 Optimization Results

C.2.1 December 12, 2017

Current - 15.1 A

Ch3 - 377 ns

Power before compressor = 3.45 W

Current = 18.4 A

Ch3 - 250 ns

Power before compressor = 6.1 W

After compressor = 4.5 W

Current = 18.4 A

Ch3 - 260 ns

Power before compressor = 6.41-6.44W

After compressor = 4.7 W

C.2.2 January 11, 2018

Current = 15.1 A

Ch3 = 389.75 ns (highest peak)

Power after comp = 2.56 W

Current = 18.4 A

Ch3 = 250 ns

Power after comp = 4.630 - 4.655

Current = 18.4 A

Ch3 = 260 ns (highest peak)

Power after comp = 4.818 - 4.828 W

C.2.3 March 29, 2018

Current 15.1

Ch3 405 ns – There are several peaks that are almost exactly same height

First peak is at 375 ns

Power after comp 2.72 W

Current 18.4
Ch3 260 ns (highest peak, although very close in height to 250 ns peak)
Power after comp 4.8 W

Current 18.4
Ch3 250 ns
Power after comp 4.54 W

C.2.4 June 21, 2018

Current 15.1
Ch3 375.5 ns (365.5 and 375.5 ns both are have pretty much equal peaks)
Power after comp 2.6 W

At 18.4 A, CH3 250 ns and 260 ns have exactly same height, both are highest peaks

Current 18.4
Ch3 250 ns
Power after comp 4.5 W

Current 18.4
Ch3 260 ns
Power after comp 4.7 W

Appendix D

Hollowfibre Alignment Technique

Aligning the beam is a straightforward but sometimes timely process. Two irises can be setup 1 metre apart. The first one is placed at the focus of the pulses (approximately 1 metre from the focusing lens) and the second iris 1 metre away. A beam line can be then be set if the laser is aligned through both irises. After the beam is set, the placement of the irises can be marked. The idea is then to move the hollowfibre chamber in place such that the silica hollow core fibre follows the beam line set by the irises. The laser can be run at low power during the alignment process to avoid damage to the fibre. If placed correctly, the beam should be coupled to the fibre and transmitted through. The transmitted power can be measured and the transmission percentage calculated. The translation stages can be adjusted in tandem to improve the transmission percentage. The best transmission percent achieved was approximately 55%.

Appendix E

GRENOUILLE Techniques

Fortunately, the GRENOUILLE device used (model 8-9-122-THICK-USB) comes with a complete user guide and documentation for its QuickFrog software, all found in the QuickFrog Windows Start Menu folder (entitled “Femtisoft Technologies”) after it has been installed. The Quick Start Guide outlines a stepwise process for alignment of the GRENOUILLE that should be followed precisely. If starting from scratch, the hard copy manual includes device cable setup and installation instructions. The “Documentation” files were found to be extremely helpful. There are two different modes in QuickFrog: Time Mode and Space Mode. Space Mode provides beam profiling which is only useful for alignment, as described in the Quick Start guide and further described in the documentation page entitled “Space Mode” or in the installation folder entitled “spacemode.html”. Time Mode is where the temporal characteristics of the pulses are measured. Various windows are found in Time Mode. Time Mode and its various windows are described in the Documentation page entitled “Time Mode” or “timemode.html”.

Time Mode

A screenshot of the QuickFrog software in Time Mode is shown in Fig. E.1. There are 5 main windows in Time Mode which are used to obtain a FROG trace. The “measured FROG trace” is the experimentally measured FROG trace which should be as symmetrical as possible to abide by the laws of physics for SHG FROG. The “Retrieved FROG trace” is obtained by the FROG algorithm which iteratively guesses pulses that correspond to the experimentally measured trace. As stated in Ch. 4.3.2 retrieved FROG trace is generally a more accurate measurement of the pulse, so the retrieved FROG trace was focused on more

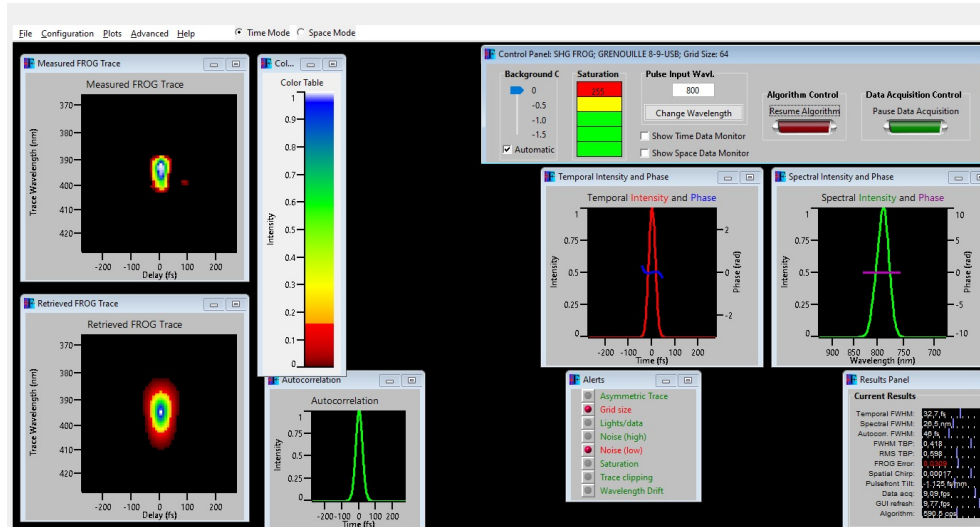


Figure E.1: Screenshot of QuickFrog software in Time Mode during operation.

than the measured. There are “Temporal Intensity and Phase” and “Spectral Intensity and Phase” windows. These are the plotted temporal intensity and spectral intensity functions, both with phase functions, found in the equation for the pulse, $E(t)$, which was guessed by the algorithm for the retrieved FROG trace. With $E(t)$, both the temporal and spectral intensity can be found using Eqns. 4.5 - 4.8. The “Results” window shows quantitative data about the pulse and FROG measurements.

Dithering Crystal - AGC Driver

The AGC driver controls the angle dithering of the SHG crystal in the GRENOUILLE device. Shown in Fig. E.2, there are two tuning knobs on the AGC driver: the phase knob and amplitude knob. The phase knob controls the dithering speed of the crystal. The amplitude knob controls the amplitude of the dithering angle. The amplitude of the dithering angle must be set to cover the entire spectral bandwidth of the pulse and the dithering speed should be set such that its rotation frequency matches the repetition rate of the laser.



Figure E.2: Photo of the AGC driver and its phase and amplitude tuning knobs.

Data Output

In the Time Mode Documentation page, there is also a section outlining the various menu commands in QuickFrog. There is a “File -> Save Data” command which outputs all of the retrieved data from Time Mode into separate data files. The data file formats are shown in “fileformats.html”.

Data Analysis

Shown below is the code for retrieving and plotting the frequency marginal, autocorrelation, spectral data in frequency, and temporal data in time.

```
#=====
#Returns the frequency marginal and autocorrelation from a FROG .dat file
#The FROG .dat file is exported from the QuickFrog software
#=====
def get_frequency_marginal_and_autocorrelation():

    print("Choose FROG trace file for frequency marginal")

    Tk().withdraw() # we don't want a full GUI, so keep the root window from
        appearing
    FROG_exp_fname = askopenfilename() # show an "Open" dialog box and return
        the path to the selected file

    # FROG_exp_data = np.genfromtxt(FROG_exp_file, delimiter=" ", skip_header=2)

    with open(FROG_exp_fname) as f:
        header1 = f.readline() #get grid size of FROG data. i.e., 32 32
        header2 = f.readline() #get 2nd header: fs/pixel, nm/pixel, central
            wavelength

    print("FROG grid size is ", header1)

    print("The header of FROG file below is: ")
    print(header2, " (fs/pixel, nm/pixel, central wavelength)") #prints
        header file of FROG trace data file
```

```

        #fs/pixel, nm/pixel, central wavelength

FROG_grid = header1.split()      #grid information is in form 32 32 (or
    64 64 or # #)

                                #need to split it into array [32,32] to
                                access integer

num_points = int(FROG_grid[0])   #number of points in one slice of the
    grid

                                #i.e., a 64x64 grid has 64 points in a
                                single slice

mid_col = int(int(FROG_grid[0])/2) #middle column in a row of the grid
    #i.e., for 64x64 grid, mid_col=31

#get FROG 2D grid data into 2D array
FROG_data = np.genfromtxt(FROG_exp_fname, delimiter=" ", skip_header=2)

autocorrelation_spectrum = []
for col in FROG_data:           #go through each row in FROG grid
    autocorrelation_spectrum.append(np.sum(col)) #get the sum of each row
        in the grid
                                #to be put in a 1D array

FROG_data_T = np.transpose(FROG_data)

wavelength_marginal_signal = [] #spectral intensity list for y-axis of
    plot
for row in FROG_data_T:        #go through each row in FROG grid
    wavelength_marginal_signal.append(np.sum(row)) #get the sum of each row
        in the grid
                                #to be put in a 1D array

wavelength_marginal_signal /= np.nanmax(wavelength_marginal_signal)
    #normalize spectral intensity to 1

grid_info = header2.split()     #split 2nd header into array:
                                #[fs/pixel, nm/pixel,
                                central wavelength]

```

```

fs_pixel = math.fabs( float(grid_info[0]) )    #get fs/pixel. For plotting
autocorrelation spectrum
nm_pixel = math.fabs( float(grid_info[1]) )    #get nm/pixel. For plotting
frequency spectrum
central_wvl = math.fabs( float(grid_info[2]) ) #get central wavelength
start_wvl = central_wvl - nm_pixel * mid_col  #get the start wavelength
start_delay = 0 - fs_pixel * mid_col

wvl = []                                     #initialize wavelength list for
x-axis
for i in range(0, num_points):               #populate wavelength list
    wvl.append( start_wvl + i*nm_pixel )
wvl = np.array(wvl)
delay = []                                    #for autocorrelation
for i in range(0, num_points):               #populate wavelength list
    delay.append( start_delay + i*fs_pixel )
delay=np.array(delay)

[freq, frequency_marginal_signal] = do_jacobian_transformation(wvl,
    wavelength_marginal_signal)

frequency_marginal_signal /= np.nanmax(frequency_marginal_signal)

return [wvl, wavelength_marginal_signal, freq, frequency_marginal_signal,
    delay, autocorrelation_spectrum, FROG_exp_fname]

#=====
#Plots the frequency marginal which is retrieved from the get function
#=====
def plot_frequency_marginal():

    [wvl, wavelength_marginal_signal, freq, frequency_marginal_signal, \
    delay, autocorrelation_spectrum, FROG_exp_fname] =
        get_frequency_marginal_and_autocorrelation()

#Wavelength marginal

```



```

fig, ax = plt.subplots()
line1 = ax.plot(wvl, wavelength_marginal_signal, "red")
ax.grid(True, which = 'major')
ax.minorticks_on()
ax.grid(True, which = 'minor', alpha=0.2)
plt.title('Wavelength Marginal ' + "..." +
          FROG_exp_fname[len(FROG_exp_fname)-50:len(FROG_exp_fname)])
ax.set_xlabel('Wavelength (nm)')
ax.set_ylabel('signal')

```

```

#Frequency marginal
fig, ax = plt.subplots()
line1 = ax.plot(freq/1000, frequency_marginal_signal, "red")
ax.grid(True, which = 'major')
ax.minorticks_on()
ax.grid(True, which = 'minor', alpha=0.2)
plt.title('Frequency Marginal ' + "..." +
          FROG_exp_fname[len(FROG_exp_fname)-50:len(FROG_exp_fname)])
ax.set_xlabel('Frequency (THz)')
ax.set_ylabel('signal')

```

```

return

```

```

#=====
#Plots the autocorrelation which is retrieved from the get function
#=====

```

```

def plot_autocorrelation():

    [wvl, spectral_intensity, delay, autocorrelation_spectrum, FROG_exp_fname]
    = get_frequency_marginal_and_autocorrelation()

    fig, ax = plt.subplots()
    line1 = ax.plot(delay, autocorrelation_spectrum, "red")
    ax.grid(True, which = 'major')
    ax.minorticks_on()
    ax.grid(True, which = 'minor', alpha=0.2)
    plt.title('Autocorrelation ' + "..." +

```

```

        FROG_exp_fname[len(FROG_exp_fname)-50:len(FROG_exp_fname)])
ax.set_xlabel('delay (fs)')
ax.set_ylabel('signal')

return

#=====
#Gets the spectral data from the ESpectral .dat file
#The ESpectral .dat file is exported from the QuickFrog software
#=====
def get_ESpectral():

    print("Choose an ESpectral.dat file in the format [Wavelength (nm),
          Intensity,\
          Phase (in radians), Real Part of Field, Imaginary Part of Field] for
          spectral information")

    Tk().withdraw() # we don't want a full GUI, so keep the root window from
                    # appearing
    ESpectral_file = askopenfilename() # show an "Open" dialog box and return
    the path to the selected file

    ESpectral_data = np.transpose( np.genfromtxt(ESpectral_file) )

    wavelength = ESpectral_data[0]
    spectral_intensity = ESpectral_data[1]
    phase = ESpectral_data[2]
    EField_real = ESpectral_data[3]
    EField_imaginary = ESpectral_data[4]

    return [ wavelength, spectral_intensity, phase, EField_real,
            EField_imaginary, ESpectral_file ]

#=====

```

```

#Plots the spectral data from the get function
#=====
def plot_ESpectral():

    [wavelength, spectral_intensity, phase, EField_real, EField_imaginary,
     ESpectral_file] = get_ESpectral()

    #plot spectrum
    fig, ax = plt.subplots()
    line1 = ax.plot(wavelength, spectral_intensity, "red")
    ax.grid(True, which = 'major')
    ax.minorticks_on()
    ax.grid(True, which = 'minor', alpha=0.2)
    plt.title('Spectral Intensity and Phase ' + "..." + \
              ESpectral_file[len(ESpectral_file)-50:len(ESpectral_file)])
    ax.set_xlabel('wavelength (nm) and phase')
    ax.set_ylabel('signal')

    ax_phase = ax.twinx() # instantiate a second axes that shares the same
                          # x-axis
    line2 = ax_phase.plot(wavelength, phase, "blue")
    ax_phase.set_ylabel('phase (radians)')

    #plot EField real
    fig, ax = plt.subplots()
    line1 = ax.plot(wavelength, EField_real, "red")
    ax.grid(True, which = 'major')
    ax.minorticks_on()
    ax.grid(True, which = 'minor', alpha=0.2)
    plt.title('EField Real ' + "..." + \
              ESpectral_file[len(ESpectral_file)-50:len(ESpectral_file)])
    ax.set_xlabel('wavelength (nm)')
    ax.set_ylabel('signal')

    #plot EField imaginary
    fig, ax = plt.subplots()
    line1 = ax.plot(wavelength, EField_imaginary, "red")
    ax.grid(True, which = 'major')

```

```

ax.minorticks_on()
ax.grid(True, which = 'minor', alpha=0.2)
plt.title('EField Imaginary ' + "..." + \
          ESpectral_file[len(ESpectral_file)-50:len(ESpectral_file)])
ax.set_xlabel('wavelength (nm)')
ax.set_ylabel('signal')

return

#=====
#Gets the temporal data from the ETemporal .dat file
#The ETemporal .dat file is exported from the QuickFrog software
#=====
def get_ETemporal():

    print("Choose an ETemporal.dat file in the format [Time (fs), Intensity,\
          Phase (in radians), Real Part of Field, Imaginary Part of Field] for
          spectral information")

    Tk().withdraw() # we don't want a full GUI, so keep the root window from
                    # appearing
    ESpectral_file = askopenfilename() # show an "Open" dialog box and return
    the path to the selected file

    ESpectral_data = np.transpose( np.genfromtxt(ESpectral_file) )

    time = ESpectral_data[0]
    temporal_intensity = ESpectral_data[1]
    phase = ESpectral_data[2]
    EField_real = ESpectral_data[3]
    EField_imaginary = ESpectral_data[4]

    return [ time, temporal_intensity, phase, EField_real, EField_imaginary,
            ESpectral_file ]

#=====
#Plots the temporal data from the get function

```

```

#-----
def plot_ETemporal():

    [time, temporal_intensity, phase, EField_real, EField_imaginary,
     ESpectral_file] = get_ETemporal()

    #plot spectrum
    fig, ax = plt.subplots()
    line1 = ax.plot(time, temporal_intensity, "red")
    ax.grid(True, which = 'major')
    ax.minorticks_on()
    ax.grid(True, which = 'minor', alpha=0.2)
    plt.title('Temporal Intensity and Phase ' + "..." + \
              ESpectral_file[len(ESpectral_file)-50:len(ESpectral_file)])
    ax.set_xlabel('time (fs) and phase')
    ax.set_ylabel('signal')

    ax_phase = ax.twinx() # instantiate a second axes that shares the same
        x-axis
    line2 = ax_phase.plot(time, phase, "blue")
    ax_phase.set_ylabel('phase (radians)')

    #plot EField real
    fig, ax = plt.subplots()
    line1 = ax.plot(time, EField_real, "red")
    ax.grid(True, which = 'major')
    ax.minorticks_on()
    ax.grid(True, which = 'minor', alpha=0.2)
    plt.title('EField Real ' + "..." + \
              ESpectral_file[len(ESpectral_file)-50:len(ESpectral_file)])
    ax.set_xlabel('time (fs)')
    ax.set_ylabel('signal')

    #plot EField imaginary
    fig, ax = plt.subplots()
    line1 = ax.plot(time, EField_imaginary, "red")
    ax.grid(True, which = 'major')
    ax.minorticks_on()

```

```

ax.grid(True, which = 'minor', alpha=0.2)
plt.title('EField Imaginary ' + "... " + \
          ESpectral_file[len(ESpectral_file)-50:len(ESpectral_file)])
ax.set_xlabel('time (fs)')
ax.set_ylabel('signal')

return

def plot_autoconvolution_and_marginal():

    [freq, signal_f_autoconvolve, wvl, signal_w_autoconvolve] =
        get_autoconvolution()

    [wvl_grenouille, wavelength_marginal_signal, freq_grenouille,
     frequency_marginal_signal, delay, \
     autocorrelation_spectrum, FROG_exp_fname] =
        get_frequency_marginal_and_autocorrelation()

    freq_shift = freq[ find_index( signal_f_autoconvolve,
                                   np.nanmax(signal_f_autoconvolve)) ]
    wvl_shift = wvl[ find_index( signal_w_autoconvolve,
                                 np.nanmax(signal_w_autoconvolve)) ]
    freq_grenouille_shift = freq_grenouille[ find_index(
        frequency_marginal_signal, \
                                                np.nanmax(frequency_marginal_signal))
                                             ]
    wvl_grenouille_shift = wvl_grenouille[ find_index(
        wavelength_marginal_signal, \
                                                np.nanmax(wavelength_marginal_signal))
                                             ]

    #   freq_shift = -1* freq_grenouille_shift
    #   wvl_shift = 0
    #   freq_grenouille_shift = 0
    #   wvl_grenouille_shift = 0

    #plot autoconvolution and frequency marginal vs frequency
    #=====

```

```

fig, ax = plt.subplots()
line1 = ax.plot( (freq - freq_shift)/1000,
    signal_f_autoconvolve/np.nanmax(signal_f_autoconvolve), "red")
ax.grid(True, which = 'major')
ax.minorticks_on()
ax.grid(True, which = 'minor', alpha=0.2)
# plt.title("Autoconvolution vs frequency ")
# ax.set_xlabel('Frequency (THz)')
# ax.set_ylabel('Signal')

#Frequency marginal
line2 = ax.plot( (freq_grenouille-freq_grenouille_shift)/1000,
    frequency_marginal_signal, "blue")
ax.grid(True, which = 'major')
ax.minorticks_on()
ax.grid(True, which = 'minor', alpha=0.2)
plt.title('Autoconvolution and Frequency Marginal ' + "... " \
    + FROG_exp_fname[len(FROG_exp_fname)-50:len(FROG_exp_fname)])
ax.set_xlabel('Frequency (THz)')
ax.set_ylabel('signal')

#plot autoconvolution and wavelength marginal vs wavelength
#=====
fig, ax = plt.subplots()
line3 = ax.plot(wvl-wvl_shift,
    signal_w_autoconvolve/np.nanmax(signal_w_autoconvolve), "red")
ax.grid(True, which = 'major')
ax.minorticks_on()
ax.grid(True, which = 'minor', alpha=0.2)
# plt.title("Autoconvolution vs Wavelength ")
# ax.set_xlabel('Wavelength (nm)')
# ax.set_ylabel('Signal')

line4 = ax.plot(wvl_grenouille-wvl_grenouille_shift,
    wavelength_marginal_signal, "blue")
ax.grid(True, which = 'major')
ax.minorticks_on()
ax.grid(True, which = 'minor', alpha=0.2)

```

```
plt.title('Autoconvolution and Wavelength Marginal ' + "... " + \
          FROG_exp_fname[len(FROG_exp_fname)-50:len(FROG_exp_fname)])
ax.set_xlabel('Wavelength (nm)')
ax.set_ylabel('signal')

return
```

Appendix F

Time-Of-Flight Spectrometer Techniques

F.1 Coulomb Explosion Imaging Chamber Alignment Technique

The diagram of the laser beamline into the CEI chamber is shown in Fig. F.1. The first step in aligning the laser into the CEI chamber is to set the final beam-steering mirror (FBSM) in the correct general position. The height of the TOF focusing mirror can be roughly measured through the chamber window. The screw holes on the optical table can be used to horizontally align the FBSM with the TOF focusing mirror. The angle of the FBSM can be set in the direction of the TOF mirror.

After the FBSM is set by eye, the laser can be turned on. The laser should be directed to the initial beam-steering mirror then reflected to the FBSM. Both beam-steering mirrors must be adjusted until the laser is incident onto the TOF mirror. It will be clear that the laser is hitting the TOF mirror by the presence of a diverging back reflection. The laser will initially be focused by the TOF mirror inside the TOF spectrometer then *de-focused*. Hence the diverging back reflection outside of the chamber. Once the laser is confirmed to be hitting the TOF mirror, the alignment needs to be fine-tuned so that the incident beam is centred on the TOF mirror. The idea is to analyze the incident laser beam with respect to the back reflection from TOF mirror. When perfectly aligned, the incident beam should be centred exactly on the outgoing back reflection as shown in Fig. F.2. It is easier to scan the first iris in both the vertical and horizontal directions while keeping an eye on

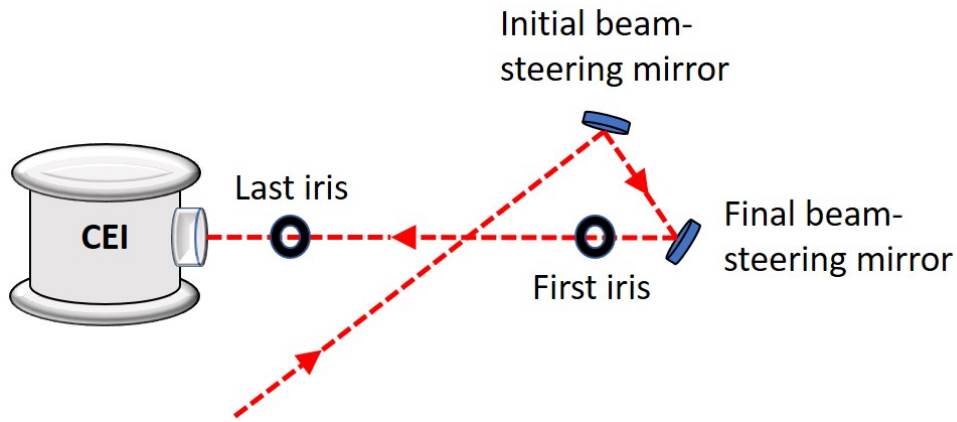


Figure F.1: Laser beamline into CEI chamber

the back reflection. A card can be used to block the incident beam to see how it compares to the vertical half, the horizontal half, and a quarter of the back reflection, shown in Fig. F.3. Once the iris is positioned such that the incident beam is perfectly centred on the back reflection, a second iris can be set (shown in Fig. F.1) to create a beamline between both irises. The beam steering mirrors should be adjusted such that the beam follows, exactly, the beamline set by both irises (i.e., the beam should be centred on both irises). If perfectly aligned, the first iris can aperture the incident beam to a point, which will go through the centre of the second iris then hit the centre of the focusing mirror and finally the back reflection will go back through the centre of both irises.

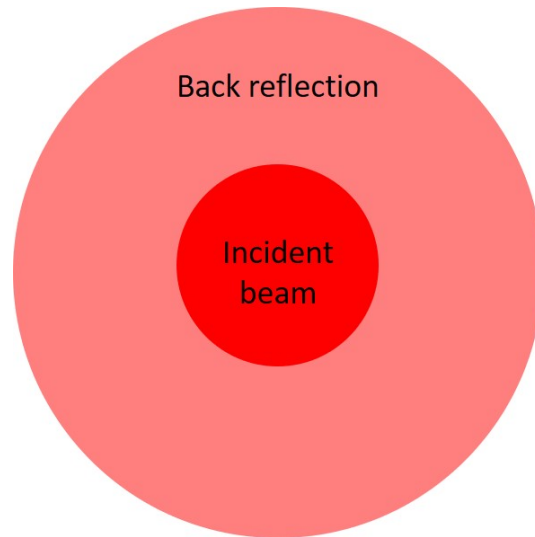


Figure F.2: Visualization of a perfectly aligned CEI beamline, where the incident beam is centred exactly on the outgoing back reflection.

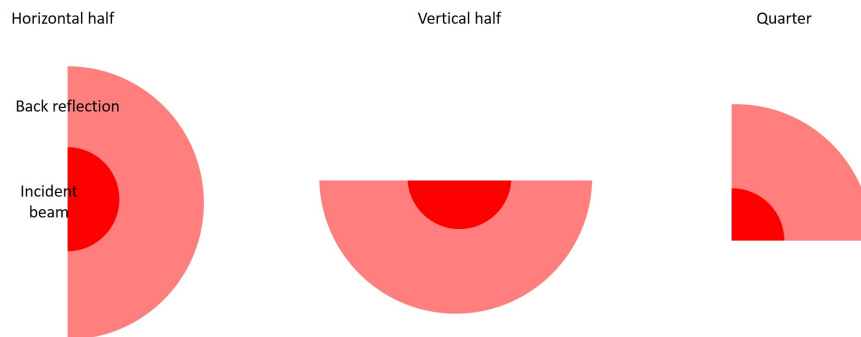


Figure F.3: A card can be used to block the incident beam to see how it compares to the vertical half, the horizontal half, and a quarter of the back reflection.

F.2 Electronic Connections

In order to operate the TOF spectrometer, the ion detector box, the four position detection boxes, and the TDG Sync signal output (shown in Appendix C Fig. 2), must be connected.

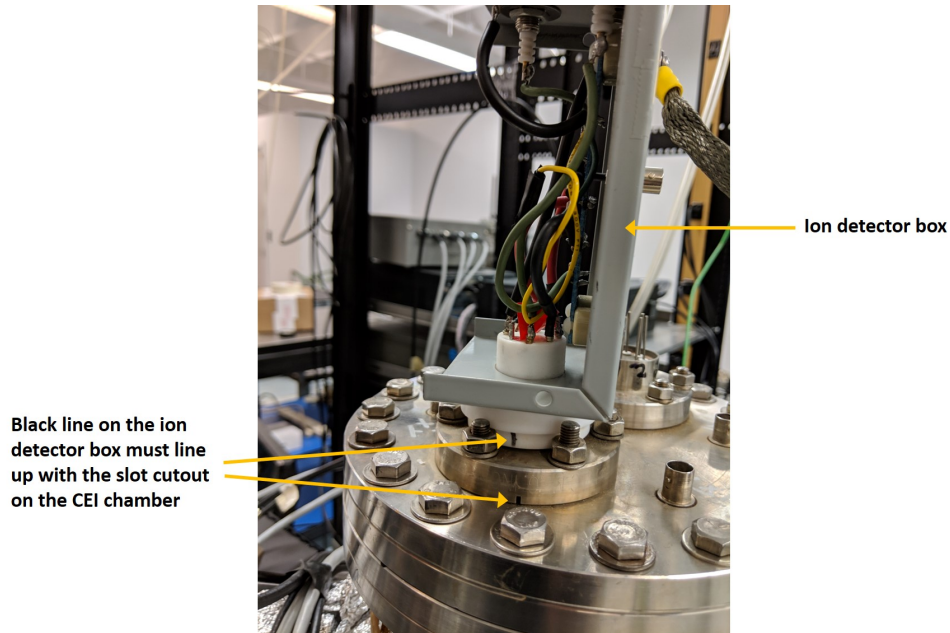


Figure F.4: The proper connection orientation for the ion detector box. Notice there is a small black line on the white part of the ion detector box which must align with the slot cutout shown on the CEI chamber.

The ion detector box has 8 pins in a circular pin-out array which must be connected to the CEI chamber as shown in Fig. F.4. There are two 8-pin input connections on the CEI chamber, one for the ion detector and one for the electron detector. This appendix does not consider the electron detector. Ensure the ion detector box is connected to the correct 8-pin input by viewing Fig. F.5 for perspective on orientation.

The 4 position boxes must be connected to the 4 coaxial inputs on the CEI chamber such that the labels on each box match the labels on the CEI chamber (i.e., “1XY”, “1 \bar{X} Y”, “1X \bar{Y} ”, “1 \bar{X} \bar{Y} ”).

The ion detection box has two connections that must be connected to two different voltage supplies: the voltage for the ion extraction region and the voltage for the ion MCP. The 4 position detection boxes should be connected to the DAQ. The TDG Sync signal must be connected to the DAQ as well, for triggering.

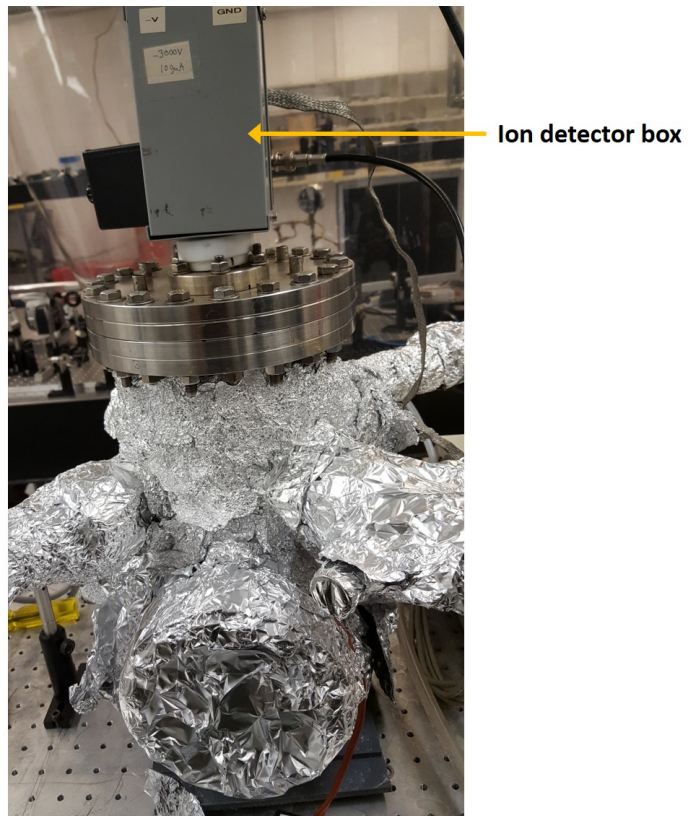


Figure F.5: Perspective on orientation of the CEI chamber to assist in the proper connection of the ion detector box.

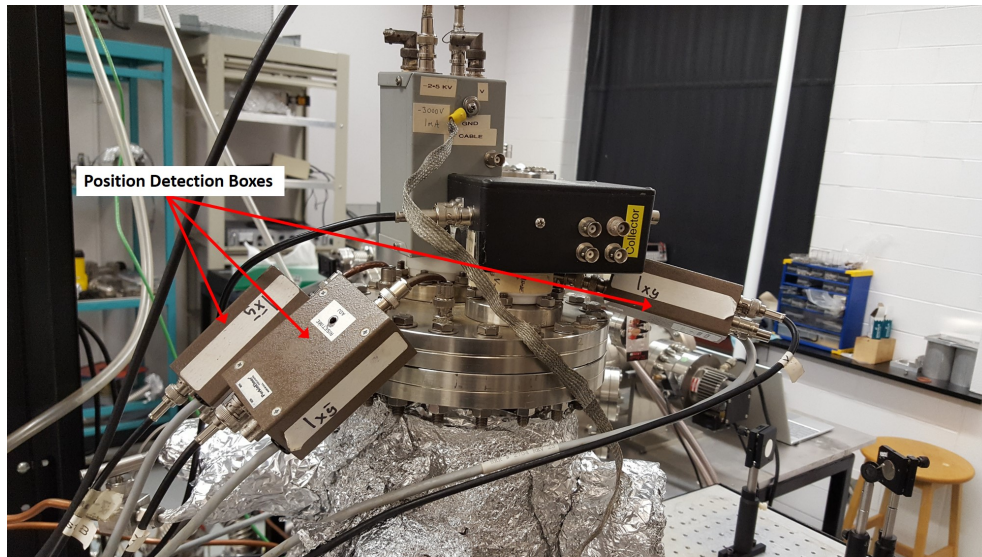


Figure F.6: There are 4 position detection boxes that need to be connected to 4 coaxial inputs on the CEI chamber. Only 3 position detection boxes are shown, the 4th box is not visible.

F.2.1 Starting the TOF Spectrometer

Once the electronics are connected properly as described in Section F.2, the two voltage supplies need to be ramped up together. Before ramping up the voltage supplies, the CEI chamber pressure gauge should be turned off and the voltage fuse box needs to be turned on. The ion extraction region was usually ran at 3000 kV and the ion MCP was ran at 2300 kV. Both voltage supplies should be incremented in unison by 10 Volts at a time until 2300 kV. Once both supplies are at 2300 kV, the ion extraction voltage supply can be incremented up to 3000 kV.

On the DAQ computer, the user must open the folder on the desktop entitled “UW2016”, then open the executable file “CEIROOTDAQ.exe”. From that application, CEI experimental data can be recorded.

F.3 Plot Identification Algorithm Code

=====

Created on Jul 26, 2018
@author: Michael Singh
=====

```
import matplotlib.pyplot as plt
from tkinter import Tk
from tkinter.filedialog import askopenfilename
import seaborn as sns
import numpy as np
from _overlapped import NULL
from fileinput import filename
```

```
#constants
```

```
Amu_kg = 1.6605389e-27; #1 amu = 1.6605389e-27 kg
```

```
e = 1.60217662e-19; #C
```

```
# d = 76.825e-3; #m
```

```
d = 89.3e-3; #m
```

```
E = 2.8e3; #V
```

```
Ar_+t = '$Ar^{1+}$'
```

```
Ar_2+t = '$Ar^{2+}$'
```

```
Ar_3+t = '$Ar^{3+}$'
```

```
H_+t = '$H^{+}$'
```

```
H_2+t = '$H_2^{+}$'
```

```
H_3+t = '$H_3^{+}$'
```

```
CO2+t = '$CO_2^{+}$'
```

```
N+t = '$N^{+}$'
```

```
N_2_+t = '$N_2^{+}$'
```

```
N_2_2+t = '$N_2^{2+}$'
```

```
H2O_+t = '$H_2O^{+}$'
```

```
O2_+t = '$O_2^{+}$'
```

```
def populate_elements():
```

```
    #elements.txt contains each element of the periodic table along with info
    about it
```

```

filename = "ion_list.txt"

elm= {}      #dictionary of elements and standard atomic masses, i.e., el[
    "hydrogen" ] = 1.008

# open file for reading
with open(filename, "r") as f:

    for line in f:
        line = line.split('\t')

        #creates dictionary of elements names:mass, symbol:mass, atomic#:mass
        elm[ line[0] ] = float(line[3]) #element name:mass
        elm[ line[1] ] = float(line[3]) #symbol:mass
        elm[ line[1].lower() ] = float(line[3]) #lowercase symbol:mass
        elm[ line[2] ] = float(line[3]) #atomic#:mass

    return elm

#element = mass
Ac = 227
Al = 26.981538
Am = 243
Sb = 121.76
Ar = 39.948
As = 74.9216
At = 210
Ba = 137.327
Bk = 247
Be = 9.012182
Bi = 208.98038
Bh = 264
B = 10.811
Br = 79.904
Cd = 112.411
Cs = 132.90545
Ca = 40.078
Cf = 251
C = 12.0107

```


Ce = 140.116
Cl = 35.4527
Cr = 51.9961
Co = 58.9332
Cu = 63.546
Cm = 247
Db = 262
Dy = 162.5
Es = 252
Er = 167.26
Eu = 151.964
Fm = 257
F = 18.9984032
Fr = 223
Gd = 157.25
Ga = 69.723
Ge = 72.61
Au = 196.96655
Hf = 178.49
Hs = 269
He = 4.002602
Ho = 164.93032
H = 1.00794
In = 114.818
I = 126.90447
Ir = 192.217
Fe = 55.845
Kr = 83.8
La = 138.9055
Lr = 262
Pb = 207.2
Li = 6.941
Lu = 174.967
Mg = 24.305
Mn = 54.938049
Mt = 268
Md = 258
Hg = 200.59
Mo = 95.94
Nd = 144.24

Ne = 20.1797
Np = 237
Ni = 58.6934
Nb = 92.90638
N = 14.00674
No = 259
Os = 190.23
O = 15.9994
Pd = 106.42
P = 30.973762
Pt = 195.078
Pu = 244
Po = 210
K = 39.0983
Pr = 140.90765
Pm = 145
Pa = 231.03588
Ra = 226
Rn = 222
Re = 186.207
Rh = 102.9055
Rb = 85.4678
Ru = 101.07
Rf = 261
Sm = 150.36
Sc = 44.95591
Sg = 266
Se = 78.96
Si = 28.0855
Ag = 107.8682
Na = 22.98977
Sr = 87.62
S = 32.066
Ta = 180.9479
Tc = 98
Te = 127.6
Tb = 158.92534
Tl = 204.3833
Th = 232.0381
Tm = 168.93421

```
Sn = 118.71
Ti = 47.867
W = 183.84
Uub = 277
Ds = 269
Rg = 272
U = 238.0289
V = 50.9415
Xe = 131.29
Yb = 173.04
Y = 88.90585
Zn = 65.39
Zr = 91.224
```

```
#Common molecules
```

```
N2 = N*2
O2 = O*2
CO2=C+2*O
H2O=H*2+O
Acetone=C*3+H*6+O
OCS=O+C+S
```

```
def TOF_plot(filename):
```

```
# Tk().withdraw() # we don't want a full GUI, so keep the root window from
# appearing
```

```
# filename = askopenfilename() # show an "Open" dialog box and return the
# path to the selected file
```

```
t = [] # list for times of flight
loop_index = 0
```

```
if filename != '':
```

```
    # open file for reading
    with open(filename, "r") as f:
```

```
        # character position multiplier
```

```

line_num = 3

f.seek(121*line_num + 36,0) # seek to 3rd line, position 39
    #where the number of laser shots is located
num_laser_shots = float(f.read(9)) # read in number of laser shots

while True:
    f.seek(121*line_num + 84,0) # seek to 3rd line, position 84
    temp_t = f.read(9) # read in time
    line_num += 1

    if not temp_t: break #if time is null or 0, skip
    try: #try to convert temp_t to float, if it is not a number,
        skip line
        temp_t = float(temp_t) #convert to float so mathematical
            operations can be applied

        t.append( temp_t ) #add flight time to list

    except ValueError: #skip line if temp_t is not a number
        continue

t = np.array(t)
# t = 4*t
title_index = 50
if title_index > len(filename): title_index = len(filename)
plt.figure(loop_index)
plt.title("..." + filename[len(filename)-50:len(filename)])
plt.xlabel('time (ns)')
plt.ylabel('signal')
plt.hist(t, int(num_laser_shots/100), histtype='step', fill = False,
    density=True, stacked=True)

loop_index += 1

return t, filename, line_num

```

```

from TOF_Peaks import TOF_plot
import matplotlib.pyplot as plt
from math import sqrt
from ion_dictionary import *
from CONSTANTS import *
import random

#Returns time of flight calculation based on mass to charge ratio
#Uses equation of the line
def t_func(mq_):
    time = slope*sqrt(mq_) + b
    return time

def find_mass_to_charge(time):

    mass_charge = ((time - b)/slope)**2

    return mass_charge

#Plots point of ion
#(mass to charge ratio, time of flight, text to annotate point, theoretical
    boolean)
#Example for N23+
#(N2/3, it's time of flight, 'N2{3+}')
#(Mass of N2/charge of ion, its measured time of flight, text to annotate the
    plotted point, *optional
# argument (boolean) -- "True" will plot a theoretical point)
#Theoretical point is simply to check where an ion will fall on the plotted line
def plot_ion(mq, time, text, *theoretical):

    if theoretical:    #plot theoretical point
        plt.plot(sqrt(mq), t_func(mq), 'r*');
        plt.text(sqrt(mq), t_func(mq) - 70, text, color = 'r')
    else:             #plot real point
        plt.plot(sqrt(mq), time, 'b*');
        plt.text(sqrt(mq), time - 70, text)
    return

#plots ion point on the TOF spectra plot
#generates vertical line on plot to help identify peaks

```

```

def plot_peak_identify(mq, text):

    #height of point
    height = random.randint(880,940)

    #plot ion point
    plt.plot( t_func(mq), height, 'g*');
    plt.text( t_func(mq), height - 20, text, color = 'g')

    #generate dashed vertical line
    x = []
    y = []
    i = 0
    while i < int(height):
        x.append(t_func(mq))
        y.append(i)
        i+=30

    plt.plot( x, y, 'g', linestyle = ":")

    return

elm = populate_elements() #create dictionary of ion_dictionary to return atomic
    masses

TOF_1 = 142;          #CO2 jan24 2019 400mw vertical
# TOF_1 = 202;          #TOF of H+ (H2^1+ = TOF_H2_1) CO2 aug13 2018 400mw
    vertical
mass_charge_1 = sqrt(H/1);    #sqrt(mass of H+ / charge of H+)
TOF_2 = 477;          #CO2 jan24 2019 400mw vertical
# TOF_2 = 1031;          #TOF of 2nd known ion CO2 aug13 2018 400mw vertical
mass_charge_2 = sqrt(CO2/1);

#t = slope * sqrt(m/q) + b --- b is y-intercept
b = ( TOF_1*mass_charge_2 - TOF_2*mass_charge_1 ) / ( mass_charge_2 -
    mass_charge_1 );
slope = (TOF_1 - b) / ( mass_charge_1 );

#since Acetone is usually has the longest TOF

```

```

#I use it to set a limit on the x-axis (sqrt(m/q))
t=[]
x=[]
i=0
while i<sqrt(Acetone+10):
    t.append(slope*i+b)    #t = slope * sqrt(m/q) + b --- b is y-intercept
    x.append(i)
    i+=0.01

# Plot the TOF equation fit line
# plt.figure(1)
# plt.title("TOF VS SQRT(m/q)")
# plt.xlabel('SQRT(m/q)')
# plt.ylabel('TOF (ns)')
# plt.minorticks_on()
# plt.grid( which='major', axis='both')
#
# plt.plot(x,t, color = 'grey')

#H+
# plot_ion(H, 140, '$H^{+}$')
# #text can be set as
#
# #H2+
# plot_ion(H*2, 162, '$H_2^{+}$')
#
# #N2+
# # plot_ion(N*2, 840, '$N_2^{+}$')
#
# #Ar2+
# plot_ion(Ar/2, 338, '$Ar^{2+}$')

# #Theoretical
# =====
# plt.plot(sqrt(Acetone), t_func(Acetone/1), 'r*');
# plt.text(sqrt(Acetone), t_func(Acetone/1) - 70, 'Acetone', color = 'r')
# plot_ion(Acetone, t_func(Acetone/1), 'Acetone', True)

```

```

# plot_ion(N2, t_func(N2), '$N_2^{+}$', True)
# plot_ion(N, t_func(N), '$N^{+}$', True)
# plot_ion(H2O, t_func(H2O), '$H_2O^{+}$', True)
# plot_ion(CO2, t_func(CO2), '$CO_2^{+}$', True)
# plot_ion(H*3, t_func(H*3), '$H3^{+}$', True)

peak_identify = True
if peak_identify:

#     "C:/Users/Michael/Google Drive/Graduate School/CEI Data/Dec 3 2018 All
#     Vertical/Ar_Dec3_2018_50mW.log"
#     fname = r"C:\Users\Michael\Google Drive\Graduate School\CEI Data\Dec 3
#     2018 All Vertical\Ar_Dec3_2018_50mW.log"

#     TOF_plot(r"C:\Users\Michael\Google Drive\Graduate School\CEI Data\Aug 13
#     - CO2\CO2_400mW_Vertical_50000shots.log")
#     TOF_plot(r"C:\Users\Michael\Google Drive\Graduate School\CEI Data\Aug 13 -
#     CO2\CO2_400mW_Vertical_10000shots.log")

#     TOF_plot(r"C:\Users\Michael\Google Drive\Graduate School\CEI
#     Data\Jan24_2019_OCSandCO2\CO2_400mw_Ver_100000shots_Jan24.log")
#     TOF_plot(r"C:\Users\Michael\Google Drive\Graduate School\CEI Data\Dec 3
#     2018 All Vertical\BG_Dec3_2018_400mW.log")

identify_peaks = False

if identify_peaks == True:

    plot_peak_identify(N2, '$N_2^{+}$')
    plot_peak_identify(N, '$N^{+}$')
    plot_peak_identify(N/3, '$N^{3+}$')
    plot_peak_identify(H, '$H^{+}$')
    plot_peak_identify(H*2, '$H_2^{+}$')
    plot_peak_identify(H2O, '$H_2O^{+}$')
#     plot_peak_identify(Ar, '$Ar^{+}$')
#     plot_peak_identify(Ar/2, '$Ar^{2+}$')
    plot_peak_identify(CO2, '$CO_2^{+}$')
    plot_peak_identify(O2, '$O_2^{+}$')
    plot_peak_identify(O, '$O^{+}$')
    plot_peak_identify(C, '$C^{+}$')

```



```

plot_peak_identify(C+O, '$CO^{+}$')

# selection = input("To find mass-to-charge ratio - type 'M' \nTo find time of
  flight - type 'T' \n('0' to exit): ")
# while selection != '0':
#     if selection == "T":
#         mass_charge = float(input("Enter a mass-to-charge ratio to see its
  time of flight: "))
#         print( t_func(mass_charge) )
#     if selection == "M":
#         time = float(input("Enter a time of flight to see its mass-to-charge
  ratio: "))
#         print( find_mass_to_charge(time) )
#     selection = input("To find mass-to-charge ratio - type 'M' \nTo find time
  of flight - type 'T' \n('0' to exit): ")

# print( t_func(H2O) )
# print( find_mass_to_charge(444) )
plt.show()

```
